A COMPARATIVE STUDY OF KALMAN FILTER IMPLEMENTATIONS FOR RELATIVE GPS NAVIGATION

A Thesis

by

MATTHEW PEYTON FRITZ

Submitted to the Office of Graduate Studies of
Texas A&M University
in partial fulfillment of the requirements for the degree of

MASTER OF SCIENCE

December 2009

Major Subject: Aerospace Engineering

A COMPARATIVE STUDY OF KALMAN FILTER IMPLEMENTATIONS FOR RELATIVE GPS NAVIGATION

A Thesis

by

MATTHEW PEYTON FRITZ

Submitted to the Office of Graduate Studies of
Texas A&M University
in partial fulfillment of the requirements for the degree of

MASTER OF SCIENCE

Approved by:

Chair of Committee,	Srinivas Rao Vadali
Committee Members,	Tamás Kalmár-Nagy
	Aniruddha Datta
	Renato Zanetti
Head of Department,	Dimitris Lagoudas

December 2009

Major Subject: Aerospace Engineering

ABSTRACT

A Comparative Study of Kalman Filter
Implementations for Relative GPS Navigation. (December 2009)
Matthew Peyton Fritz, B.S, Texas A&M University
Chair of Advisory Committee: Dr. Srinivas Rao Vadali

Relative global positioning system (GPS) navigation is currently used for autonomous rendezvous and docking of two spacecraft as well as formation flying applications. GPS receivers deliver measurements to flight software that use this information to determine estimates of the current states of the spacecraft. The success of autonomous proximity operations in the presence of an uncertain environment and noisy measurements depends primarily on the navigation accuracy. This thesis presents the implementation and calibration of a spaceborne GPS receiver model, a visibility analysis for multiple GPS antenna cone angles, the implementation of four different extended Kalman filter architectures and a comparison of the advantages and disadvantages of each filter used for relative GPS navigation. A spaceborne GPS model is developed to generate simulated GPS measurements for a spacecraft located on any orbit around the Earth below the GPS constellation. Position and velocity estimation algorithms for GPS receivers are developed and implemented. A visibility analysis is performed to determine the number of visible satellites throughout the duration of the rendezvous. Multiple constant fields of view are analyzed and results compared to develop an understanding of how the GPS constellation evolves during the proximity operations. The comparison is used to choose a field of view with adequate satellite coverage. The advantages and disadvantages of the relative navigation architectures are evaluated based on a trade study involving several parameters.

It is determined in this thesis that a reduced pseudorange filter provides the best

overall performance in both relative and absolute navigation with less computational cost than the slightly more accurate pseudorange filter. A relative pseudorange architecture experiences complications due to multipath rich environments and performs well in only relative navigation. A position velocity architecture performs well in absolute state estimation but the worst of the four filters studied in relative state estimation.

DEDICATION

In dedication to my loving wife Amylyn, whose unending support and incredible patience was key in the completion of this thesis.

ACKNOWLEDGMENTS

I would like to thank everyone that has played a major role over the course of my education. First and foremost, I would like to thank God for the grace and good fortune he has shown on me all the days of my life. I would like to thank my true love, Amylyn, for always supporting me. I would like to thank my mother who continuously supported me and instilled the importance of hard work and determination. I would like to thank Keith and Holly. The support they gave me during my entire college career is unequaled by any other person and inspired belief in myself. I would like to thank my friends that I have bounced ideas off of and struggled through problems with. Thank you all for all that you have done, known and unknown.

Academically, I would like to thank first and foremost my advisor, Dr. Vadali, for his countless words of advice and mentoring. Without his guidance specifically over the past two years, the thesis work presented here would never have been possible. I'd like to thank Dr. Haisler and Karen Knabe for making being a graduate student much easier due to their hard work and easy approachability.

Professionally, I would like to thank Naz Bedrossian for his perseverance and hard work which made it possible for me to be a Draper Laboratory Fellow. I'd like to thank Renato Zanetti for his patience, guidance, and support which were key to the completion of this thesis. I would like to thank Ian Mitchell and Piero Miotto for allowing me to work on the project they oversee.

Finally, on a more personal note, I'd like to thank the one man who has had the greatest impact on my entire life, Paster Charles Treptow. He showed me the way to my savior Jesus Christ. Nothing in my life could have been accomplished without the incredible foundation of faith that he has instilled in me.

TABLE OF CONTENTS

CHAPTER Page

LIST OF TABLES

TABLE Page

LIST OF FIGURES

FIGURE Page

FIGURE Page

FIGURE Page

CHAPTER I

INTRODUCTION

A. Precursors of GPS Navigation

For many centuries, explorers have faced the need to be able to determine their current location on the surface of the Earth. For directional navigation, the magnetic compass has been used for many centuries. The invention of the compass allowed for navigators to no longer have to rely solely on the stars for directional navigation. The magnetic compass was first developed by the Chinese around 200 BC. Mariners took advantage of Earth's magnetic field and began to commonly use the magnetic compass for navigation around 900 AD [1]. While the compass gave the navigators knowledge of the general direction they were traveling, it did not give them their current location on the Earth's surface. One of the earliest navigation tools that allowed for a general knowledge of the current position was the astrolabe. The astrolabe determined latitude by determining the altitude of the sun and stars. Another commonly used navigation tool for latitude determination was the sextant. The sextant was capable of providing more accurate latitude measurements by determining the altitude between the horizon and celestial bodies [2].

Although latitude was easily determined using celestial navigation, an accurate measurement of longitude could not be made using celestial navigation. A clockmaker by the name of John Harrison developed a device that became known as the chronometer in the mid 1700s.

The journal model is *IEEE Transactions on Automatic Control.*

The chronometer kept an accurate measure of the current time of home port at any point on the surface of the globe. Using the home port time and current local time on the vessel, a longitude determination within 30 nautical miles was achieved [3].

Celestial navigation and chronometers were used for navigation until the early 20th century. Gyroscopic compasses replaced magnetic compasses in the early 20th century. Gyroscopic compasses are not influenced by Earth's magnetic field and always point to true north. In 1935, radar was introduced allowing for vessels as well as aircraft to locate other vessels, land or any obstruction during instances of decreased visibility [4]. Radar technology uses radio waves to determine location. A radar set transmits radio waves and determines an accurate location of an object based on the time it takes the echo to return and the Doppler shift in that echo. It also has the capability to measure the speed of an object based on the Doppler shift. Long range navigation, developed shortly after radar, uses pulsed radio transmissions from two stations to determine the location of a vessel or aircraft. A disadvantage to long range navigation is its limited coverage.

B. Global Position System

In the 1950s, the space race that ensued between the United States and former Soviet Union paved the way for present day navigation. The Navy Navigation Satellite System (NNSS), also known as TRANSIT, was the first operational satellite system launched in 1972. The NNSS allowed for position determination based on satellites orbiting at an altitude of 600 nautical miles. Doppler shift was measured in a frequency constantly transmitted from the satellites. Aircraft applications of the system proved not useful since corrections had to be made based on vehicle velocity. In addition, the number of satellites were limited to five worldwide, resulting in signal blackouts

that would last as long as 100 minutes [5]. In 1973, the idea of a satellite constellation capable of providing a user with an accurate position anywhere on the surface of the Earth began to become a reality. A Joint Program Office was formed and the development of the global positioning system (GPS) began. Although an initial design was disapproved by the Department of Defense (DoD), the DoD approved a proposed system developed from the synthesis of previous designs in December 1973. The initial approval was for 24 GPS satellites, with the first phase consisting of four satellites. In February 1978, the first satellite was launched into orbit. Over the course of the next 15 years, the GPS constellation was expanded to the approved 24 satellites. The GPS constellation became fully operational in July 1995 [6]. Today the constellation consists of 32 satellites, and 12 new Block IIF GPS satellites currently being developed and built by Boeing [7].

GPS operates on a system similar to long range navigation and the TRANSIT system. The GPS consists of a space, control, and user segment. The space segment consists of the GPS satellites and the transmission of the ranging signal. The satellites transmit the ranging signal which is acquired by a GPS receiver, the user segment. The receiver calculates the distance between itself and the satellite based on the time difference between time of transmission and time of reception. The receiver uses the computed distance to calculate its latitude, longitude and altitude in addition to a correction to the user's clock. At least four satellites are needed in order for the receiver to accurately approximate its current location. If any of the four parameters approximated by the receiver are known to the receiver, less than four satellites can be used to determine the current location. The control segment updates the current position and clock corrections of the GPS satellites. Predicted future positions and clock corrections are periodically uploaded to the GPS satellites which are then transmitted as part of the navigation message [8].

The GPS constellation is located at an altitude of approximately 20200 kilometers. The orbital period of each satellite is approximately 12 hours. The GPS satellites are distributed among six circular orbits inclined at 55° from the equator and separated by a right ascension angle of 60° to allow for greatest coverage [9]. The system broadcasts updated ephemeris data once every 30 seconds to GPS receivers. GPS receivers gather new ephemeris data every 30 minutes while each set of ephemeris data is valid for the next four hours. Using the GPS satellites visible to the GPS receiver, pseudorange measurements are calculated and used to approximate the current location of the spacecraft. The accuracy of the position approximation is directly influenced by the geometric delusion of precision (GDOP). GDOP is based on the geometry between the satellites in view and the GPS receiver, or in other words the direction the signals transmitted by the GPS satellite travel to the receiver. The most optimal satellite configuration resulting in low GDOP values and accurate position estimates is one GPS satellite located directly above the receiver and three GPS satellites located approximately 120° apart along the horizon line of the antenna field of view [5].

GPS satellites are commonly used for ground based and aircraft navigation. The system has also been used for space applications. GPS navigation can only be used for vehicles orbiting at altitudes lower than the current altitude of the constellation. The GPS constellation was not developed to include the ability for position determination above its current orbiting altitude. The Space Shuttle currently has GPS receivers located on-board for GPS navigation [10]. Absolute and relative GPS navigation has been performed on the European Space Agency's ATV [11], [12]. Relative GPS navigation is currently being implemented on the Japanese H-II Transfer Vehicle (HTV) [13], [14]. The NASA Constellation Project currently under development will make use of GPS navigation on the Crew Exploration Vehicle (CEV) [15], [16]. In

addition to governmentally sponsored projects, developing commercial transportation systems will also use GPS to assist in space navigation. With the emergence of formation flying in the past decade, multiple studies have been performed on the use GPS and differential GPS for relative spacecraft navigation for formation flying [17], [18].

Studies have been performed comparing the performance of inertial state estimators to relative state estimators [19]. Inertial navigation using a relative state estimator, assuming Lambert targeting, requires the implementation of an additional inertial state filter to estimate the absolute inertial states. Lambert targeting determines the transfer between two positions given the two position vectors and time of flight between them [20]. Errors arise from the sole use of an absolute filter when the relative position is known very well and the absolute position is poorly known due to an ill-conditioned estimation error covariance matrix.

C. Thesis Focus

Methods for relative GPS navigation are explored in this thesis by examining the performance of four different Kalman filter architectures. Relative navigation for two spacecraft is the process of determining estimates of both the position, velocity and attitude of a single spacecraft with respect to the other spacecraft [21]. Relative GPS navigation requires the processing of raw GPS measurements. Multiple possible architectures can be used for relative navigation. The four architectures considered in this thesis are similar in that all are dual inertial state filters, but differ in the measurements each processes. A dual inertial filter estimates the inertial position and velocity states of the two vehicles. The relative states for all four Kalman filters are found by differencing the chaser and target inertial states. The four architectures that are focused upon in this work are a position-velocity (PV) extended Kalman

filter (EKF), a relative pseudorange (RGPS) EKF, a pseudorange (GPS) EKF, and a reduced GPS EKF.

The PV EKF uses GPS measurements to estimate the inertial position and velocity vectors of the two spacecraft. The GPS receiver provides the filter with estimates of its current three-dimensional position and velocity vectors. The PV filter is thought to be the simplest filter and easiest to implement since it takes advantage of all the computations done by the receiver. One disadvantage is the inability of the filter to determine the size and direction of the error. Since the filter processes estimated position and velocity measurements, the filter cannot determine which satellites are used to calculate the estimated measurements and therefore cannot determine error directionality. Specifications on the size of the position and velocity errors are given as overall error values instead of individual error values of each axis. When designing the PV EKF, the overall error values of both the position and velocity errors are assigned to all three directions causing conservative predictions of the estimation errors by the estimation error covariance matrix. In order to determine the size of the errors in each direction, the computations taking place inside the GPS receiver need to be recalculated, hence voiding the advantage of using GPS position and velocity measurements. This uncertainty increases the uncertainty in the relative information obtained from the PV EKF.

Perhaps the most commonly used relative GPS filter is the RGPS EKF [12], [13]. The RGPS EKF processes relative pseudorange measurements. While the filter performs well for relative position and velocity estimation, the filter does not provide accurate estimates for inertial position and velocity. Knowledge of inertial position and velocity is still desired despite the main focus of relative navigation. Spacecraft that have implemented a RGPS EKF in the past relied on an external absolute navigation filter in order to acquire accurate estimates of inertial states [12]. Both

filters use the same GPS measurements to perform the state estimation. Since the same measurements are processed, the same measurement noise corrupts the measurements. Although this is the case, the two filters approximate the measurement noise independently and assume no correlation between the measurements being processed. As a result, this procedure is less theoretically sound as opposed to a single filter that performs well in inertial and relative state estimation.

The GPS EKF processes pseudorange measurements to estimate the inertial position and velocity of each spacecraft. The GPS EKF is often more complex due to an addition of numerous states in an attempt to estimate the common measurement noise. Much of the noise corrupting the pseudorange measurements is common between satellites due to the domination of the ionosphere error. By correctly modeling the common error, accurate relative information can be obtained. However, the GPS EKF has a higher computational cost.

The reduced GPS EKF attempts to take advantage of the performance of a GPS EKF without the complexity of the filter. As is the case for the GPS EKF, the reduced GPS EKF processes pseudorange measurements in order to estimate the inertial position and velocity of the spacecraft. The difference in the filters is in the states estimated. The reduced GPS EKF includes the additional states for measurement noise estimation but does not estimate the additional states. Although the additional states are not estimated, entries in the estimation error covariance corresponding to the additional states are allowed to evolve with time thus influencing the state estimation of the inertial position and velocity of the spacecraft. The covariance of the white sequence is increased to the steady state standard deviation of the common measurement noise. Bookkeeping of which satellites are being processed is avoided.

A trade study is performed on the four Kalman filters to determine and outline the advantages and disadvantages of using each filter for relative GPS navigation.

D. Thesis Approach and Outline

The primary focus of this thesis is an assessment of the advantages and disadvantages of different Kalman filter designs used for relative GPS navigation. This thesis develops a mathematical model of a GPS sensor for an orbiting spacecraft. Based upon the measurements from the GPS sensors, a trade study is performed on four Kalman filter designs in order to determine the pros and cons of each filter used for relative GPS navigation.

Chapter II explores the development of the mathematical model of the GPS sensor. An error budget for the GPS model is presented along with algorithms used for position and velocity determination based upon GPS measurements. Chapter IV documents a GPS satellite visibility analysis performed for variable receiver fields of view. Chapter V describes the theory behind the Kalman filter along with the parameters used during the implementation of the four Kalman filters. Design specifications of the four Kalman filters are documented and the theory behind the development of each is explored. Chapter VI presents the results and analysis of Monte Carlo runs performed on each filter. Conclusions from the trade study performed are documented in Chapter VII.

CHAPTER II

GPS SENSOR MODEL

A mathematical model for the GPS sensor onboard the chaser and target vehicles are developed in this chapter. The measurements from the GPS model are pseudoranges, deltaranges, estimated position, estimated velocity, GPS satellite identification numbers and position delusion of precision (PDOP) values. An error budget is performed on the developed sensor model is also included.

A. Pseudorange Errors

A measured pseudorange is needed to approximate the current position of the receiver. The pseudorange is defined as the distance between a particular GPS satellite at the time of signal transmission and the GPS receiver at the time of signal reception. Due to the nature of the atmosphere, clock drifting and data transmission, the exact pseudorange cannot be accurately calculated. There are six primary sources of error that affect the calculation of the pseudorange: ionosphere, troposphere, receiver clock noise, GPS satellite clock bias, multipath and ephemeris. Ionosphere, troposphere and multipath errors are all the result of time delays and therefore are always positive. Receiver clock noise, GPS satellite clock bias and ephemeris errors are due to data and clock drifting resulting in both positive and negative values. In addition to these six error sources, there is also a bias in the onboard clock of the GPS receiver. The measured pseudorange is modeled by the following equation [9]:

$$\rho_i = \|\mathbf{r}_{rec} - \mathbf{r}_{gps_i}\| + \mathrm{c}(\epsilon_{iono_i} + \epsilon_{trop_i} + \epsilon_{mult_i} + \epsilon_{rcb} + \epsilon_{scb_i}) + \epsilon_{eph_i} + \epsilon_{\eta} \tag{2.1}$$

$\mathbf{r}_{\text{rec}}$: position of receiver at time of signal reception (m)

$\mathbf{r}_{\text{gps}_i}$: position of the ithGPS satellite at time of signal transmission (m)

c : speed of light = $2.99792458 \cdot 10^8 \ \frac{\text{m}}{\text{s}}$

ϵ_{iono_i} : error due to ionosphere time delay of the ithGPS satellite (s)

ϵ_{trop_i} : error due to troposphere time delay of the ithGPS satellite (s)

ϵ_{mult_i} : error due to multipath time delay of the ithGPS satellite (s)

ϵ_{rcb} : error due to receiver clock bias (s)

ϵ_{scb_i} : error due to GPS satellite clock bias of the ithGPS satellite (s)

ϵ_{eph_i} : error due to ephemeris data variations of the ithGPS satellite (m)

ϵ_{η} : error due to receiver clock noise (m)

The speed at which transmitted data travels through space is approximately the speed of light. Since the distance between two satellites is measured in units of length and time delays are measured in units of time, the speed of light is used to ensure consistency of units. For each GPS satellite in view of the receiver, a separate corresponding pseudorange is calculated.

1. Receiver Clock Bias

Each receiver clock differs in the accuracy built into it. The accuracy of the receiver clock is substantially less than the accuracy of the GPS satellite clocks, since the receiver clock is not atomic and the offset of the clock is unknown. As a result, the "random walking" of the receiver clock will result in an error in the calculation of the current position of the receiver. The continuous time model for the 2^{nd} order random walk used to simulate the inaccuracies of the receiver clock producing the errors is given by Equation 2.2.

$$\dot{\mathbf{x}}(t) = \begin{bmatrix} 0 & 0 \\ 1 & 0 \end{bmatrix} \mathbf{x}(t) + \mathbf{w}(t) \tag{2.2}$$

where the vector $\mathbf{w}(t)$ is a zero-mean white noise process and the state vector $\mathbf{x}(t)$ comprises the clock bias and drift. The corresponding discrete form of 2^{nd} order random walk model found by sampling the continuous model at a time interval of Δt is given by the following equations [9].

$$\mathbf{x}_{\mathrm{k}} = \mathbf{\Phi}(\Delta \mathrm{t})\mathbf{x}_{\mathrm{k}-1} + \mathbf{Q}\mathbf{w}_{\mathrm{k}-1} \tag{2.3a}$$

$$\mathbf{x}_{\mathrm{k}} = [\, \mathrm{b_k} \quad \mathrm{f_k} \,]^{\mathrm{T}} \tag{2.3b}$$

where b_k is the receiver clock bias given as ϵ_{rcb} in Equation 2.1 and f_k is the clock drift. The vector $\mathbf{w}_{\mathrm{k}-1}$ is a zero-mean white noise sequence. The discrete sample time is Δt. $\mathbf{\Phi}$ and $\mathbf{Q}$ are given as the following matrices.

$$\mathbf{\Phi} = \begin{bmatrix} 1 & \Delta t \\ 0 & 1 \end{bmatrix}$$

$$\mathbf{Q} = \begin{bmatrix} S_b \Delta t + S_f \frac{\Delta t^3}{3} & S_f \frac{\Delta t^2}{2} \\ S_f \frac{\Delta t^2}{2} & S_f \Delta t \end{bmatrix}$$

$$S_b = 4 \times 10^{-19}\ (\mathrm{s})$$

$$S_f = 16\pi^2 \times 10^{-20}\ (\tfrac{1}{\mathrm{s}})$$

S_f and S_b are white noise spectral density coefficients for a compensated crystal clock [22]. For receiver clock errors given in meters, the spectral density coefficients are multiplied by the speed of light for consistent units.

2. Ionosphere Model

The ionosphere is a layer of ionized particles that extends from 50 to 1000 kilometers above the surface of the Earth. GPS satellites are located at an altitude of approximately 20,000 km above the surface of the Earth therefore the transmitted signals from the GPS satellites frequently pass through the ionosphere. The Klobuchar model is used to approximate the effects of the ionosphere [23]. Coefficients needed in the Klobuchar model are broadcast in the GPS ephemeris and are received every 30 minutes. Three cases are considered when calculating the time delay due to the presence of the ionosphere. Since the ionosphere has finite limits the time delay will vary if the receiver is below the lower level of the ionosphere, inside the ionosphere, or above the upper level of the ionosphere. This research applies to any satellite in lower earth orbit (LEO). The orbit of the ISS is located approximately 250 kilometers above the surface of the Earth placing the ISS and chasing spacecraft inside the ionosphere. The model used during this research is that of Reference [24]. Appendix A contains a detailed derivation of the ionosphere time delay.

3. Troposphere Model

The troposphere is the lowest and densest portion of the atmosphere. The troposphere ranges from sea level to approximately 50 kilometers above the surface of the Earth. As a result, the troposphere has little to no impact on the for LEO satellites. For completeness and validation purposes, the troposphere model is included in the overall GPS model. Hopfield's troposphere model is used to approximate the time delay due to GPS signals passing through the troposphere [25]. As is the case for the ionosphere, multiple cases are considered during the calculation of the troposphere delay. The troposphere is separated into two layers - wet and dry. The wet layer extends from

sea level to eleven kilometers and the dry layer extends from 11 to 50 kilometers. Depending on the location of the spacecraft, the appropriate equation is used to calculate the troposphere delay. A detailed derivation of the time delay due to the presence of the troposphere is given in Appendix B.

4. Satellite Clock Error

GPS satellites have four built in atomic clocks - two cesium and two rubidium. The redundancy of multiple clocks in each GPS satellite results in a high stability of one part in 10^{13} per day. Although the atomic clocks are highly accurate, GPS satellite clocks cannot remain synchronized with one another. As a result, an error of 10^{-8} seconds or 3.5 meters per day due to clock drift is expected [5].

For modeling purposes, a discrete Gauss-Markov process is used to model the satellite clock drift, shown by Equation 2.4 [22].

$$\mathbf{x}_{k+1} = e^{-\frac{\Delta t}{\tau_{sce}}}\mathbf{x}_k + \mathbf{w}_k \tag{2.4}$$

where the vector $\mathbf{w}_k$ is a zero mean white sequence with length equal to the number of active GPS satellites. The number of active satellites varies from 24 to 32 due to the deactivation and re-activation of satellites over time. As a result, the model is designed to accept a variable number of active satellites. Since the clock bias is represented by a discrete model, k represents the current time step. The covariance matrix corresponding to the white noise is given by

$$E\left\{\mathbf{w}_k\mathbf{w}_j^T\right\} = \begin{cases} \mathbf{0} & k \neq j \\ \mathbf{Q}_k & k = j \end{cases} \tag{2.5}$$

The covariance, $\mathbf{Q}_k$, as defined in Equation 2.5 is given by Equation 2.6. The steady state standard deviation of the satellite clock error is given by $\sigma_{sce_{ss}}$ and the

time constant τ_{sce} is modeled to be 30 minutes since this is the rate at which GPS ephemerides information is received [5].

$$\mathbf{Q}_k = \sigma^2_{sce_{ss}}(1 - e^{-\frac{2\Delta t}{\tau_{sce}}}) \tag{2.6}$$

Since errors in the satellite clock are essentially the same for spaceborne and ground based GPS receivers, the error corresponding to the satellite clock error for a ground based receiver of 1-2 meters given in Reference [5] is used as a guideline for calibrating the satellite clock error of the GPS sensor model. The initial variance is set equal to the square of the average error given of 1.75 meters with the final variance being twice the initial variance. The resulting value from the discrete Gauss-Markov process is in the form of a time delay hence the multiplication of the value by the speed of light in Equation 2.1.

5. Receiver Clock Noise

In addition to the low frequency error, there is also a high frequency receiver clock error. A first order Gauss-Markov process identical to the Gauss-Markov process described for the error due to the satellite clock bias is used to model the receiver noise. Since pseudoranges arrive at different times from each visible satellite, the receiver noise corrupting each pseudorange measurement is different. The variance of the receiver noise, σ^2_n, is modeled as 0.5 square meters corresponding to the receiver clock error for a ground based GPS receiver [25]. The time constant of the receiver noise, τ_n, is modeled as 0.1 seconds therefore the modeled error is essentially a white noise with a variance of 0.5 square meters. The variance and time constant of the receiver noise are substituted into Equation 2.4 and Equation 2.6 in place of the variance and time constant corresponding to the satellite clock error.

6. Multipath Error

Multipath error is a result of the broadcast signal bouncing off adjacent objects and interfering with the direct path of the signal to the receiver's antenna resulting in a delay. Multipath errors are difficult to accurately model due to the complexity in geometric shapes of the surrounding environment and the irregularity and unpredictability of the signal bouncing. Each GPS satellite results in an entirely unique multipath error due to the varying geometry and signal path from GPS satellite to receiver. Multipath error models exist requiring individual frequencies relating to each GPS satellite that include a Doppler shift as well as each GPS satellite signal power coming into the receiver, both of which proved difficult to approximate [26]. As a result, an alternate model of the multipath time delay is implemented.

A first order Gauss-Markov process is used to model the multipath time delay. The Gauss-Markov process implemented is identical to the Gauss-Markov process used to model the GPS satellite clock bias, Equations 2.4-2.6. In this thesis, calibrations are performed on the multipath error in order to achieve errors within the range of References [5], [27], [25], [9]. A steady state standard deviation of 0.5 meters for the chaser and 2.0 meters for the target vehicle is implemented and held constant over the entire simulation. The time constant of the Gauss-Markov processes for both vehicles is 200 seconds. The steady state standard deviation of the target vehicle is chosen to be four times higher due to the complexity in geometry of the target vehicle's structure.

7. Ephemeris Error

Every 30 seconds, GPS satellites broadcast a set of ephemeris data and the GPS receivers update their ephemeris data approximately every 30 minutes. There are

slight errors in the ephemeris parameters transmitted in the ephemeris data. Due to these errors, the resulting calculations of the GPS satellite positions do not represent the exact current location of the GPS satellites. The median position errors in Local Vertical Local Horizontal (LVLH) frame over a 12 hour period are 1.2 meters radially, 4.5 meters along track and 3.2 meters cross track [5]. Figure 1 shows the LVLH frame with respect to the Earth Centered Inertial (ECI) where the x-axis of the LVLH frame is aligned with the direction of motion (into the page).

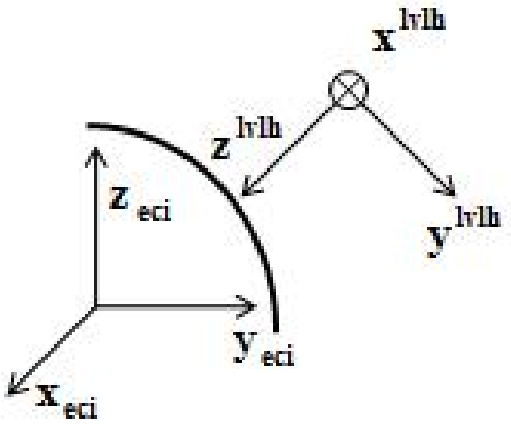

Fig. 1. LVLH Frame

In order to model the ephemeris errors, an integrated Gauss-Markov process is implemented. Equation 2.7 is implemented with parameters defined by successive vector and matrix definitions [22].

$$\mathbf{x}_{k+1}^{lvlh} = \mathbf{\Phi}_k \mathbf{x}_k^{lvlh} + \mathbf{w}_k \tag{2.7}$$

$$\mathbf{x}_k^{lvlh} = [e_x \;\; e_y \;\; e_z \;\; e_{\dot{x}} \;\; e_{\dot{y}} \;\; e_{\dot{z}}]^T$$

$$\mathbf{\Phi}_k = \begin{bmatrix} \mathbf{I}_{3x3} & \mathbf{I}_{3x3} \cdot \tau_{eph}(1 - e^{-\frac{\Delta t}{\tau_{eph}}}) \\ \mathbf{0}_{3x3} & \mathbf{I}_{3x3} \cdot e^{-\frac{\Delta t}{\tau_{eph}}} \end{bmatrix}$$

where the vector $\mathbf{w}_k$ is a zero mean white noise sequence. The covariance matrix corresponding the the Gauss-Markov process described in Equation 2.7 is as follows:

$$E\left\{\mathbf{w}_k \mathbf{w}_j^T\right\} = \begin{cases} \mathbf{0} & k \neq j \\ \mathbf{Q}_k & k = j \end{cases}$$

where

$$\mathbf{Q}_k = \begin{bmatrix} \mathbf{Q}_{11} & \mathbf{Q}_{12} \\ \mathbf{Q}_{21} & \mathbf{Q}_{22} \end{bmatrix}$$

The covariance matrix $\mathbf{Q}_k$ is populated by the smaller covariance matrices given by Equations 2.9-2.10 [22].

$$\mathbf{Q}_{11} = 2\sigma^2\tau_{eph}(\Delta t - 2\tau_{eph}(1 - e^{-\frac{\Delta t}{\tau_{eph}}}) + \frac{\tau_{eph}}{2}(1 - e^{-\frac{2\Delta t}{\tau_{eph}}}))\mathbf{I}_{3\times3} \quad (2.8)$$

$$\mathbf{Q}_{12} \equiv Q_{21} = \sigma^2\tau_{eph}(2(1 - e^{-\frac{\Delta t}{\tau_{eph}}}) - (1 - e^{-\frac{2\Delta t}{\tau_{eph}}}))\mathbf{I}_{3\times3} \quad (2.9)$$

$$\mathbf{Q}_{22} = \sigma^2(1 - e^{-\frac{2\Delta t}{\tau_{eph}}})\mathbf{I}_{3\times3} \quad (2.10)$$

As previously mentioned, the median ephemeris error is known for 12 hour periods of time. In order to implement the Gauss-Markov process, initial conditions are needed on the initial error vectors as well as the initial covariance matrix. Using the given median daily position errors, the final covariance matrix representing the uncertainty in the position errors is chosen to be two times the square of the median standard deviation as shown in Equation 2.11 while the initial covariance matrix is chosen to be one fourth of the final covariance matrix.

$$\mathbf{Q}_{11_k}(t_f) = 2 \begin{bmatrix} 4.5^2 & 0 & 0 \\ 0 & 3.2^2 & 0 \\ 0 & 0 & 1.2^2 \end{bmatrix} \tag{2.11}$$

Equating Equation 2.11 to $\mathbf{Q}_{11}$ as defined by Equation 2.9 while setting Δt to be the final time of 12 hours and choosing τ_{eph} to be 30 minutes (the frequency of the reception of ephemeris data), it is possible to solve for the variance corresponding to each position error. The resulting variance vector is defined by Equation 2.12.

$$\boldsymbol{\sigma}^2 = 1\mathrm{e}^{-6} \begin{bmatrix} 0.1405 \\ 0.2778 \\ 0.0198 \end{bmatrix} \tag{2.12}$$

The vector squaring notation in Equation 2.12 represents the squaring of each individual term of the vector $\boldsymbol{\sigma}$. Once the variance is determined, the covariance matrix $\mathbf{Q}_k$ at each time step is determined using Equations 2.9-2.10 during the simulation using Δt equal to the simulation time step and holding τ_{eph} constant at 30 minutes.

B. Delta Range and Range Rate

Range rate is defined as the rate of change of the distance between a GPS receiver and a single GPS satellite. The range rate is used to compute the deterministic velocity solution. Delta range is defined as the difference between two consecutive pseudorange measurements taken within a given time interval. The pseudorange is calculated using Equation 2.1. Let the acquisition time interval be defined as δt. The acquisition time interval varies based on the receiver but is 0.1 seconds for the study performed in this thesis. The true range rate is defined by Equation 2.13.

$$\dot{\rho}_i = \frac{\boldsymbol{\rho}_i \cdot \dot{\boldsymbol{\rho}}_i}{\rho_i} \tag{2.13}$$

where

$$\boldsymbol{\rho}_i = \mathbf{r}_{\mathbf{gps_i}} - \mathbf{r}_{rec}$$

$$\dot{\boldsymbol{\rho}}_i = \mathbf{v}_{gps_i} - \mathbf{v}_{rec}$$

While range rate measurements from Doppler effects exist, delta range measurements from integrated carrier phase are more common. Two first order Gauss-Markov processes are used to approximate the range rate error. The Gauss-Markov processes model the portion of the error unique to each satellite and the portion of the the error unique to the receiver. The overall steady state standard deviation of the range rate error is 0.1 meters per second [27]. There is a contribution to the range rate from the receiver and GPS satellite. In order to model each of these contributions, two first order Gauss-Markov processes are used with the variance of each process equal to half of the total variance. The time constant corresponding to the receiver contribution is 1 second while the time constant corresponding to the GPS satellite contribution is 60 seconds. The total range rate error is depicted by Equation 2.14 and the Gauss-Markov process model is given by Equation 2.15.

$$\mathbf{x}_{tot} = \mathbf{x}_{\mathbf{sat}} + \mathbf{x}_{\mathbf{rec}} \tag{2.14}$$

$$\mathbf{x}_{k+1} = e^{-\frac{\Delta t}{\tau}} \mathbf{x}_k + \mathbf{w}_k \tag{2.15}$$

Equation 2.15 is used to model both contributions to the total range rate model

with a corresponding covariance value $\mathbf{Q}$ for each modeled contribution given by Equation 2.16. The steady state standard deviation and time constant differ for each contribution.

$$\mathbf{Q_{cont}} = \sigma_{cont}^2 \left(1 - e^{\frac{-2\Delta t}{\tau_{cont}}}\right) \tag{2.16}$$

Although the contribution from the GPS receiver is unique to a single receiver, the time of reception of GPS satellite signals by the receiver varies. Therefore, the noise contribution from the GPS receiver for each range rate corresponding to different GPS satellites differs for each time interval due to the slight variation in reception time. Since the two contributions to the range rate error are not correlated, the total covariance is the sum of the individual covariances as shown in Equation 2.17.

$$\mathbf{Q_{tot}} = \mathbf{Q_{sat}} + \mathbf{Q_{rec}} \tag{2.17}$$

C. GPS Satellite Position and Velocity

The position and velocity of each GPS satellite are calculated via GPS ephemerides which are transmitted from the GPS satellites once every 30 seconds and received by the GPS receiver once every 30 minutes on-board the spacecraft. The broadcast GPS ephemerides are valid for up to four hours after the time of transmission to allow for instances when the GPS ephemerides are not acquired by the receiver during successive data transmissions. In order to calculate the position of the GPS satellites, a step by step process is followed [5]. In the process, the position is initially defined in a body frame and is then transformed into an Earth Centered Earth Fixed (ECEF) frame. The position is also needed in the Earth Centered Inertial (ECI) frame. The position of the GPS satellites in both ECEF and ECI frames [2] is given as

$$\begin{aligned} \mathbf{r}_{lvlh} &= [x_k \; y_k \; z_k]^T \\ \mathbf{r}_{ecef} &= \mathbf{C}_{\mathbf{ecef}}^{\mathbf{lvlh}\,T} \mathbf{r}_{lvlh} \\ \mathbf{r}_{eci} &= \mathbf{C}_{\mathbf{ecef}}^{\mathbf{eci}} \mathbf{r}_{ecef} \end{aligned}$$

$$\begin{aligned} \mathbf{r}_{lvlh} &: \text{position of spacecraft in LVLH frame (m)} \\ \mathbf{r}_{ecef} &: \text{position of spacecraft in ECEF frame (m)} \\ \mathbf{r}_{eci} &: \text{position of spacecraft in ECI frame (m)} \end{aligned}$$

where

$$\begin{aligned} \theta_k &= f_k + \omega_k \\ \tilde{\theta}_k &= \theta_k + \zeta_{corr_k} \\ x_k &= r_k \cos(\tilde{\theta}_k) \\ y_k &= r_k \sin(\tilde{\theta}_k) \\ z_k &= 0 \end{aligned}$$

$$\begin{aligned} r_k &: \text{distance from receiver to center of earth (m)} \\ f_k &: \text{true anamoly (rad)} \\ \omega_k &: \text{argument of periapsis (rad)} \\ i_k &: \text{inclination (rad)} \\ \Omega_k &: \text{longitude of ascending node (rad)} \\ \zeta_{corr_k} &: \text{correction term determined from GPS ephemeris (rad)} \end{aligned}$$

and the transformation matrices $\mathbf{C}_{\mathbf{ecef}}^{\mathbf{lvlh}\,T} \mathbf{r}_{lvlh}$ and $\mathbf{C}_{\mathbf{ecef}}^{\mathbf{eci}} \mathbf{r}_{ecef}$ are given as follows:

$$\begin{aligned} \mathbf{C}_{\mathbf{ecef}}^{\mathbf{lvlh}} &= R_1(i_k)R_3(\Omega_k) \\ \mathbf{C}_{\mathbf{ecef}}^{\mathbf{eci}} &= R_3(\Omega_0 + \dot{\Omega}_E t_k) \end{aligned}$$

$$\begin{aligned} \Omega_E &: \text{ angular velocity of the earth} \sim 7.2921151467 \times 10^{-5} \tfrac{rad}{s} \\ \Omega_0 &: \text{ initial angle of longitude of ascending node (rad)} \end{aligned}$$

The rotation matrices $\mathbf{R}_1$ and $\mathbf{R}_3$ are defined as

$$\mathbf{R}_1(i_k) = \begin{bmatrix} 1 & 0 & 0 \\ 0 & \cos i_k & \sin i_k \\ 0 & -\sin i_k & \cos i_k \end{bmatrix}$$

$$\mathbf{R}_3(\Omega_k) = \begin{bmatrix} \cos\Omega_k & \sin\Omega_k & 0 \\ -\sin\Omega_k & \cos\Omega_k & 0 \\ 0 & 0 & 1 \end{bmatrix}$$

The velocity of each GPS satellite is computed by taking the time derivative of the position vector. The following equations give the velocity of the GPS satellites in the LVLH and ECEF frames taking into account a time varying orbit radius. [28]

$$\begin{aligned} v_{x_k} &= \dot{r}_k cos(\tilde{\theta}_k) - y_k \dot{\tilde{\theta}}_k \\ v_{y_k} &= \dot{r}_k sin(\tilde{\theta}_k) + x_k \dot{\tilde{\theta}}_k \\ v_{z_k} &= 0 \\ \mathbf{v}_{lvlh} &= [v_{x_k}\ v_{y_k}\ v_{z_k}]^T \end{aligned}$$

$$
\begin{aligned}
\dot{X}_k &= (v_{x_k} - y_k\dot{\Omega}_k\cos(i_k))\cos(\Omega_k) - (y_k\sin(i_k)\dot{i}_k - v_{y_k}\cos(i_k) - x_k\dot{\Omega}_k)\sin(\Omega_k) \\
\dot{Y}_k &= (v_{x_k} - y_k\dot{\Omega}_k\cos(i_k))\sin(\Omega_k) + (x_k\dot{\Omega}_k + v_{y_k}\cos(i_k) - y_k\sin(i_k)\dot{i}_k)\cos(\Omega_k) \\
\dot{Z}_k &= v_{y_k}\sin(i_k) + y_k\cos(i_k)\dot{i}_k \\
\mathbf{v}_{ecef} &= [\dot{X}_k\ \dot{Y}_k\ \dot{Z}_k]^T
\end{aligned}
$$

The velocity of the GPS satellites in the ECI frame is:

$$\mathbf{v}_{eci} = \mathbf{C}^{\mathbf{eci}}_{\mathbf{ecef}}\mathbf{v}_{ecef} + (\dot{\mathbf{\Omega}}_E \times \mathbf{r}_{ecef})$$

The $\times$ symbol denotes the cross product between the two given vectors.

D. GPS Receiver Position Estimation

Position estimates of the GPS receiver are determined using a deterministic solution to the GPS problem. The algorithm, known as Bancroft least squares [29], requires knowledge of position vectors of the visible GPS satellites (easily calculated from transmitted ephemeris data) and the corresponding pseudorange measurements. Being a deterministic solution, Bancroft least squares requires at least four GPS satellites in order to approximate the position and time error of the receiver.

1. Bancroft Least Squares

The following derivation can be found in depth in Reference [29]. Measurements are sampled at a fixed sample period specified for the GPS receiver. Let ρ_i be the pseudorange measurements taken by the receiver for the i^{th} GPS satellite. Let N be the total number of pseudorange measurements of the visible satellites. It is assumed the pseudorange measurements have included errors due to receiver clock bias. Define

the vectors $\boldsymbol{\alpha}$ to be

$$\boldsymbol{\alpha}_i = [\mathbf{s}_i^T \ \rho_i]^T, \qquad \text{for } i = 1...N \tag{2.18}$$

where $\mathbf{s}_i^T$ is the position coordinates of the i^{th} GPS satellite given in ECI coordinates and ρ_i is the corresponding measured pseudorange. The Minkowski function for four dimensional space is defined by Equation 2.19.

$$\langle \boldsymbol{\xi}, \boldsymbol{\eta} \rangle = \boldsymbol{\xi} \cdot \boldsymbol{\eta} - 2\,\xi_4\,\eta_4 \tag{2.19}$$

Making using of Equation 2.19 allows for the definition of the auxiliary variable χ_i.

$$\boldsymbol{\chi}_i = \frac{\langle \boldsymbol{\alpha}_i, \boldsymbol{\alpha}_i \rangle}{2} \tag{2.20}$$

Once all α and χ have been assembled, define the following matrix and vectors for future use.

$$\mathbf{A} = [\boldsymbol{\alpha}_1 \ \ \boldsymbol{\alpha}_2 \ \ \boldsymbol{\alpha}_3 \ \ \cdots \ \ \boldsymbol{\alpha}_N]^T \tag{2.21a}$$

$$\boldsymbol{\gamma} = [1 \ \ 1 \ \ 1 \ \ \cdots \ \ 1]^T \tag{2.21b}$$

$$\boldsymbol{\chi} = [\chi_1 \ \ \chi_2 \ \ \chi_3 \ \ \cdots \ \ \chi_N] \tag{2.21c}$$

where $\mathbf{A}$ is an N $\times$ 4 matrix and $\boldsymbol{\gamma}$ and $\boldsymbol{\chi}$ are [N x 1] column vectors. The inclusion of the weighting matrix, $\mathbf{W}$, allows for scaling when desired. In this thesis, $\mathbf{W}$ is chosen to be the identity matrix. In general, $\mathbf{W}$ is a symmetric positive definite matrix.

$$\mathbf{B} = (\mathbf{A}^T\mathbf{W}\mathbf{A})^{-1}\mathbf{A}^T\mathbf{W} \tag{2.22}$$

Define vectors $\mathbf{u}$ and $\mathbf{v}$ as

$$\mathbf{u} = \mathbf{B}\boldsymbol{\gamma} \tag{2.23}$$

$$\mathbf{v} = \mathbf{B}\boldsymbol{\chi} \tag{2.24}$$

Compute the coefficients to be used with the quadratic defined by Equation 2.26.

$$X = \langle \mathbf{u}, \mathbf{u} \rangle \tag{2.25a}$$

$$Y = \langle \mathbf{u}, \mathbf{v} \rangle - 1 \tag{2.25b}$$

$$Z = \langle \mathbf{v}, \mathbf{v} \rangle \tag{2.25c}$$

Solving the quadratic for λ

$$X\lambda^2 + 2Y\lambda + Z = 0 \tag{2.26}$$

results in two solutions. Two position and clock bias estimates are calculated by substituting the solution to Equation 2.26 into Equation 2.27.

$$\mathbf{y}_{est} = \lambda\mathbf{u} + \mathbf{v} = [\mathbf{r}_{rec_e} \quad -b_e]^T \tag{2.27}$$

The estimated position vector $\mathbf{r}_{rec_e}$ is given in the ECI reference frame. Only one of the two solutions calculated from Equation 2.27 provides a correct position estimate of the GPS receiver. In order to distinguish the extraneous solution from the actual solution, the estimated position and clock bias is substituted into the pseudorange equation given by Equation 2.28 and compared with the measured pseudorange. The pseudorange calculated with the extraneous solution will not match the measured pseudorange whereas the pseudorange calculated via the actual solution will be nearly

identical.

$$\rho_{i_{est}} = \|\mathbf{s}_i - \mathbf{r}_{rec_e}\| + c \cdot b_e \tag{2.28}$$

E. GPS Receiver Velocity Estimation

The deterministic velocity solution is simpler than the position deterministic solution since velocity enters the range rate equation linearly. The velocity estimate algorithm is the least squares solution. It requires knowledge of estimated receiver position, position and velocity of each GPS satellite, and range rate measurements. A similar algorithm is derived in Reference [30] where the velocity vector is determined using the same required variable knowledge, except the algorithm did not provide a solution for the clock drift. The algorithm below is developed from the time derivative the the pseudorange equation and includes a solution to the clock drift not given in Reference [30] along with the velocity of the GPS receiver.

1. Algorithm Derivation

To begin, determine the distance d_i between the receiver and each GPS satellite where i denotes the i^{th} satellite. Then take the time derivative of the distance to get a distance rate.

$$d_i^2 = \mathbf{x}^T\mathbf{x} - 2\mathbf{s}_i^T\mathbf{x} + \mathbf{s}_i^T\mathbf{s}_i$$

$$\frac{\mathrm{d}}{\mathrm{dt}}(d_i^2) = \frac{\mathrm{d}}{\mathrm{dt}}(\mathbf{x}^T\mathbf{x} - 2\mathbf{s}_i^T\mathbf{x} + \mathbf{s}_i^T\mathbf{s}_i)$$

$$d_i\dot{d}_i = (\mathbf{x} - \mathbf{s}_i)^T\dot{\mathbf{x}} + (\mathbf{s}_i - \mathbf{x})^T\dot{\mathbf{s}}_i \tag{2.29}$$

where the vector $\mathbf{x}$ is the estimated position of the receiver, $\mathbf{s}_i$ is the position of the i^{th} GPS satellite, $\dot{\mathbf{x}}$ is the velocity of the receiver to be estimated, and $\dot{\mathbf{s}}_i$ is the velocity of the i^{th} single GPS satellite.

Taking the time derivative of the pseudorange equation results in

$$\frac{\mathrm{d}}{\mathrm{dt}}(\rho_i) = \frac{\mathrm{d}}{\mathrm{dt}}(d_i + cb)$$

$$\dot{\rho}_i = \dot{d}_i + c\dot{b} \tag{2.30}$$

Note that ρ_i is the pseudorange for each GPS satellite, d_i is the distance to each satellite, c is the speed of light, and b is the receiver clock bias. In addition, $\dot{\rho}_i$ is the range rate corresponding to each GPS satellite, $\dot{d}_i$ is the rate at which the distance is changing between the receiver and the GPS satellite and $\dot{b}$ is the receiver clock drift. Solving Equation 2.30 for $\dot{d}_i$ and substituting into Equation 2.29 leads to

$$d_i(\dot{\rho}_i - \dot{B}) = (\mathbf{x} - \mathbf{s}_i)^T\dot{\mathbf{x}} + (\mathbf{s}_i - \mathbf{x})^T\dot{\mathbf{s}}_i \tag{2.31}$$

Let B be defined as the product of c and b. Define $\mathbf{R}_i = \mathbf{s}_i - \mathbf{x}$. Implementing the definition and rearranging, Equation 2.31 becomes

$$\mathbf{R}_i^T\dot{\mathbf{x}} - d_i\dot{B} = \mathbf{R}_i^T\dot{\mathbf{s}}_i - d_i\dot{\rho}_i \tag{2.32}$$

Let

$$\mathbf{z} = [\dot{\mathbf{x}}^T\ \dot{B}]^T$$

Making use of the definition of $\mathbf{z}$, Equation 2.32 can be rewritten as

$$[\mathbf{R}_i^T \ -d_i]\mathbf{z} = \mathbf{R}_i^T \dot{\mathbf{s}}_i - d_i\dot{\rho}_i \tag{2.33}$$

If $\mathbf{a}_i$ and β_i, where i refers to each GPS satellite, are defined as

$$\mathbf{a}_i = [\mathbf{R}_i^T \ -d_i]^T$$

$$\beta_i = \mathbf{R}_i^T \dot{\mathbf{s}}_i - d_i\dot{\rho}_i$$

the matrices $\mathbf{A}$ and $\mathbf{y}$ can be formulated as

$$\mathbf{A} = [\mathbf{a}_1 \ \mathbf{a}_2 \ \mathbf{a}_3 \ \cdots \ \mathbf{a}_n]^T$$

$$\mathbf{y} = [\beta_1 \ \beta_2 \ \beta_3 \ \cdots \ \beta_n]^T$$

Equation 2.33 can be rewritten in a recognizable and easily solvable linear form.

$$\mathbf{Az} = \mathbf{y} \tag{2.34}$$

Matrix $\mathbf{A}$ has dimensions of m $\times$ 4. A weighted least squares algorithm is used to solve for $\mathbf{z}$. Omitting the derivation of the least squares methodology [31], the solution to Equation 2.34 is

$$\mathbf{z} = (\mathbf{A}^T\mathbf{WA})^{-1}\mathbf{A}^T\mathbf{Wy} \tag{2.35}$$

The weight matrix $\mathbf{W}$ is defined to be an identity matrix, $\mathbf{I}_{m\times m}$. If $\mathbf{A}$ is a square matrix, then Equation 2.35 reduces to a more familiar form.

$$\mathbf{z} = \mathbf{A}^{-1}\mathbf{y}$$

Using the above algorithm, the receiver velocity can be estimated using the estimated

position of the receiver and known position and velocity of the GPS satellites in addition to the range rate measurements.

F. GPS Satellite Visibility Validation

For this thesis, the orbit of the International Space Station (ISS) is used as a reference for validation purposes and analysis due to the availability of orbital information pertaining to the ISS. Orbital information for the ISS is updated daily and found in Reference [32]. A validation of the 6 DOF model used to determine the position and velocity of the GPS satellites is performed using initial conditions and parameters corresponding to the ISS. A GPS receiver has an allotted field of view in which transmitted signals from GPS satellites can be received. The antenna field of view is specified by the half cone angle of the antenna. The half cone angle is the angle between the antenna cone and the boresight, as shown in Figure 2.

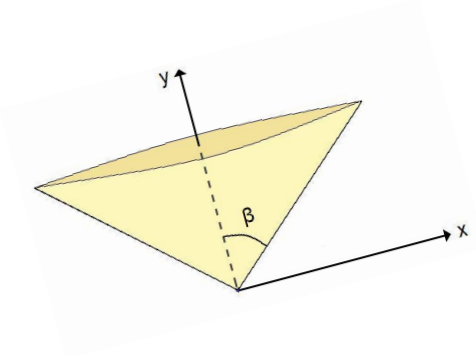

Fig. 2. Antenna Half Cone Angle

A range of half cone angles between 55° - 65° are examined with the two extremes presented. The chaser vehicle is assumed to be on the same orbit as the ISS with

initial conditions as given below.

$$\mathbf{r}_0 = 10^6 \cdot \begin{bmatrix} 3.395964921 \\ 3.604875629 \\ 4.548220882 \end{bmatrix} \text{m}$$

$$\mathbf{v}_0 = 10^3 \cdot \begin{bmatrix} -6.645263099 \\ 2.415260514 \\ 3.047389154 \end{bmatrix} \frac{\text{m}}{\text{s}}$$

A two day period of time is considered during which the chaser's orbit and orbits of the GPS satellites are simulated. The orbit of the chaser vehicle is propagated using a simple two body approach assuming no external accelerations acting upon the system. The orbits of the GPS satellites are propagated via an orbit propagation algorithm [5]. Select orbital elements corresponding to the orbit of the ISS are given as follows:

$$\begin{aligned} i_{ISS} &= 51.39979^\circ \\ \Omega_{ISS} &= 349.81214^\circ \\ \omega_{ISS} &= 156.31946^\circ \end{aligned}$$

Using the above initial conditions, the orbit of the chaser vehicle is propagated for two days and the number of visible GPS satellites is recorded every ten seconds. In addition to the 6 DOF simulation of the GPS orbits, Satellite Tool Kit (STK) is also used to propagate the orbits of both the chaser vehicle and GPS satellites. Providing the same initial conditions and epoch time (date and time) as used in the

6 DOF simulation, a comparable data set is extracted from STK for comparison.

First a half cone angle of 55° is analyzed. The number of GPS satellites visible for both simulations is given by Figure 3. As can be seen upon inspection of Figures 3, the results from the 6 DOF and STK simulations are similar. The maximum difference between the two data sources is approximately 5%.

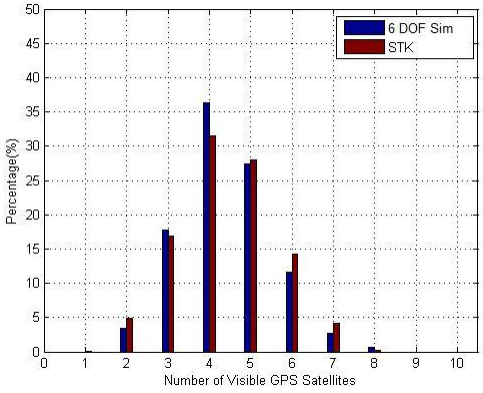

Fig. 3. Comparison of Simulations - Total Number of GPS Satellites Visible for 65° Half Cone Angle

Since four GPS satellites are needed in view to approximate the position of the GPS receiver, percentages pertaining to four GPS satellites in view are given in Table I. The comparisons given in Figure 3 and Table I show the orbit propagation of the 6 DOF simulation resembles the STK simulation.

Table I. Percentage of GPS Satellites Visible - 55° Half Cone Angle

Simulation Method	Percentage < 4	Percentage ≥ 4
6 DOF	21.2674	78.7326
STK	21.7778	78.2222

To ensure the 6 DOF satellite propagation orbit will produce accurate results at multiple antenna half cone angles, a 65° half cone angle is also analyzed. The number of satellites visible for both simulations is given by Figure 4. Although there is a slight discrepancy in the number of satellites visible determined by each simulation method in Figure 4, the percentage of satellites less than the required four needed to determine receiver position is once again less than 1%.

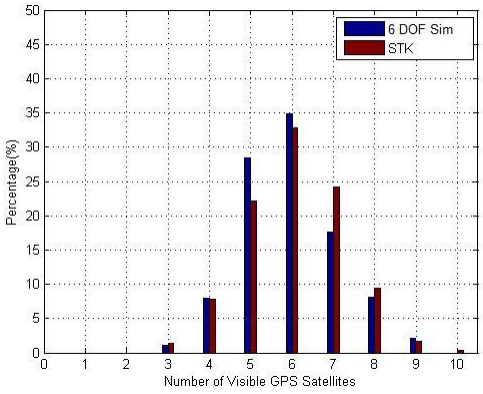

Fig. 4. Comparison of Simulations - Total Number of GPS Satellites Visible for 65° Half Cone Angle

Table II. Percentage of GPS Satellites Visible - 65° Half Cone Angle

Simulation Method	Percentage < 4	Percentage ≥ 4
6 DOF	1.0938	98.9063
STK	1.3977	98.6023

Comparing the two half cone angles analyzed, the resulting percentages of less than four GPS satellites visible over the duration of the 2 days orbit given in Table II are within less than a percentage point of each other. The 6 DOF simulation for both cone angles closely resembles the STK simulation results. As a result, this confirms the GPS satellite orbit propagation method used for the 6 DOF simulation properly calculates the position of the GPS satellites given a set of GPS ephemerides.

G. Pseudorange Error Budget

The purpose of this section is to describe the methodology and process taken to validate the error sources affecting the calculated pseudoranges and approximate range rates. The expected total error in the pseudorange for a ground based GPS receiver is approximately 5-15 meters(1σ) [5],[27]. The main contribution to the pseudorange error is the ionosphere error. During months of high solar activity, the time delay due to the presence of the atmosphere increases, while the time delay will decrease during months of low solar activity. The position of the GPS receiver on the Earth affects the time delay since there is a higher total electron count (TEC) located equatorially about the Earth and low amounts of TEC around the poles [23].

Time delays due to the ionosphere and troposphere are both governed by physics

and restricts error alteration without some form of alternate position location. However, the spacecraft will almost exclusively be located outside the troposphere and will not experience a time delay due to signal passage through the troposphere. Any drift in the GPS satellite clocks will be experienced in the same manner regardless of the location of the GPS receiver.

Table III gives error data corresponding to the ground based GPS sensor [5] and the GPS receiver located on-board the orbiting spacecrafts assuming the coarse-acquisition (C/A) code is used. Note that each error source has units of meters. The total error values given in Table III are the RSS values calculated using all of the error sources corresponding to each sensor.

Table III. GPS Error Sources

Active Error Sources	Expected Error Reference [5], [27], [25], [9]	Chaser Sensor Error (Simulation)	Target Sensor Error
Ionosphere	2.0-15.0	6.9	7.2
Troposphere	0.0-1.0	0.0	0.0
Ephemeris	2.0-2.5	2.1	2.1
Receiver Noise	0.0-0.7	0.7	0.7
Satellite Clock	1.0-2.0	1.8	1.8
Multipath	0.0-1.0	0.5	2.0
Total Error (RMS)	3.0-15.4	7.3	8.7

The total RMS error does not include the range rate error since the range rate

error does not contribute to the pseudorange error. The expected range rate error is <0.2 meters per second and is determined to be 0.1 meters per second for both vehicles from simulation results. Also, the time delay due to the presence of the troposphere is non-existent for the trajectory considered. The RMS value for the total pseudorange error for the chaser vehicle is approximately seven meters one sigma. The RMS value for the total pseudorange error for the target vehicle is approximately nine meters one sigma. The difference between the two values is attributed to the steady state standard deviation of the multipath error for the target vehicle being four times greater than that of the chaser vehicle as well as a slight difference in the ionosphere error. As previously discussed, the multipath error of the target vehicle is modeled to be higher due to the complexity in the target vehicle's structure as opposed to the more simplistic chaser vehicle structure. Since the ionosphere time delay is associated with latitude location, the two vehicles being located at different latitudes results in a difference in the ionosphere error.

The following figures are the time history of the RMS values of each error for all 100 Monte Carlo simulations. The time history of the RMS values is determined using Equation 2.36 where N is the total number of recorded errors for one simulation. For each of the figures, errors for both vehicles are included allowing for a comparison between the errors experienced by each vehicle. The total error due to the troposphere is zero for the entire simulation and is therefore not included.

$$\epsilon_{\mathbf{err_{rms_j}}} = \sqrt{\frac{1}{100}\sum_{i=1}^{100}\epsilon_{err_i}^2} \quad \text{for } j = 1 \ldots N \tag{2.36}$$

Figure 5 shows the time history of the RMS values of the ionosphere error for all 100 Monte Carlo simulations. Although the initial Ω_0 and initial GPS time are varied for each Monte Carlo simulation, the rotation of the GPS constellation and receiver

positions in ECEF coordinates is about the z-axis of the ECI frame. Since only a single trajectory is considered, the latitude of both the constellation and receiver positions remain unchanged resulting in a similar error time history for each Monte Carlo simulation. In order to shift the cosine behavior of the error left or right, the latitudes of the receiver positions must change.

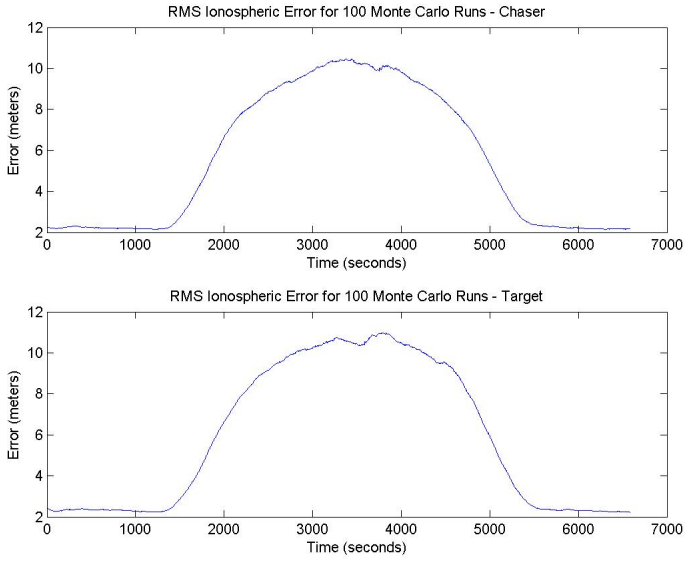

Fig. 5. RMS Ionosphere Error - 100 Monte Carlo Runs

Figure 6 gives the RMS values of the ephemeris errors for all 100 Monte Carlo simulations. The ephemeris error is modeled as a second order Gauss-Markov process modeling errors on both position and velocity components of the GPS satellites as opposed to errors on each ephemeris data component. Figure 6 shows the growing error as time progresses as is modeled by defining the initial and final process noise covariance matrices over a 12 hour period. During the error analysis, a single broadcast ephemeris data file is used since ephemeris data is valid for four hour periods.

If the ephemeris data is updated, the error will reset to the initial covariance value defined and a linear growth of the error attributed to the new ephemeris data will begin from the time of ephemeris data acquisition.

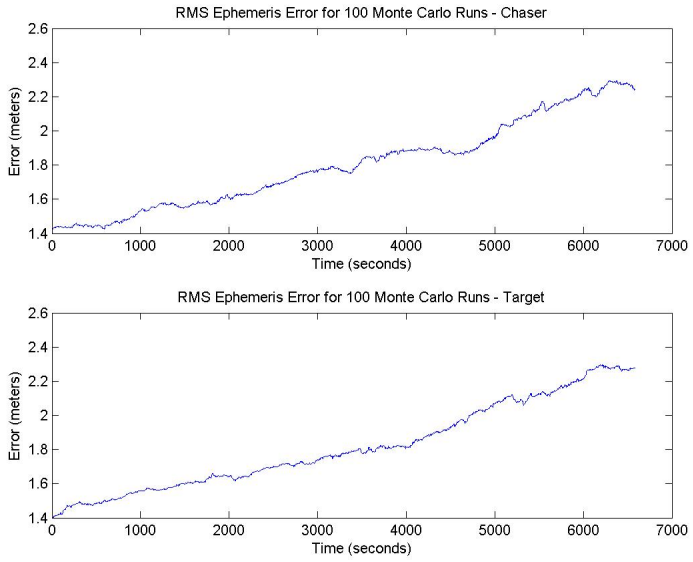

Fig. 6. RMS Ephemeris Error - 100 Monte Carlo Runs

Figure 7 gives the RMS values of the multipath error for both vehicles for all 100 Monte Carlo simulation. A first order Gauss-Markov process is used to model the error with steady state standard deviations of the chaser and target vehicles given as 0.5 meters and 2.0 meters respectively. Both plots in Figure 7 fluctuate about the steady state standard deviations defined.

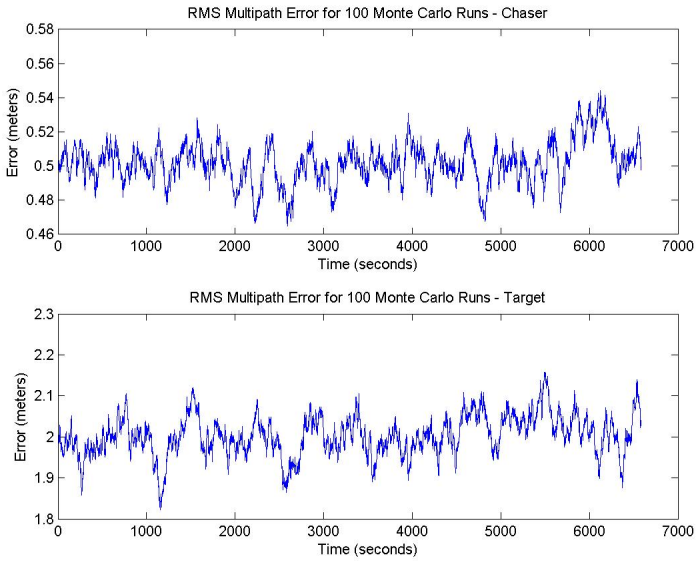

Fig. 7. RMS Multipath Error - 100 Monte Carlo Runs

Figures 8-9 give the RMS values for the error due to receiver noise and satellite clock error for all 100 Monte Carlo simulations. While both plots in each figure are very similar the plots are not identical due to different random numbers being used for each error source. Although both vehicles see many of the same satellites, especially as the relative distance between the two vehicles nears zero, each receiver will receive the GPS data at different times resulting in the differences in the plots in Figure 9. Since each receiver is independent from the other receiver, the receiver noise experienced by each receiver is unique to each respective receiver resulting in the difference in the plots in Figure 8.

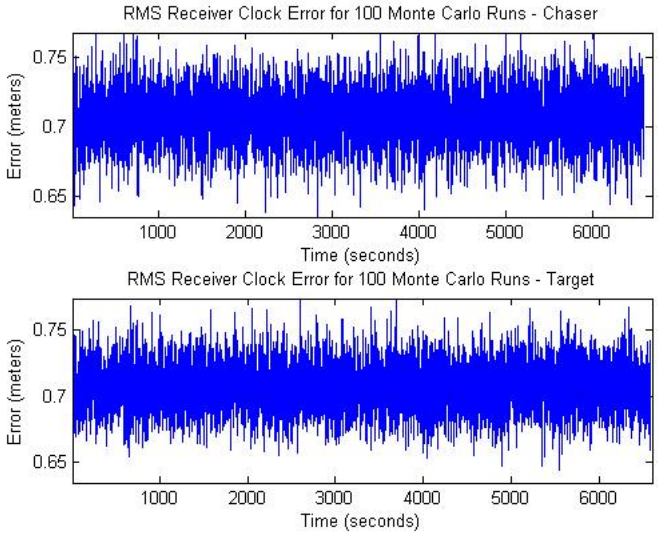

Fig. 8. RMS Error Due to Receiver Clock Noise - 100 Monte Carlo Runs

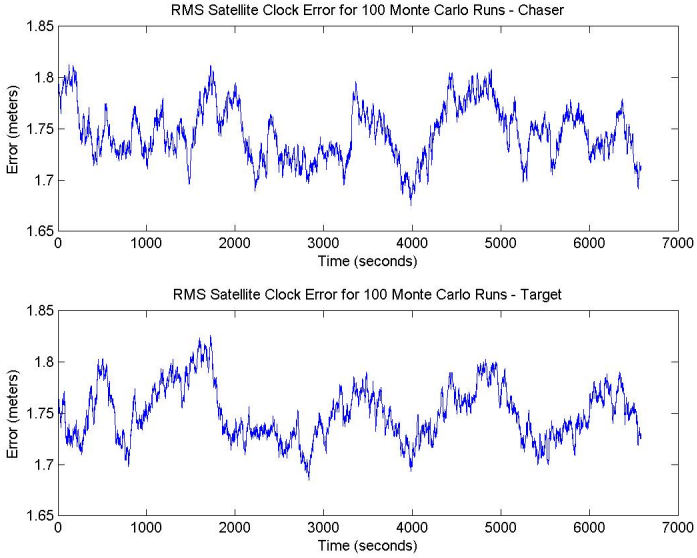

Fig. 9. RMS Satellite Clock Error - 100 Monte Carlo Runs

Figure 10 shows the total RMS value of the total pseudorange error for all 100 Monte Carlo simulations. It is obvious from Figure 10 that the ionosphere error

dominates the total error present in the pseudorange measurements which is to be expected considering the values given in Table III. Note that for each plot, the curve is shifted upwards by approximately the value of the multipath error of each vehicle. The upward shift is due to both ionosphere and multipath errors being calculated from time delays which are positive. All other errors, with the exception of the non-existent error due to the troposphere for the current trajectory, are not constrained to positive real numbers.

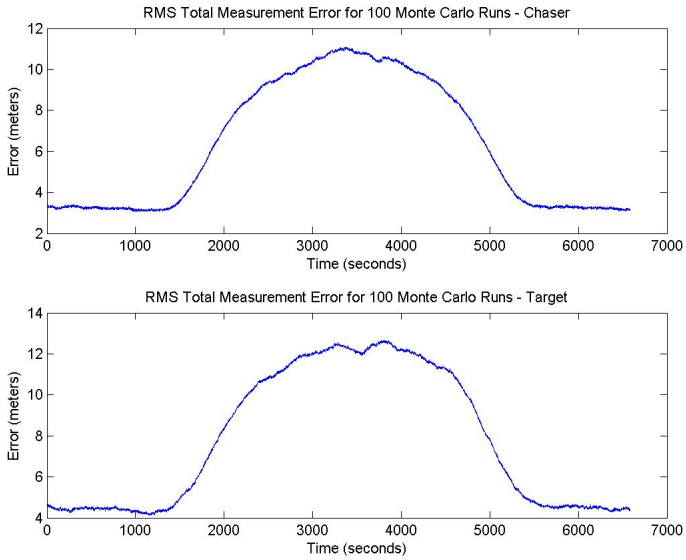

Fig. 10. RMS Total Pseudorange Error - 100 Monte Carlo Runs

Figure 11 is the RMS for corresponding to the range rate error for all 100 Monte Carlo simulations. The range rate error affects the velocity estimation and clock drift calculations as opposed to the pseudorange errors effect on the position estimation and clock bias calculations. Figure 11 shows the two combined first order Gauss-Markov processes assumed for the range rate error produce an error of 0.1 meters per

second.

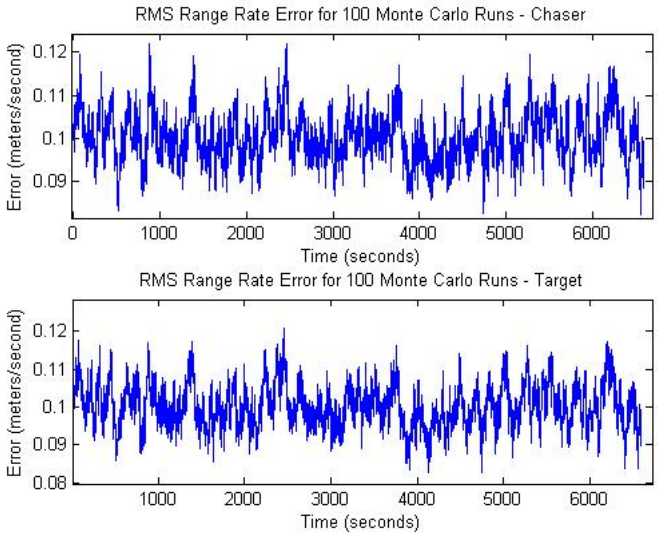

Fig. 11. RMS Range Rate Error - 100 Monte Carlo Runs

CHAPTER III

ADDITIONAL SENSOR MODELS

Details on the development of the mathematical models for a star tracker, gyroscope, and accelerometer are presented in this chapter. The star tracker provides attitude measurements. The gyroscopes and accelerometers provide the change in attitude angle and change in translational velocity respectively. The changes in attitude and velocity are used to compute the angular velocity and translational acceleration of the spacecraft by implementation of the mean value theorem.

A. Star Tracker

1. Principle of Operation

The star tracker takes advantage of technologically advanced imaging sensors to measure the relative orientation of the vehicle it is located on by tracking stars. The sensor detects the location of the stars in a two dimensional plane. With the location of the stars and the focal length associated with the sensor, the star tracker is able to determine the stars in the two dimensional image from an almanac. Once the stars are identified, the information acquired from almanac allows the star tracker to determine its orientation with respect to an inertial coordinate system.

2. Mathematical Model

The mathematical model used to describe the star tracker is given by Equation 3.1 [33].

$$\bar{\mathbf{q}}_i^{st} = \left(\left(\bar{\mathbf{q}}_b^{st} \otimes \bar{\mathbf{q}}_{error}\right) \otimes \bar{\mathbf{q}}_i^b\right) \otimes \bar{\mathbf{q}}_\eta \tag{3.1}$$

where

$\bar{\mathbf{q}}_i^{st}$: inertial to star tracker quaternion

$\bar{\mathbf{q}}_b^{st}$: body to star tracker quaternion

$\bar{\mathbf{q}}_{error}$: quaternion derived from alignment error

$\bar{\mathbf{q}}_i^b$: inertial to body quaternion

$\bar{\mathbf{q}}_\eta$: quaternion derived from tracker noise and bias, random walk

The scalar first definition of the quaternion is used. Let $\bar{\mathbf{a}}$ and $\bar{\mathbf{b}}$ be defined as:

$$\bar{\mathbf{a}} = \begin{bmatrix} \alpha \\ \boldsymbol{\xi}_{3\text{x}1} \end{bmatrix} \qquad \bar{\mathbf{b}} = \begin{bmatrix} \beta \\ \boldsymbol{\gamma}_{3\text{x}1} \end{bmatrix}$$

Using the above definition of $\bar{\mathbf{a}}$ and $\bar{\mathbf{b}}$, the following equation defines the quaternion product as seen in Equation 3.1 [34].

$$\bar{\mathbf{c}} = \bar{\mathbf{a}} \otimes \bar{\mathbf{b}} = \begin{bmatrix} 2\,\alpha\,\beta - \boldsymbol{\xi} \cdot \boldsymbol{\gamma} \\ \alpha\,\boldsymbol{\gamma} + \beta\,\boldsymbol{\xi} - \boldsymbol{\xi} \times \boldsymbol{\gamma} \end{bmatrix}$$

The star tracker returns an attitude parameter set that allows the user to know its current orientation relative to a fixed inertial frame. The derivation of Euler angles from quaternions is given by Equations 3.2-3.4 [34]. The estimated orientation of the chaser vehicle is defined in terms of Euler angles as opposed to quaternions.

$$\psi = \arctan\left(\frac{2q_1q_2 + 2q_0q_3}{2q_0^2 + 2q_1^2 - 1}\right) \tag{3.2}$$

$$\theta = \arcsin\left(2q_0q_2 - 2q_1q_3\right) \tag{3.3}$$

$$\phi = \arctan\left(\frac{2q_2q_3 + 2q_0q_1}{2q_0^2 + 2q_3^2 - 1}\right) \tag{3.4}$$

where

$$\bar{\mathbf{q}} = \begin{bmatrix} q_0 & q_1 & q_2 & q_3 \end{bmatrix}^T \tag{3.5}$$

3. Performance

The errors present in the star tracker model is given in Table IV [33].

Table IV. Star Tracker Model Error Parameters

Parameters	Values	Notes
Misalignment Error, $\bar{\mathbf{q}}_{error}$		
σ_{error}	0.1°	1σ standard deviation
Attitude Noise, $\bar{\mathbf{q}}_{\eta}$		
σ_{η_ϕ}	0.0002 rad	1σ standard deviation, roll
σ_{η_θ}	0.0002 rad	1σ standard deviation, pitch
σ_{η_ψ}	0.0002 rad	1σ standard deviation, yaw
m_η	0.1 °	mean for all attitude states

B. Gyroscopes

1. Principle of Operation

The rate gyroscopes on-board the spacecraft measure the angular velocity of the vehicle and integrate the measured value to determine the change in angle measured by the gyroscope. Three-axis gyroscopes are used.

2. Mathematical Model

The mathematical model used to describe the rate gyroscopes mounted on-board the spacecraft is given by Equation 3.6 [35].

$$\boldsymbol{\Delta\theta}^b = \int_t^{t+\Delta t} \left\{ \boldsymbol{\omega}^b + \boldsymbol{\eta}_v + \mathbf{w}_{m_v} \right\} d\tau \tag{3.6}$$

$$\boldsymbol{\omega}^b = [\mathbf{T}_i^b(\bar{\mathbf{q}}_i^b)]\, \boldsymbol{\omega}^i \tag{3.7}$$

where

$\boldsymbol{\theta}^b$	:	angle vector given in body coordinate system
$\boldsymbol{\omega}^b$	:	angular velocity vector in body coordinate system
$\mathbf{T}_\mathbf{i}^\mathbf{b}$	:	transformation matrix from inertial to body coordinate system
$\boldsymbol{\eta}_v$	:	noise and bias vector associated with angular velocity, random walk
$\mathbf{w}_{m_v}$	:	first-order Markov process vector associated with angular velocity

The sample time, Δt, is 0.1 seconds. The resulting angular measurement is given in the body coordinate system and is used to describe the motion and orientation of the spacecraft.

3. Performance

Table V gives the error parameters present on the gyroscopes of the IMU [36], [37].

Table V. Gyroscope Model Error Parameters

Parameters	Values	Notes
IMU Body Misalignment Error		
$\sigma_{IMU_{mis}}$	0.05 °	1σ standard deviation
Markov error, $\mathbf{w}_{m_v}$		
σ_{m_v}	$\frac{0.3°}{hr}$	1σ standard deviation
τ_{m_v}	3600 sec	time constant
Gyroscope Noise, $\boldsymbol{\eta}_v$		
σ_{η_v}	$\frac{0.025°}{\sqrt{hr}}$	1σ standard deviation
m_{η_v}	$\frac{0.5°}{hr}$	error mean

C. Accelerometer

1. Principle of Operation

The mathematical model used to represent the accelerometer and the performance specifications of the accelerometers used onboard the spacecraft is documented in this section. The accelerometer located on-board the spacecraft measures the change in the translational velocity. The maneuvers applied during the rendezvous operation are recorded by the accelerometer.

2. Mathematical Model

The mathematical model used to describe the accelerometer mounted on-board the spacecraft is given by Equation 3.8 [35].

$$\boldsymbol{\Delta}\mathbf{v}_{imu} = \int_{t}^{t+\Delta t} \{\mathbf{a}_{imu} + \boldsymbol{\eta}_a + \mathbf{w}_{m_a}\}\, d\tau \tag{3.8}$$

where

$\mathbf{a}_{imu}$: translational acceleration vector in IMU coordinate system

$\boldsymbol{\Delta}\mathbf{v}_{imu}$: velocity vector in IMU coordinate system

$\boldsymbol{\eta}_a$: noise and bias vector associated with acceleration, random walk

$\mathbf{w}_{m_a}$: first-order Markov process vector associated with acceleration

The sample time, Δt, is 0.1 seconds. The vector $\boldsymbol{a}_{imu}$ is the translational acceleration as defined in the IMU coordinate system. All values entering into the IMU sensor are given in a body frame therefore transformations are performed on incoming parameters to redefine the parameters in the IMU coordinate system. Equation 3.12 transforms position and velocity (both translational and rotational) vectors into the IMU coordinate systems from the body coordinate system [34].

$$\bar{\mathbf{q}}_{imu}^{body} = [q_0 \;\; q_1 \;\; q_2 \;\; q_3]^T = [q_0 \;\; \mathbf{q}] \tag{3.9}$$

$$\mathbf{x}_{body} = [x_1 \;\; x_2 \;\; x_3]^T \tag{3.10}$$

$$\boldsymbol{\omega} = \mathbf{q} \times \mathbf{x}_{body} \tag{3.11}$$

$$\mathbf{x}_{imu} = \mathbf{x}_{body} - 2\left(q_0\boldsymbol{\omega} + \mathbf{q} \times \boldsymbol{\omega}\right) \tag{3.12}$$

Euler parameters given in the body coordinate system are transformed to the IMU coordinate system. The sensor accepts the angular velocity, angular velocity rate, Euler parameter set from inertial frame to IMU frame, acceleration due to non-gravitational forces and IMU location onboard the spacecraft with respect to the CG location of the spacecraft. Using these parameters, the translational acceleration $\mathbf{a}_{imu}$

as shown in Equation 3.8 is calculated by summing the acceleration due the offset of the IMU from the CG of the spacecraft with the acceleration due to non-gravitational forces.

3. Performance

The error parameters present in the accelerometer of the IMU model are given in Table VI. The values given in Table VI are typical values for accelerometers used for space applications [38]. The bias value given in reference [38] is a start up bias and is assumed to be compensated internally by the IMU. The bias present on the measurements of the accelerometer is in the form of the one-year composite repeatability. This value is used to model the mean and standard deviation of the bias affecting the accelerometer measurements.

Table VI. Accelerometer Model Error Parameters

Parameters	Values	Notes
IMU Body Misalignment Error		
$\sigma_{IMU_{mis}}$	0.05 °	1σ standard deviation
Markov error, $\mathbf{w}_{m_a}$		
σ_{m_a}	7 μg	1σ standard deviation
τ_{m_a}	3600 sec	time constant
Accelerometer Noise, $\boldsymbol{\eta}_a$		
σ_{η_a}	40 μg	1σ standard deviation
m_{η_a}	40 μg	error mean

CHAPTER IV

GPS SATELLITE VISIBILITY

The number of satellites a GPS receiver can receive data transmissions from is limited by the field of view of the antenna. In addition to field of view limitations, there may also be objects in the line of sight of the receiver to a satellite that interfere with the signals being transmitted by the satellite. Any obstruction in the antenna field of view results in signal loss from satellites obscured by the obstruction.

Half cone angles of 55, 65, and 75 degrees are analyzed to determine the number of satellites in view over the course of the proximity operations. Both chaser and target vehicles are analyzed. The target vehicle is the ISS for this analysis. The same half cone angles are investigated while propagating a single orbit of a vehicle at the ISS altitude at various longitudes of the ascending node. For the cases under examination in this thesis, the antenna located onboard the chaser vehicle is oriented in the zenith direction while the ISS antenna is oriented a -15 degree pitch from zenith as defined in the LVLH reference frame. Two configurations of the GPS satellite constellation are examined, with 24 and 32 active satellites. There are six different GPS satellite orbits with at least four satellites active on each orbit at any given time. Currently there are 32 satellites in orbit that are capable of being active at one time therefore the case when all satellites are active is examined. In order to select which 24 of the 32 satellites should be used to allow for greatest constellation coverage, the right ascension of each GPS satellite is examined to determine which satellites are on each of the six previously mentioned orbits. With the orbits of each satellite determined, the satellites are chosen based on the four largest differences in the argument of perigee of each satellite. Although the sum of the argument of perigee and mean anomaly should be used for satellite selection, it is assumed the

mean anomaly of each satellite is zero therefore leaving the argument of perigee on which to base the satellite selection. With this determined, the analysis is performed with time durations for certain numbers of visible satellites recorded and analyzed.

A. Proximity Operations

The duration of the rendezvous is assumed to be 13000 seconds, although GPS navigation is only used during approximately 6600 seconds of the rendezvous, for the chaser vehicle located 23 kilometers to 500 meters downrange of the ISS. The following analysis is performed up to the chaser vehicle being 500 meters downrange during which GPS navigation is used. Although GPS navigation is only used for 6600 seconds, a total of 9000 seconds are examined to allow for a larger sample space. The number of satellites visible is influenced solely by the antenna field of view. For the rendezvous, the antenna field of view of the chaser vehicle may encounter an area of obstruction due to the presence of the ISS as a result of the location of the receiver onboard the chaser vehicle. The obstruction area within the field of view will continuously grow as the chaser vehicle nears the ISS until the entire field of view of the antenna is obstructed by the ISS. By the time the GPS antenna is rendered useless due to the obstruction, navigation of the chaser vehicle will have switched from GPS based navigation to another navigation method which has a higher fidelity at close proximity than GPS navigation. The probability that the ISS will experience an obstructed view due to the chaser vehicle is low, since the antenna onboard the ISS will be directed away from the approaching chaser vehicle. The chance of either vehicle experiencing an obstructed view due to the presence of satellites at higher altitudes is minuscule and therefore neglected from the analysis.

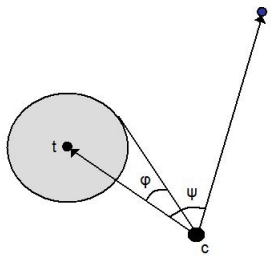

Fig. 12. Antenna Field of View Obstruction

Figure 12 gives a two-dimensional view of the manner in which satellite visibility is determined when an object obstructs the field of view of the GPS antenna. The gray circle represents the ISS with a diameter of 100 meters with the center of the circle located at the center of gravity of the ISS. It should be noted that the current maximum length of the ISS is approximately 100 meters hence the reason for choosing the dimensions of the sphere. For any angle $\Psi > \Phi$, the direct signal path between the GPS satellite and vehicle is not blocked; therefore, the satellite remains in view of the vehicle. On the contrary, any angle $\Psi \leq \Phi$ results in an interference of the direct signal path due to the obstruction. Therefore, the satellite is not seen by the GPS receiver located onboard the chaser vehicle, although it may be seen by the receiver onboard the ISS.

The ISS does not obstruct the view of the chaser GPS receiver until the chaser vehicle is less than 500 meters downrange of the ISS. As aforementioned, a relative navigation method will be used from the time at which the chaser vehicle is approximately 1300 meters downrange of the ISS until rendezvous with the ISS. Although a relative navigation method will be used beginning when the chaser vehicle is approximately 1300 meters downrange, GPS navigation will remain active until the chaser is approximately 500 meters downrange at which point the chaser vehicle will be

navigated solely by the relative navigation method.

The following analysis is performed by repeating the rendezvous trajectory 12 times, each starting with the GPS constellation rotated one hour forward since the orbital period of the GPS constellation is 12 hours. The number of satellites visible to both the chaser spacecraft and ISS is analyzed in addition to common satellites seen by both vehicles. Statistical information corresponding to the amount of time various numbers of satellites are visible are calculated to better understand the visibility of the GPS constellation over the duration of the rendezvous during which GPS navigation is implemented. In addition, the percentage of satellites visible over the course of the rendezvous is presented.

1. 55 Degree Half Cone Angle

Figures 13 shows the percentage of satellites visible over the duration of the rendezvous with a 24 GPS satellite constellation configuration for the ISS oriented at the 0-0-0 LVLH attitude. Figures 14 gives the percentage of visible satellites during the course of the rendezvous when GPS navigation is implemented assuming a 32 active GPS satellites constellation for the ISS positioned in the 0-0-0 LVLH attitude. The number of satellites defined does not correspond to occurrences during which the number of satellites is exactly the number specified but instead refers to the circumstances during which the number of satellites visible is equal to or greater than the number specified. For example, the percentage given for 6 satellites visible corresponds to the the total number of occasions during the course of the rendezvous in which 1-6 satellites are in view of the receiver. As can be inferred from Figure 13, the maximum number of satellites visible over the entire duration of rendezvous for a 24 GPS satellite constellation configuration does not exceed 6 satellites for either vehicle or 5 commonly shared satellites of both vehicles. Comparing Figures 13 and 14 veri-

fies that more satellites active in the GPS constellation results in higher percentages of satellites visible for all amounts of GPS satellites shown in the figures.

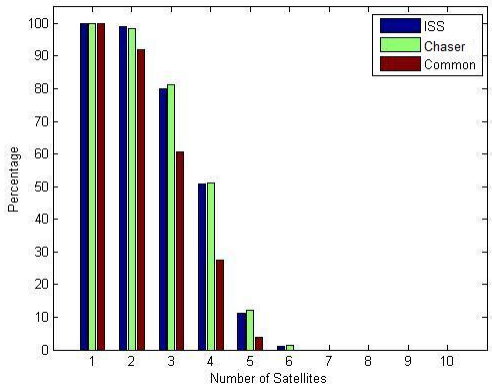

Fig. 13. Percentage of Occurrences When at Least the Number of Satellites Given Are Visible - ISS at 0-0-0 LVLH Attitude, 24 GPS Satellites, 55° Half Cone Angle

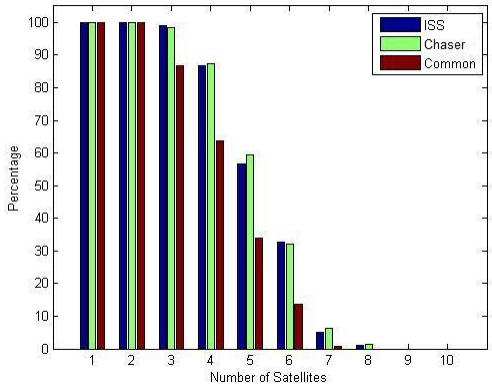

Fig. 14. Percentage of Occurrences When at Least the Number of Satellites Given Are in View - ISS at 0-0-0 LVLH Attitude, 32 GPS Satellites, 55° Half Cone Angle

Table VII gives statistical information of the time interval quantities corresponding to the cases when strictly less than the number of satellites are visible over the duration of the rendezvous. In order to determine an estimated position and velocity

from GPS measurements, information from at least four GPS satellites is needed. Information from five GPS satellites is required to detect faulty pseudorange measurements and six or more GPS satellites are needed to correctly identify and detect the faulty pseudorange measurements.

Table VIII accounts for the statistical data corresponding to the time interval quantities during which at least the number of satellites are visible. Notice in both Table VII and Table VIII there are standard deviation values higher than the average value of the time intervals although the value for all time intervals is greater than zero. The large standard deviation is a result of one or two outlying data points that dominate the calculation of the standard deviation and raise the value above that of the given average. Due to the large standard deviations that are seen occasionally in Tables VII-VIII, minimum and maximum time intervals are given as well as the median value of the time interval quantities.

Table VII. Statistics of Time Interval Data for Instances When Strictly Less than the Given Number of Satellites Are Visible - ISS at 0-0-0 LVLH Attitude, 55° Half Cone Angle

Vehicle	Statistical Variables	24 Satellites			32 Satellites		
		< 4	< 5	< 6	< 4	< 5	< 6
ISS	# of Entries	122.0	80.0	21.0	113.0	152.0	84.0
	Max (s)	1851.0	6308.0	9000.0	994.0	3119.0	7960.0
	Min (s)	3.0	5.0	303.0	2.0	3.0	3.0
	Median (s)	328.5	531.5	4662.0	144.0	258.5	615.0
	Average (s)	486.0	1177.4	5085.0	192.2	394.4	1082.2
	Std Dev (s)	457.0	1371.1	3361.5	184.5	428.3	1448.7
Chaser	# of Entries	134.0	75.0	20.0	123.0	155.0	79.0
	Max (s)	1853.0	6539.0	9000.0	1005.0	3165.0	8022.0
	Min (s)	2.0	5.0	361.0	2.0	3.0	10.0
	Median (s)	283.0	582.0	5565.5	139.0	273.0	565.0
	Average (s)	462.2	1271.0	5351.9	199.3	404.5	1161.0
	Std Dev (s)	470.0	1457.0	3342.6	189.9	448.9	1509.7
Common	# of Entries	103.0	40.0	14.0	158.0	96.0	43.0
	Max (s)	4349.0	9000.0	9000.0	2012.0	5770.0	9000.0
	Min (s)	2.0	47.0	3187.0	2.0	10.0	9.0
	Median (s)	487.0	1468.5	9000.0	239.5	559.0	1725.0
	Average (s)	817.5	2601.4	7700.9	333.7	896.8	2363.7
	Std Dev (s)	849.5	2637.9	2200.8	326.2	987.1	2434.8

Table VIII. Statistics of Time Interval Data for Instances When at Least the Given Number of Satellites Are Visible - ISS at 0-0-0 LVLH Attitude, 55° Half Cone Angle

Vehicle	Statistical Variables	24 Satellites			32 Satellites		
		≥ 4	≥ 5	≥ 6	≥ 4	≥ 5	≥ 6
ISS	# of Entries	121.0	70.0	9.0	118.0	152.0	74.0
	Max (s)	1496.0	685.0	324.0	2928.0	1580.0	1265.0
	Min (s)	11.0	2.0	15.0	4.0	1.0	2.0
	Median (s)	280.0	141.5	125.0	527.0	212.0	165.5
	Average (s)	402.7	197.4	136.3	731.3	316.2	231.2
	Std Dev (s)	364.5	180.1	102.7	683.8	321.5	266.7
Chaser	# of Entries	128.0	65.0	8.0	128.0	150.0	70.0
	Max (s)	1392.0	638.0	348.0	2939.0	1361.0	1208.0
	Min (s)	8.0	2.0	9.0	4.0	2.0	6.0
	Median (s)	256.5	146.0	112.0	477.5	203.0	161.5
	Average (s)	360.0	195.2	121.6	652.3	302.1	232.8
	Std Dev (s)	336.8	176.8	109.0	643.1	305.5	263.7
Common	# of Entries	94.0	28.0	2.0	154.0	87.0	32.0
	Max (s)	1144.0	311.0	128.0	1438.0	1125.0	985.0
	Min (s)	1.0	9.0	60.0	1.0	7.0	1.0
	Median (s)	198.5	104.5	94.0	268.5	191.0	94.5
	Average (s)	253.2	140.8	94.0	358.9	251.8	198.8
	Std Dev (s)	228.2	100.1	48.1	322.2	259.4	227.0

2. 65 Degree Half Cone Angle

Figures 15-16 depict the percentage of satellites visible over the duration of the rendezvous when GPS navigation is used for 24 and 32 active GPS satellites configuration for the ISS oriented at an attitude of 0-0-0 LVLH. For the 65 degree half cone angle under consideration, the maximum number of satellites seen over the entire time period does not exceed 8 satellites for all cases assuming 24 active GPS satellites and 10 satellites for both vehicles with 32 active GPS satellites.

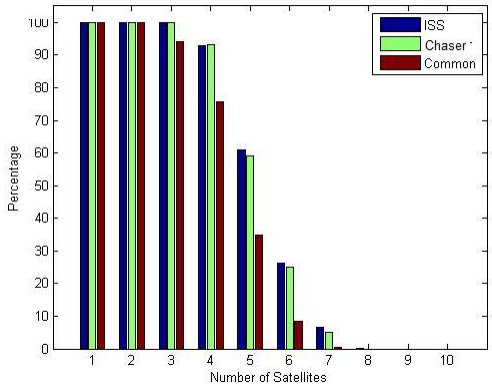

Fig. 15. Percentage of Occurrences When at Least the Number of Satellites Given Are in View - ISS at 0-0-0 LVLH Attitude, 24 GPS Satellites, 65° Half Cone Angle

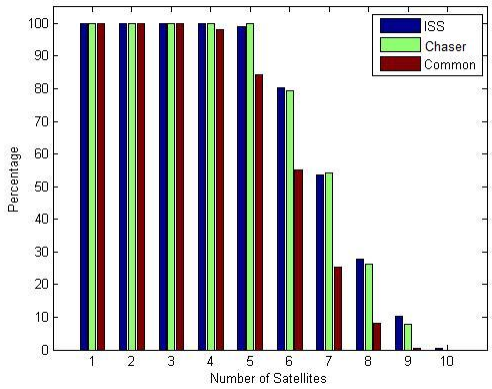

Fig. 16. Percentage of Occurrences When at Least the Number of Satellites Given Are in View - ISS at 0-0-0 LVLH Attitude, 32 GPS Satellites, 65° Half Cone Angle

Table IX gives statistical information of the time intervals corresponding to occasions during which the number of GPS satellites visible is less than the number of given satellites over the duration of the rendezvous. As additional satellites signals are received or lost, the time interval corresponding to the new number of visible satellites resets and time accumulates until more satellites signals are received or lost at which time the current time interval is recorded for the previous number of satellites in view.

Table IX. Statistics of Time Interval Data for Instances When Strictly Less than the Given Number of Satellites Are Visible - ISS at 0-0-0 LVLH Attitude, 65° Half Cone Angle

Vehicle	Statistical Variables	24 Satellites			32 Satellites		
		< 4	< 5	< 6	< 4	< 5	< 6
ISS	# of Entries	74.0	133.0	98.0	7.0	59.0	157.0
	Max (s)	791.0	1935.0	4201.0	552.0	663.0	1036.0
	Min (s)	6.0	2.0	4.0	19.0	5.0	2.0
	Median (s)	151.5	282.0	541.5	110.0	114.0	184.0
	Average (s)	207.0	403.0	908.4	189.7	154.3	252.2
	Std Dev (s)	206.1	406.7	999.4	214.4	144.7	218.4
Chaser	# of Entries	82.0	141.0	91.0	10.0	70.0	166.0
	Max (s)	775.0	1913.0	3986.0	559.0	646.0	1141.0
	Min (s)	5.0	2.0	1.0	11.0	3.0	1.0
	Median (s)	135.0	273.0	553.0	99.0	79.5	161.5
	Average (s)	213.2	396.3	989.8	153.0	144.0	253.0
	Std Dev (s)	209.4	415.6	1080.5	188.4	152.8	241.3
Common	# of Entries	127.0	107.0	48.0	74.0	151.0	131.0
	Max (s)	1579.0	3769.0	9000.0	870.0	1314.0	3139.0
	Min (s)	3.0	4.0	6.0	2.0	1.0	5.0
	Median (s)	172.0	413.0	1493.5	90.0	146.0	270.0
	Average (s)	310.0	744.4	2144.8	127.7	225.2	557.8
	Std Dev (s)	344.8	837.7	2161.8	142.9	236.7	646.4

Table X accounts for the statistical information corresponding to the time inter-

vals during which at least the given number of satellites in view.

Table X. Statistics of Time Interval Data for Instances When at Least the Given Number of Satellites Are Visible - ISS at 0-0-0 LVLH Attitude, 65° Half Cone Angle

Vehicle	Statistical Variables	24 Satellites			32 Satellites		
		≥ 4	≥ 5	≥ 6	≥ 4	≥ 5	≥ 6
ISS	# of Entries	84.0	132.0	90.0	19.0	68.0	161.0
	Max (s)	4545.0	2322.0	1459.0	9000.0	8905.0	2759.0
	Min (s)	1.0	2.0	3.0	288.0	1.0	1.0
	Median (s)	671.0	243.0	193.5	5957.0	836.5	203.0
	Average (s)	1103.5	412.3	211.0	5614.9	1454.5	425.0
	Std Dev (s)	1120.2	450.8	248.8	3215.9	1904.3	536.4
Chaser	# of Entries	90.0	141.0	82.0	22.0	79.0	166.0
	Max (s)	4426.0	2246.0	1084.0	9000.0	9000.0	3004.0
	Min (s)	2.0	1.0	4.0	48.0	1.0	1.0
	Median (s)	604.0	188.0	139.0	4347.5	627.0	178.5
	Average (s)	1005.9	369.8	218.8	4840.1	1239.6	397.6
	Std Dev (s)	1092.8	445.8	212.6	3118.4	1589.0	522.6
Common	# of Entries	128.0	100.0	37.0	81.0	152.0	125.0
	Max (s)	2076.0	1416.0	462.0	5411.0	2677.0	1394.0
	Min (s)	1.0	1.0	2.0	1.0	1.0	1.0
	Median (s)	371.5	183.0	79.0	887.0	307.5	203.0
	Average (s)	536.2	283.5	136.4	1216.7	486.8	279.4
	Std Dev (s)	517.5	288.9	131.8	1243.5	517.5	282.5

3. 75 Degree Half Cone Angle

Figures 17 - 18 show the percentage of satellites visible over time for the ISS oriented at 0-0-0 LVLH with a 24 and 32 active GPS satellites constellation configuration respectively when GPS navigation is implemented during the rendezvous. For both GPS constellation configurations, Figures 17 - 18 reveal that the maximum number of satellites seen over the entire rendezvous exceeds 10 satellites but more importantly, the minimum number of satellites seen for all three categories is greater than 4 except for approximately 3% of the duration of the rendezvous. Recall from the previous chapter that at least four GPS satellites must be in view in order to approximate the position of the receiver using absolute navigation. Since at least four are in view for both vehicles, absolute navigation can be performed over the duration of the rendezvous without measurement rejection due to the a lack of satellites. At the same time, this does not suggest that measurements will always be accepted since poor geometry can lead to a poor quality of measurements.

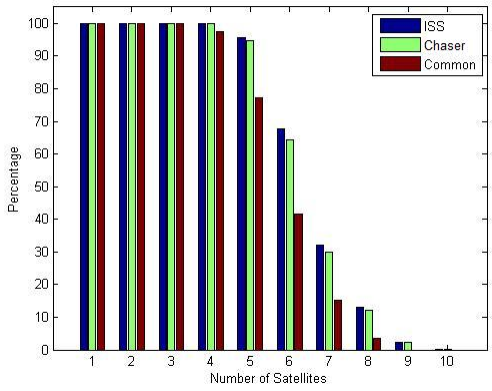

Fig. 17. Percentage of Occurrences When at Least the Number of Satellites Given Are in View - ISS at 0-0-0 LVLH Attitude, 24 GPS Satellites, 75° Half Cone Angle

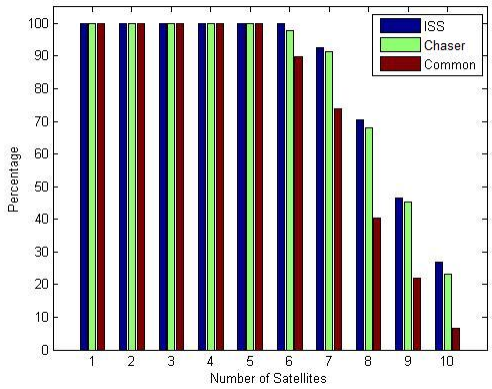

Fig. 18. Percentage of Occurrences When at Least the Number of Satellites Given Are in View - ISS at 0-0-0 LVLH Attitude, 32 GPS Satellites, 75° Half Cone Angle

Table XI presents the data related to a statistical analysis of time interval quantities corresponding to cases when strictly less than the number of satellites mentioned are in view over the time in which GPS navigation is used throughout the course of the rendezvous.

Table XII gives the statistical information of the time interval quantities corresponding to occurrences during which at least the number of satellites are in view over the time period during which navigation with respect to position and velocity is done solely using GPS measurements. Navigation with respect to orientation is performed with the help of a star tracker. Table XI communicates that for more than 90% of the duration of the rendezvous, at least six satellites are visible to each vehicle for a GPS constellation of 32 active satellites and five satellites for a 24 active GPS satellites configuration.

Table XI. Statistics of Time Interval Data for Instances When Strictly Less than the Given Number of Satellites Are Visible - ISS at 0-0-0 LVLH Attitude, 75° Half Cone Angle

Vehicle	Statistical Variables	24 Satellites			32 Satellites		
		< 4	< 5	< 6	< 4	< 5	< 6
ISS	# of Entries	8.0	57.0	129.0	0.0	4.0	15.0
	Max (s)	238.0	396.0	1730.0	0.0	202.0	246.0
	Min (s)	9.0	2.0	3.0	0.0	9.0	2.0
	Median (s)	88.5	73.0	215.0	0.0	92.0	110.0
	Average (s)	92.1	125.6	293.4	0.0	98.8	115.8
	Std Dev (s)	68.4	109.0	301.8	0.0	81.0	77.6
Chaser	# of Entries	10.0	67.0	130.0	1.0	3.0	22.0
	Max (s)	261.0	469.0	1724.0	7.0	236.0	261.0
	Min (s)	12.0	1.0	2.0	7.0	138.0	4.0
	Median (s)	59.5	107.0	199.5	7.0	168.0	80.5
	Average (s)	103.3	142.2	317.0	7.0	180.7	108.4
	Std Dev (s)	84.0	122.3	342.2	0.0	50.2	88.5
Common	# of Entries	33.0	122.0	135.0	2.0	13.0	94.0
	Max (s)	457.0	755.0	2356.0	132.0	437.0	483.0
	Min (s)	6.0	1.0	7.0	17.0	6.0	2.0
	Median (s)	106.0	164.5	334.0	74.5	50.0	102.0
	Average (s)	153.3	237.9	516.9	74.5	121.5	149.0
	Std Dev (s)	127.8	200.6	535.2	81.3	152.6	128.6

Table XII. Statistics of Time Interval Data for Instances When at Least the Given Number of Satellites Are Visible - ISS at 0-0-0 LVLH Attitude, 75° Half Cone Angle

Vehicle	Statistical Variables	24 Satellites			32 Satellites		
		≥ 4	≥ 5	≥ 6	≥ 4	≥ 5	≥ 6
ISS	# of Entries	20.0	67.0	130.0	12.0	16.0	26.0
	Max (s)	9000.0	4224.0	2986.0	9000.0	9000.0	9000.0
	Min (s)	43.0	9.0	3.0	9000.0	43.0	415.0
	Median (s)	6526.0	932.0	323.5	9000.0	9000.0	3306.0
	Average (s)	5363.8	1505.2	539.7	9000.0	6726.1	4087.5
	Std Dev (s)	3475.1	1332.8	614.9	0.0	3227.5	2558.9
Chaser	# of Entries	22.0	78.0	135.0	13.0	15.0	34.0
	Max (s)	9000.0	4125.0	2767.0	9000.0	9000.0	9000.0
	Min (s)	191.0	21.0	3.0	1156.0	1126.0	161.0
	Median (s)	4781.5	679.0	300.0	9000.0	9000.0	2822.5
	Average (s)	4862.7	1262.6	494.8	8308.1	7164.7	3106.7
	Std Dev (s)	3295.4	1262.6	554.2	2172.8	2770.2	2214.6
Common	# of Entries	45.0	127.0	132.0	14.0	25.0	103.0
	Max (s)	6330.0	2971.0	1700.0	9000.0	9000.0	5656.0
	Min (s)	20.0	2.0	3.0	448.0	28.0	2.0
	Median (s)	2151.0	302.0	169.0	9000.0	3568.0	483.0
	Average (s)	2287.6	621.9	289.5	7703.6	4256.8	912.5
	Std Dev (s)	1766.4	727.5	325.5	2970.3	3208.4	1026.8

For this particular case, all standard deviations with a value of zero in Table XI

correspond to a zero value time interval while zero standard deviations in Table XII correspond to a single time interval value. Although for Table XI there are at least five visible satellites at all times for all three categories, the manner in which data is recorded allows for the time interval to be zero due to there always being more than the number of satellites specified for the zero quantity entries. There are also cases present where there are zero quantities for one or both vehicles but a value for the commonly shared satellites case and vice versa. This is attributed to the position difference between the target and pursuing chaser vehicle resulting in different satellites viewed by each vehicle. Although each vehicle may see two or more satellites, this does not mean that the overlapping field of view of these satellites contains as many satellites as seen by each individual vehicle satellites.

The visibility analysis suggests that uses of 55° and 65° fields of view could affect relative navigation. There are time intervals of 1005 seconds for a 55° field of view and 559 seconds for a 65° field of view when there are less than 4 satellites visible to each vehicle. The time intervals corresponding to occurrences when less than 4 common satellites are visible is worse at 2012 and 870 seconds for 55° and 65° fields of view respectively. The maximum time interval corresponding to less than 4 satellites visible for a 75° receiver field of view is 7 seconds for the chaser vehicle and 132 seconds for common satellite visibility. Since the maximum time interval of less than 4 satellites visible is substantially lower for 75° field of view compared to 55° and 65° fields of view, a field of view of 75° is used during the analysis of the four Kalman filters.

CHAPTER V

KALMAN FILTER DEVELOPMENT

The development of the various Kalman filter architectures is presented in this chapter. The theory behind the extended Kalman filter (EKF) is also outlined. The four Kalman filters developed are 1) position-velocity EKF, 2) relative pseudorange EKF, 3) pseudorange EKF and 4) reduced pseudorange EKF. The four filters estimate the position and velocity of both the chaser and target vehicles as well as the attitude of the chaser vehicle. In addition to the states of each vehicle, additional states estimated vary with each filter. Each filter processes different GPS measurements except for the pseudorange and reduced pseudorange filters.

A. Extended Kalman Filter

The purpose of this section is to develop the equations and methodology of the EKF. The EKF utilizes a discrete update logic with a continuous time propagation of the system dynamics. The model for the states and measurements corrupted by noise is given by Equations 5.1-5.2.

$$\dot{\mathbf{x}}(t) = \mathbf{f}(\mathbf{x}(t), \mathbf{u}(t), t) + \mathbf{G}(t)\mathbf{w}(t) \tag{5.1}$$

$$\widetilde{\mathbf{y}}_k = \mathbf{h}(\mathbf{x}_k) + \boldsymbol{\nu}_k \tag{5.2}$$

where

$\mathbf{x}$: true value

$\hat{\mathbf{x}}$: estimated value

$\widetilde{\mathbf{y}}$: measured value

and the vector $\mathbf{w}(t)$ is a zero mean white process. The matrix $\mathbf{G}(t)$ is an identity matrix with size equal to the length of the state vector. The measurement model is corrupted by a zero mean white sequence $\boldsymbol{\nu}_k$ [31]. The process noise $\mathbf{w}(t)$ and the measurement noise $\boldsymbol{\nu}_k$ are assumed to be uncorrelated to each other. The spectral density of the process noise is given by $\mathbf{Q}(t)$ while the covariance matrix corresponding to the measurement noise is given by $\mathbf{R}_k$. The covariances of the zero mean white process and white sequence are found as follows where E denotes the expected value.

$$E\left\{\mathbf{w}(t)\mathbf{w}^T(\tau)\right\} = \mathbf{Q}(t)\delta(t-\tau)$$

$$E\left\{\boldsymbol{\nu}_k\boldsymbol{\nu}_j^T\right\} = \begin{cases} \mathbf{0} & k \neq j \\ \mathbf{R}_k & k = j \end{cases}$$

where $\delta(t-\tau)$ is the Dirac delta function defined by Equations 5.3 [39].

$$\delta(t-\tau) = \begin{cases} \infty, & t = \tau \\ 0, & t \neq \tau \end{cases} \tag{5.3}$$

Given an initial state vector and error covariance matrix

$$\begin{aligned} \hat{\mathbf{x}}(t_0) &= \hat{\mathbf{x}}_0 \\ \mathbf{e} &= \mathbf{x} - \hat{\mathbf{x}} \\ \mathbf{P}_0 &= E\left\{\mathbf{e}_0\mathbf{e}_0^T\right\} \end{aligned}$$

the Kalman gain at a given time step, $\mathbf{K}_k$, can be computed using Equation 5.4.

$$\mathbf{K}_k = \mathbf{P}_k^-\mathbf{H}_k^T(\hat{\mathbf{x}}_k^-)[\mathbf{H}_k(\hat{\mathbf{x}}_k^-)\mathbf{P}_k^-\mathbf{H}_k^T(\hat{\mathbf{x}}_k^-) + \mathbf{R}_k]^{-1} \tag{5.4}$$

where

$$\mathbf{H}_k(\hat{\mathbf{x}}_k^-) \equiv \left.\frac{d\mathbf{h}}{d\mathbf{x}}\right|_{\hat{\mathbf{x}}_k^-} \tag{5.5}$$

After the gain and measurement sensitivity matrices are calculated, the discrete update process is followed. The update process uses the residual between the measured and estimated values multiplied by the Kalman gain to produce a correction vector which is then added to the *a priori* state vector, as shown in Equation 5.6. In addition to updating the state vector, the estimation error covariance matrix is also updated at this point using Equation 5.7.

$$\hat{\mathbf{x}}_k^+ = \hat{\mathbf{x}}_k^- + \mathbf{K}_k[\widetilde{\mathbf{y}}_k - \mathbf{h}(\hat{\mathbf{x}}_k^-)] \tag{5.6}$$

$$\mathbf{P}_k^+ = (\mathbf{I}_{n\times n} - \mathbf{K}_k\mathbf{H}_k(\hat{\mathbf{x}}_k^-))\mathbf{P}_k^-(\mathbf{I}_{n\times n} - \mathbf{K}_k\mathbf{H}_k(\hat{\mathbf{x}}_k^-))^T + \mathbf{K}_k\mathbf{R}_k\mathbf{K}_k^T \tag{5.7}$$

After the update process has been completed, the system can be propagated for a single time step in order to determine the next estimate of the state vector. Integration techniques such as a 4^{th} order Runge Kutta method or Euler's method can be used to determine the next state estimate. The equations to be propagated are given by Equations 5.8-5.10.

$$\dot{\hat{\mathbf{x}}}(t) = \mathbf{f}(\hat{\mathbf{x}}(t), \mathbf{u}(t), t) \tag{5.8}$$

$$\dot{\mathbf{P}}(t) = \mathbf{F}(\hat{\mathbf{x}}(t), t)\mathbf{P}(t) + \mathbf{P}(t)\mathbf{F}^T(\hat{\mathbf{x}}(t), t) + \mathbf{G}(t)\mathbf{Q}(t)\mathbf{G}^T(t) \tag{5.9}$$

$$\mathbf{F}(\hat{\mathbf{x}}(t), t) \equiv \left.\frac{d\mathbf{f}}{d\mathbf{x}}\right|_{\hat{\mathbf{x}}(t)} \tag{5.10}$$

It is also possible to propagate the error covariance matrix using a discrete propagation process. In order to do so, the state model is discretized about a sample time, Δt. Equation 5.11 gives the conversion from continuous to discrete time given a sample time Δt.

$$\mathbf{x}(t_{k+1}) = \mathbf{\Phi}(t_{k+1}, t_k)\mathbf{x}(t_k) + \int_{t_k}^{t_{k+1}} \mathbf{\Phi}(t_{k+1}, \tau)\mathbf{G}(\tau)\mathbf{w}(\tau)\, d\tau \tag{5.11}$$

which can be simplified to

$$\mathbf{x}_{k+1} = \mathbf{\Phi}_k \mathbf{x}_k + \mathbf{w}_k \tag{5.12}$$

The vector $\mathbf{w}_k$ is a zero mean white sequence with a corresponding covariance given by Equation 5.13.

$$E\left\{\mathbf{w}_k \mathbf{w}_j^T\right\} = \begin{cases} \mathbf{0} & k \neq j \\ \mathbf{Q}_k & k = j \end{cases} \tag{5.13}$$

where $\mathbf{Q}_k$ is given by Equation 5.14.

$$\mathbf{Q}_k = \int_{t_k}^{t_{k+1}} \int_{t_k}^{t_{k+1}} \mathbf{\Phi}(t_{k+1}, \zeta)\mathbf{G}(\zeta)E\left[\mathbf{w}(\zeta)\mathbf{w}(\vartheta)\right]\mathbf{G}^T(\vartheta)\mathbf{\Phi}^T(t_{k+1}, \vartheta)d\zeta d\vartheta \tag{5.14}$$

The matrix $\mathbf{\Phi}_k$ is the state transition matrix which is found by propagating Equation 5.15 where $\mathbf{F}(t)$ retains the same definition as in Equation 5.10.

$$\dot{\mathbf{\Phi}}(t, t_k) = \mathbf{F}(t)\mathbf{\Phi}(t, t_k) \quad \mathbf{\Phi}(t_k, t_k) = \mathbf{I} \tag{5.15}$$

Making use of Equations 5.11-5.15, the discrete propagation of the error covariance matrix is given by Equation 5.16 where $\mathbf{P}_{k+1}^-$ refers to the current update of the error covariance matrix and $\mathbf{P}_k^+$ is the error covariance matrix of the previous time

step.

$$\mathbf{P}_{k+1}^{-} = \mathbf{\Phi}_k \mathbf{P}_k^{+} \mathbf{\Phi}_k^{T} + \mathbf{Q}_k \tag{5.16}$$

Equation 5.7 and Equation 5.16 are used to update and propagate the estimation error covariance matrix for the four Kalman filters. The above process is continued at a chosen sample time until the final time is reached. Figure 19 summarizes the equations used during the implementation of the EKF.

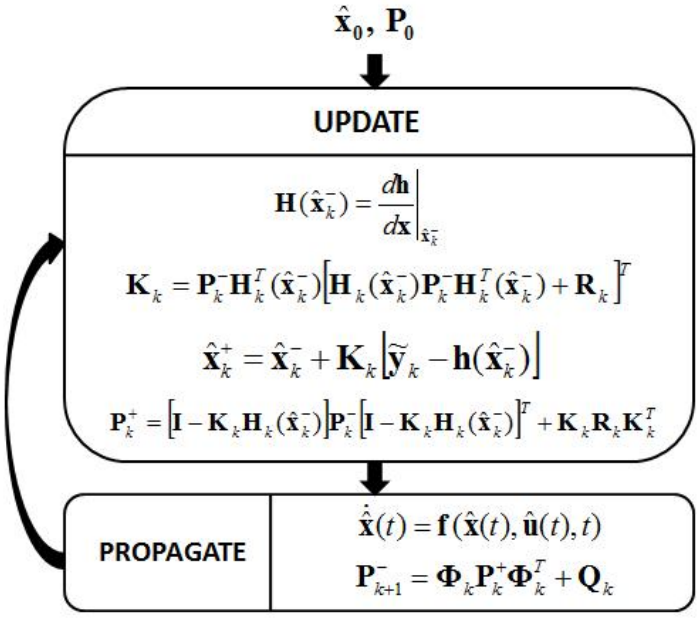

Fig. 19. Summary of EKF Procedure

B. Propagation Model

The state model used during the propagation portion of the four Kalman filters is described in this section. The state model is a propagation of the two body problem

including accelerations due to the oblateness of the Earth, atmospheric drag, and thruster firings. The state model for both the chaser and target vehicles is given by the following equations.

$$\dot{\hat{\mathbf{r}}} = \hat{\mathbf{v}} \tag{5.17}$$

$$\ddot{\hat{\mathbf{r}}} = \mathbf{g}\left(\hat{\mathbf{r}}\right) + \hat{\mathbf{a}} \tag{5.18}$$

where

$\hat{\mathbf{r}}$: estimate of spacecraft position, m

$\hat{\mathbf{v}}$: estimate of spacecraft velocity, $\frac{m}{s}$

$\hat{\mathbf{a}}$: estimate of acceleration, $\frac{m}{s^2}$

The gravitational acceleration is given by $\mathbf{g}\left(\hat{\mathbf{r}}\right)$ and includes effects due to the oblateness of the Earth. The gravitational acceleration is defined as [40]:

$$\begin{aligned}
\mathbf{g1}\left(\hat{\mathbf{r}}\right) &= \mathbf{u}_r + k_1\left(1 - 5U^2\right)\mathbf{u}_r + 2k_1 U \mathbf{u}_p \\
\mathbf{g2}\left(\hat{\mathbf{r}}\right) &= \mathbf{g1}\left(\hat{\mathbf{r}}\right) + 5k_2 U\left(3 - 7U^2\right)\mathbf{u_r} - 3k_2\left(1 - 5U^2\right)\mathbf{u}_p \\
\mathbf{g3}\left(\hat{\mathbf{r}}\right) &= \mathbf{g2}\left(\hat{\mathbf{r}}\right) + 3k_3\left(1 - 14U^2 + 21U^4\right)\mathbf{u}_r + 4k_3 U\left(3 - 7U^2\right)\mathbf{u}_p \\
\mathbf{g}\left(\hat{\mathbf{r}}\right) &= \frac{-\mu}{\hat{\mathbf{r}} \cdot \hat{\mathbf{r}}}\mathbf{g3}
\end{aligned}$$

where

$$
\begin{aligned}
k_1 &= \frac{3}{2} J_2 \left(\frac{R_e}{\hat{\mathbf{r}} \cdot \mathbf{u}_r} \right)^2 \\
k_2 &= \frac{1}{2} J_3 \left(\frac{R_e}{\hat{\mathbf{r}} \cdot \mathbf{u}_r} \right)^3 \\
k_3 &= -\frac{5}{8} J_4 \left(\frac{R_e}{\hat{\mathbf{r}} \cdot \mathbf{u}_r} \right)^4 \\
U &= (\mathbf{u}_r \cdot \mathbf{u}_p) \\
\mathbf{u}_r &= \frac{\hat{\mathbf{r}}}{\|\hat{\mathbf{r}}\|} \\
\mathbf{u}_p &= [0 \;\; 0 \;\; 1]^T
\end{aligned}
$$

and perturbation coefficients $J_{\#}$ and parameters are defined as follows.

$$
\begin{aligned}
J_2 &: J_2 \text{ perturbation coefficient, } 1.08263 \times 10^{-3} \\
J_3 &: J_3 \text{ perturbation coefficient, } -2.56 \times 10^{-6} \\
J_4 &: J_4 \text{ perturbation coefficient, } -1.58 \times 10^{-6} \\
R_e &: \text{radius of the Earth, } 6378.1363 \; km \\
\mu &: \text{gravitation constant}
\end{aligned}
$$

The estimated acceleration of the chaser vehicle during thruster firings is given by Equation 5.19. Equation 5.20 gives the acceleration each vehicle experiences due to atmospheric drag. When thruster firings occur, the acceleration due to atmospheric drag is assumed to be negligible. Therefore, Equation 5.20 is used during instances of free drift only.

$$
\hat{\mathbf{a}}_c = \hat{\mathbf{a}}_{imu} \tag{5.19}
$$

$$\hat{\mathbf{a}}_{c,t} = -D_{c,t}\frac{\hat{\mathbf{v}}_{c,t}}{\|\hat{\mathbf{v}}_{c,t}\|} \tag{5.20}$$

where

$$\begin{aligned} D_c &: \text{chaser atmospheric drag} \\ D_t &: \text{target atmospheric drag} \end{aligned}$$

It is assumed that the target is significantly larger than the chaser vehicle. As a result, the target vehicle is modeled to experience twice the drag of the chaser. The atmospheric drag on the chaser vehicle is modeled as $6.2 \times 10^{-6}\frac{m}{s^2}$ with the drag acting upon the target modeled as $12.4 \times 10^{-6}\frac{m}{s^2}$.

The state matrix for the chaser vehicle is given by Equation 5.21. There is a relation between the angular velocity and translational acceleration that is accounted for.

$$\mathbf{F}_c = \begin{bmatrix} \mathbf{0}_{3\times3} & \mathbf{I}_{3\times3} & \mathbf{0}_{3\times3} & \mathbf{0}_{3\times3} \\ \mathbf{J_2} & \mathbf{0}_{3\times3} & \hat{\mathbf{a}}^{\times} & \mathbf{T}^{i}_{imu} \\ \mathbf{0}_{3\times3} & \mathbf{0}_{3\times3} & -\widetilde{\boldsymbol{\omega}}^{\times} & \mathbf{0}_{3\times3} \\ \mathbf{0}_{3\times3} & \mathbf{0}_{3\times3} & \mathbf{0}_{3\times3} & \mathbf{0}_{3\times3} \end{bmatrix} \tag{5.21}$$

The matrices $\hat{\mathbf{a}}^{\times}$ and $\widetilde{\boldsymbol{\omega}}^{\times}$ are the skew symmetric matrices of the estimated acceleration and measured angular velocity vectors respectively. The transformation matrix $\mathbf{T}^{i}_{imu}$ is derived from $\bar{\mathbf{q}}^{i}_{imu}$. The matrix $\mathbf{J_2}$ is given as

$$\mathbf{J_2} = \begin{bmatrix} \frac{-m}{r^3} + \frac{3r_x^2}{r^2}\left(\frac{m}{r^3} + \Lambda(p-1)\right) & \frac{3r_x r_y}{r^2}\left(\frac{m}{r^3} + \Lambda(p-1)\right) & \frac{3r_x r_z}{r^2}\left(\frac{m}{r^3} + \Lambda(p+4)\right) \\ \frac{3r_x r_y}{r^2}\left(\frac{m}{r^3} + \Lambda(p-1)\right) & \frac{-m}{r^3} + \frac{3r_y^2}{r^2}\left(\frac{m}{r^3} + \Lambda(p-1)\right) & \frac{3r_y r_z}{r^2}\left(\frac{m}{r^3} + \Lambda(p+4)\right) \\ \frac{3r_x r_z}{r^2}\left(\frac{m}{r^3} + \Lambda(p+4)\right) & \frac{3r_y r_z}{r^2}\left(\frac{m}{r^3} + \Lambda(p+4)\right) & -(J_2(1,1) + J_2(2,2)) \end{bmatrix}$$

where

$$\begin{aligned} \Lambda &= \frac{\mu J_2 R_e^2}{r^5} \\ m &= \mu\left(1+\frac{3J_2R_e^2p}{4r^2}\right) \\ p &= 2\left(1-\frac{5r_z^2}{r^2}\right) \end{aligned}$$

with the perturbation coefficient J_2 and parameters definitions defined the same as above. Equation 5.22 gives the state matrix of the target vehicle.

$$\mathbf{F}_t = \begin{bmatrix} \mathbf{0}_{3\times3} & \mathbf{I}_{3\times3} \\ \mathbf{J_2} & \mathbf{0}_{3\times3} \end{bmatrix} \tag{5.22}$$

The spectral density corresponding to the zero mean white process noise $\mathbf{w}(t)$ on the position and velocity states of both vehicle as well as for the chaser attitude is $\mathbf{Q}_x(t)$. Since the estimation error covariance is propagated using Equation 5.16, the discrete form of the spectral density is needed. Using Equation 5.14, the spectral density $\mathbf{Q}_x(t)$ becomes covariance matrix $\mathbf{Q}_{x_k}$ and is given by the following.

$$\mathbf{Q}_{x_k} = \begin{bmatrix} \mathbf{Q}_{p_{c_k}} & \mathbf{Q}_{pv_{c_k}} & \mathbf{0}_{3\times3} & \mathbf{Q}_{p_{ct_k}} & \mathbf{Q}_{pv_{ct_k}} \\ \mathbf{Q}_{pv_{c_k}} & \mathbf{Q}_{v_{c_k}} & \mathbf{0}_{3\times3} & \mathbf{Q}_{pv_{ct_k}} & \mathbf{Q}_{v_{ct_k}} \\ \mathbf{0}_{3\times3} & \mathbf{0}_{3\times3} & \mathbf{Q}_{q_k} & \mathbf{0}_{3\times3} & \mathbf{0}_{3\times3} \\ \mathbf{Q}_{p_{ct_k}} & \mathbf{Q}_{pv_{ct_k}} & \mathbf{0}_{3\times3} & \mathbf{Q}_{p_{t_k}} & \mathbf{Q}_{pv_{t_k}} \\ \mathbf{Q}_{pv_{ct_k}} & \mathbf{Q}_{v_{ct_k}} & \mathbf{0}_{3\times3} & \mathbf{Q}_{pv_{t_k}} & \mathbf{Q}_{v_{t_k}} \end{bmatrix}$$

The definition of each individual covariance matrix in $\mathbf{Q}_{x_k}$ remains the same for all four Kalman filters studied. The individual covariance matrices are given as follows [40].

$$
\begin{aligned}
\mathbf{Q}_{p_{c_k}} &= \frac{1}{3}\mathbf{Q}_{v_{c_k}}\Delta t^2 \\
\mathbf{Q}_{pv_{c_k}} &= \frac{1}{2}\mathbf{Q}_{v_{c_k}}\Delta t \\
\mathbf{Q}_{v_{c_k}} &= \mathbf{T}^i_{lvlh}\mathbf{Q}_{c_v}(t)\mathbf{T}^{lvlh}_i\Delta t \\
\mathbf{Q}_{\theta_k} &= \mathbf{Q}_{\theta}(t) \\
\mathbf{Q}_{p_{t_k}} &= \frac{1}{3}\mathbf{Q}_{v_{t_k}}\Delta t^2 \\
\mathbf{Q}_{pv_{t_k}} &= \frac{1}{2}\mathbf{Q}_{v_{t_k}}\Delta t \\
\mathbf{Q}_{v_{t_k}} &= \mathbf{T}^i_{lvlh}\mathbf{Q}_{t_v}(t)\mathbf{T}^{lvlh}_i\Delta t \\
\mathbf{Q}_{p_{ct_k}} &= \frac{19}{20}\mathbf{Q}_{p_{t_k}} \\
\mathbf{Q}_{pv_{ct_k}} &= \frac{19}{20}\mathbf{Q}_{pv_{t_k}} \\
\mathbf{Q}_{v_{ct_k}} &= \frac{19}{20}\mathbf{Q}_{v_{t_k}}
\end{aligned}
$$

Table XIII gives the spectral densities corresponding to each individual covariance matrix for each Kalman filter studied. The matrix $\mathbf{I_3}$ denotes a 3×3 identity matrix.

Table XIII. Spectral Density Values for all Kalman Filters

Spectral Density	Value	Units
$\mathbf{Q}_{c_v}(t)$	$9 \times 10^{-6}\ \mathbf{I_3}$	$\left(\frac{m}{s^{1.5}}\right)$
$\mathbf{Q}_{\theta}(t)$	$1 \times 10^{-11}\ \mathbf{I_3}$	$\left(\frac{rad}{\sqrt{s}}\right)$
$\mathbf{Q}_{t_v}(t)$	$9 \times 10^{-6}\ \mathbf{I_3}$	$\left(\frac{m}{s^{1.5}}\right)$

C. Position Velocity Kalman Filter

In this section the development of a position velocity (PV) EKF will be discussed. The PV EKF is a filter that approximates the absolute position and velocity of the chaser and target vehicles. The state vector includes both the position and velocity vectors of each vehicle as well as the orientation angle set (three angles) of the chaser. The theory presented in the previous section is assumes the process and measurement noises are white. However, the process noise, measurement noise or both are occasionally colored noise. The Bancroft and velocity estimation algorithms as defined in Chapter II are utilized to determine the position and velocity of each vehicle which are corrupted by non-white noise. The equations developed for an EKF in section A assumed the process and measurement noise are zero mean white noise. In order to compensate for colored measurement noise, additional states are augmented to the state vector. In this thesis, any augment states are modeled by first order Gauss-Markov processes with variable time constants and standard deviations equal to the expected value of the error resulting from the colored measurement noise. GPS measurements are used to calculate an estimated position and velocity that is outputted by the GPS sensor. The estimated position and velocity vectors supplied by the GPS sensor are then used as the measurements processed by the PV filter.

The state and measurement vectors are given as follows.

$$\begin{aligned} \mathbf{x} &= \begin{bmatrix} \mathbf{r}_c^T & \mathbf{v}_c^T & \boldsymbol{\theta}^T & \mathbf{r}_t^T & \mathbf{v}_t^T \end{bmatrix}^T \\ \widetilde{\mathbf{y}} &= \begin{bmatrix} \widetilde{\mathbf{r}}_c^T & \widetilde{\mathbf{v}}_c^T & \widetilde{\mathbf{r}}_t^T & \widetilde{\mathbf{v}}_t^T \end{bmatrix}^T \end{aligned}$$

In addition to the state and measurement vectors, a bias present in the accelerometer states that are used to calculate the position and velocity during the propagation

portion of the Kalman filter is modeled. The accelerometer bias states are modeled as first order Gauss-Markov processes with the steady state standard deviation of 40μg and time constant τ_a of 1 hour [38]. The accelerometer bias states are given by:

$$\mathbf{a}_b = \begin{bmatrix} a_{b_x} & a_{b_y} & a_{b_z} \end{bmatrix}^T$$

Since the state vector can be represented as a linear combination of the measurement vector and the accelerometer bias is not present in either the state or measurement vectors, the EKF measurement equation is simplified from a non-linear to a linear form. The PV EKF state and measurement equations are given by the following set of equations.

$$\dot{\mathbf{x}}(t) = \mathbf{f}(\mathbf{x}(t), \mathbf{u}(t), t) + \mathbf{G}(t)\mathbf{w}(t) \tag{5.23}$$

$$\widetilde{\mathbf{y}}_k = \mathbf{H}_k \mathbf{x}_k + \boldsymbol{\xi}_k \tag{5.24}$$

where the vector $\mathbf{w}(t)$ is a zero mean white process and the vector $\boldsymbol{\xi}_k$ is a zero mean white sequence. The matrix $\mathbf{G}(t)$ is an identity matrix. As previously mentioned, additional states are needed to model the colored measurement noise. The augmented state vector and model for the PV Kalman filter is given as follows:

$$\mathbf{x}' = \begin{bmatrix} \mathbf{r}_c^T & \mathbf{v}_c^T & \boldsymbol{\theta}^T & \mathbf{r}_t^T & \mathbf{v}_t^T & \boldsymbol{\xi}_{r_c}^T & \boldsymbol{\xi}_{v_c}^T & \boldsymbol{\xi}_{r_t}^T & \boldsymbol{\xi}_{v_t}^T & \mathbf{a}_b^T \end{bmatrix}^T$$

$$\dot{\mathbf{x}}'(t) = \mathbf{f}'(\mathbf{x}'(t), \mathbf{u}'(t), t) + \mathbf{w}'(t) \tag{5.25}$$

$$\widetilde{\mathbf{y}}_k = \mathbf{H}_k{}' \mathbf{x}_k{}' + \boldsymbol{\xi}_k{}' \tag{5.26}$$

where $\mathbf{f}'(\mathbf{x}'(t), \mathbf{u}'(t), t)$ contains the new state equations excluding the white sequence

for the correlated random variables in addition to the original state equations for the position and velocity. The new white process $\mathbf{w}'(t)$, measurement sensitivity matrix $\mathbf{H}_k{}'$, and white sequence $\boldsymbol{\xi}_k{}'$ are given by Equations 5.27-5.29.

The measurement sensitivity matrix is modified to include the contribution of the correlated random variables. Since the random variables are used to model the colored noise present on the measurements, an identity matrix is inserted for the derivative of the measurements with respect to the random variables. The zero mean white process noise vector is augmented to include the noise present in the correlated random variable states. With the measurement noise being modeled as a first order Gauss-Markov process, there is no longer a white sequence present in the measurement equation hence $\boldsymbol{\xi}_k'$ becomes a vector of zeros.

$$\mathbf{H}_k{}' = [\mathbf{H}_k \;\; \mathbf{I}_{12\times 12} \;\; \mathbf{0}_{12\times 3}] \tag{5.27}$$

$$\mathbf{w}(t)' = [\mathbf{w}_x(t) \;\; \boldsymbol{\nu}(t) \;\; \mathbf{w}_a(t)\,]^T \tag{5.28}$$

$$\boldsymbol{\xi}_k{}' = \mathbf{0}_{12\times 1} \tag{5.29}$$

Note that $\mathbf{I}$ refers to an identity matrix of size n x n and $\mathbf{0}$ refers to a zero matrix of vector of size m x p or m x 1.

The colored noise is modeled as a first order Gauss-Markov process for all 12 states with 1σ values equal to the standard deviation for either the position or velocity depending on which state the noise affects. Equation 5.30 gives the continuous time representation of the correlated random variables while Equation 5.31 gives the discrete time representation of the Gauss-Markov first order process used to propagate the correlated random variables [22].

$$\dot{\boldsymbol{\xi}}(t) = -\frac{1}{\tau_{pv}}\boldsymbol{\xi}(t) + \boldsymbol{\nu}(t) \tag{5.30}$$

$$\boldsymbol{\xi}_{k+1} = \boldsymbol{\xi}_k \, e^{-\frac{\Delta t}{\tau_{pv}}} + \boldsymbol{\nu}_k \tag{5.31}$$

where the time constant τ_{pv} is 50 seconds, $\boldsymbol{\nu}(t)$ is a zero mean white process and $\boldsymbol{\nu}_k$ is a zero mean white sequence. The steady state standard deviations used for the correlated random variables are 20 meters for chaser position, 0.3 meters per second for chaser velocity, 15 meters for target position, and 0.2 meters per second for target velocity. The standard deviations for the correlated random variables are used to determine the process noise spectral density corresponding to the random variables given by Equation 5.33. Equation 5.31 can be re-written as:

$$\boldsymbol{\xi}_{k+1} = \boldsymbol{\Upsilon}_k \boldsymbol{\xi}_k + \boldsymbol{\nu}_k \tag{5.32}$$

where the matrix $\boldsymbol{\Upsilon}_k$ is

$$\boldsymbol{\Upsilon}_k = e^{-\frac{\Delta t}{\tau_{pv}}} \mathbf{I}_{12\times 12}$$

With the definition of a new augmented model, the spectral density of the white process noise and covariance matrix of the measurement noise are modified to include the spectral density and variance of the colored noise and accelerometer bias. The new spectral density, $\mathbf{Q}'(t)$, contains the previously known spectral density $\mathbf{Q}_x(t)$ corresponding to the original state vector, the spectral density corresponding to the colored noise and the spectral density of the accelerometer bias.

$$\mathbf{Q}'(t) = \begin{bmatrix} \mathbf{Q}_x(t) & \mathbf{0}_{15\times12} & \mathbf{0}_{15\times3} \\ \mathbf{0}_{12\times15} & \mathbf{Q}_\xi(t) & \mathbf{0}_{12\times3} \\ \mathbf{0}_{3\times15} & \mathbf{0}_{3\times12} & \mathbf{Q}_a(t) \end{bmatrix}$$

where $\mathbf{Q}_x(t)$ is the known spectral density corresponding to the white process noise present on the position, velocity and attitude states, $\mathbf{Q}_\xi(t)$ is defined as the spectral density of the colored noise, and $\mathbf{Q}_a(t)$ is the spectral density relating to the accelerometer bias states. The spectral density corresponding to the white noise process present on the correlated random variables used to model the colored noise is given as follows:

$$\mathbf{Q}_\xi(t) = \begin{bmatrix} \mathbf{Q}_{pc}(t) & \mathbf{0}_{3\times3} & \mathbf{0}_{3\times3} & \mathbf{0}_{3\times3} \\ \mathbf{0}_{3\times3} & \mathbf{Q}_{vc}(t) & \mathbf{0}_{3\times3} & \mathbf{0}_{3\times3} \\ \mathbf{0}_{3\times3} & \mathbf{0}_{3\times3} & \mathbf{Q}_{pt}(t) & \mathbf{0}_{3\times3} \\ \mathbf{0}_{3\times3} & \mathbf{0}_{3\times3} & \mathbf{0}_{3\times3} & \mathbf{Q}_{vt}(t) \end{bmatrix}$$

The first subscript defines the measurement, either position or velocity, and the second subscript defines the vehicle, either chaser or target. The spectral density of a first order Gauss-Markov process assuming a steady state standard deviation, $\sigma_{pv_{ss}}$, is given by Equation 5.33 where the subscript pv denotes position or velocity depending upon which error state is being modeled. Equation 5.33 is used to determine the spectral density of the correlated random variable states by replacing $\sigma_{pv_{ss}}$ and τ_{pv} with the corresponding values.

$$\mathbf{Q}_{pv}(t) = \frac{2}{\tau_{pv}}\sigma^2_{pv_{ss}} \cdot \mathbf{I}_{3\times3} \tag{5.33}$$

The spectral density $\mathbf{Q}_a(t)$ corresponds to the process noise present in the accelerometer bias states and is found by substituting the corresponding values for the

time constant and steady state standard deviations of the accelerometer bias into Equation 5.33. It is assumed that steady state deviation and time constant of the accelerometer bias is the same in every direction therefore the resulting value from Equation 5.33 is multiplied by an identity matrix of size three.

In order to make use of Equation 5.16, the spectral density matrix $\mathbf{Q}'(t)$ is transformed into the covariance matrix of a white sequence, $\mathbf{Q}'_k$, using Equation 5.14. The colored noise being modeled as a first order Gauss-Markov process is the measurement noise resulting from the pseudorange errors. As a result, the steady state values of the errors being modeled are known. The steady state values are used to determine the covariance matrix, $\mathbf{Q}_{\xi_k}$. Although the noise in each position and velocity state is correlated to one another the covariance matrix, $\mathbf{Q}_{\xi_k}$, is modeled to be a diagonal matrix with each diagonal entry calculated by Equation 5.34.

$$\mathbf{Q}_{\xi_{k_{ii}}} = \sigma^2_{pv_{ss}} \left(1 - e^{-\frac{2\Delta t}{\tau_{pv}}}\right) \quad for \;\; ii = 1, ..., 12 \tag{5.34}$$

Note the subscript, s, refers to the current measurement being considered, either position or velocity and the subscript, ii, refers to the entry corresponding to the ith column and row. The steady state standard deviations, $\sigma_{pv_{ss}}$, corresponds to the errors present on the position and velocity measurements. The covariance matrix, $\mathbf{Q}_{a_k}$, corresponding to the accelerometer bias is given by Equation 5.35.

$$\mathbf{Q}_{a_k} = \sigma^2_a \left(1 - e^{\frac{-2\Delta t}{\tau_a}}\right) \cdot \mathbf{I}_{3\times 3} \tag{5.35}$$

As for the new measurement covariance matrix $\mathbf{R}_k$, the covariance matrix is a square zero matrix the size of the measurement vector due to the definition of $\boldsymbol{\xi}'$.

The PV EKF estimates the position and velocity of each vehicle as well as the noise present in the measurements. Equations 5.36-5.38 define the error between the

true and estimated states.

$$\mathbf{e}_{p_s} = \mathbf{r}_s - \hat{\mathbf{r}}_s \tag{5.36}$$

$$\mathbf{e}_{v_s} = \mathbf{v}_s - \hat{\mathbf{v}}_s \tag{5.37}$$

$$\mathbf{e}_{\xi_s} = \boldsymbol{\xi}_{p/v_s} - \hat{\boldsymbol{\xi}}_{p/v_s} \tag{5.38}$$

where

$$\boldsymbol{\xi}_{p_s} = \widetilde{\mathbf{r}}_s - \mathbf{r}_s \tag{5.39}$$

$$\boldsymbol{\xi}_{v_s} = \widetilde{\mathbf{v}}_s - \mathbf{v}_s \tag{5.40}$$

In order to analyze the performance of the designed PV Kalman filter, the error values resulting from Equations 5.36-5.38 are graphed along with 1σ covariance derived from the estimation error covariance, $\mathbf{P}$ in Equation 5.7 and Equation 5.16. Over the course of the simulation, the filter does not process certain measurements due to fewer than four visible satellites or poor geometry resulting in bad measurements. As a result, the 1σ covariance increases, relaying the message that the uncertainty in the estimated state has increased. When the measurement quality is once again acceptable and measurements are processed the 1σ covariance will decrease, often rapidly, due to the ability of the filter to accurately estimate the state and reduce the uncertainty in the estimated state.

D. Relative Pseudorange Kalman Filter

The purpose of this section is to discuss the development of a relative pseudorange (RGPS) EKF. One difference between the RGPS EKF and PV EKF is the measurements being processed. The PV EKF processes position and velocity measurements while the RGPS EKF processes relative pseudorange measurements. The state vector differs in the additional states being modeled. For the RGPS EKF, the relative clock bias and clock drift are modeled adding only two additional states (Δb, Δf) as compared to 12 for the PV EKF. Even though more than six GPS satellites may be visible at a given time, only six relative pseudorange measurements are processed during each update of the estimate. By omitting additional measurements, the speed at which the filter performs increases. The measurement vector is populated by relative pseudoranges, $\delta\rho$, found by differencing the chaser and target pseudoranges corresponding to the same GPS satellite. The communication time delay between the two vehicles is neglected from this analysis. The state and measurement vectors for the RGPS EKF are defined as follows.

$$\begin{aligned} \mathbf{x} &= \begin{bmatrix} \mathbf{r}_c^T & \mathbf{v}_c^T & \boldsymbol{\theta}^T & \mathbf{r}_t^T & \mathbf{v}_t^T & \Delta b & \Delta f & \mathbf{a}_b^T \end{bmatrix}^T \\ \widetilde{\mathbf{y}} &= \begin{bmatrix} \delta\rho_i \cdots \delta\rho_n \end{bmatrix}^T \end{aligned}$$

Note that n is the total number of processed pseudorange measurements and cannot exceed six. The accelerometer bias is modeled in the same manner as is described in Section C. The relative clock bias and drift are modeled using the same random walk process given by Equation 2.3 with the relative clock bias and drift substituted for the clock bias and drift of a single receiver. Under the assumption that the bias and drift of the two receivers are uncorrelated to each other, Equation 5.41

gives the covariance matrix $\mathbf{Q}_{\Delta bf_k}$.

$$\mathbf{Q}_{\Delta bf_k} = \mathbf{Q}_{bf_1} + \mathbf{Q}_{bf_2} \tag{5.41}$$

The spectral density matrix corresponding to the zero mean white process present in the state model is transformed into the covariance matrix of a white sequence by Equation 5.14. The covariance matrix $\mathbf{Q}_k$ is needed since the propagation of the estimation error covariance is performed using Equation 5.16. The covariance matrix $\mathbf{Q}_k$ is given as follows.

$$\mathbf{Q}_k = \begin{bmatrix} \mathbf{Q}_{x_k} & \mathbf{0}_{15\times 2} & \mathbf{0}_{15\times 3} \\ \mathbf{0}_{2\times 15} & \mathbf{Q}_{\Delta bf_k} & \mathbf{0}_{2\times 3} \\ \mathbf{0}_{3\times 15} & \mathbf{0}_{3\times 2} & \mathbf{Q}_{a_k} \end{bmatrix}$$

The covariance matrix $\mathbf{Q}_{x_k}$ is given for the position, velocity and attitude states. The covariance matrix corresponding to the clock bias and drift, $\mathbf{Q}_{\Delta bf_k}$, is defined in Equation 5.41 and the covariance matrix corresponding to the accelerometer bias is given by Equation 5.35.

Since the same satellites must be seen by both the target and chaser vehicles in order to calculate relative pseudoranges, the number of measurements vary between sampling times. Due to the number of measurements differing from time step to time step, a method known as sequential measurement processing is utilized to analyze the data. Sequential measurement processing allows for the processing of one measurement at a time. The method repeats the update process as defined in Section A for a single time step until all measurements are processed before proceeding to the propagation of states. The primary assumption made during the implementation of the modified method is the measurement noise covariance matrix $\mathbf{R}_k$ is block diagonal meaning no correlation between measurement errors at time t_k. In the current

case of study, the measurement noise covariance matrix is block diagonal. If $\mathbf{R}_k$ is not block diagonal, i.e. correlated error measurements, a linear combination of the measurements can be formed in such a way that the resulting set of measurements contains uncorrelated errors [22]. The measurement noise covariance matrix is given as:

$$\mathbf{R}_k = 2\sigma_{\delta\rho}^2 \mathbf{I}_{n\times n}$$

where $\sigma_{\delta\rho}$ is 7 meters. The steady state standard deviation is high due to the remaining measurement noise being colored instead of white. Since the measurements are relative pseudoranges, the measurement noise covariance matrix corresponding to each pseudorange is added together hence the factor of two.

The measurement sensitivity matrix, $\mathbf{H}_k$, varies with each measurement processed. As defined in Section A, the measurement sensitivity matrix is populated with the partials of the measurements with respect to the corresponding states. For the RGPS EKF, the measurements are the difference between the pseudoranges of each vehicle defined by Equation 5.42.

$$\rho_{s_i} = \|\mathbf{r}_{gps_i} - \mathbf{r}_s\| \tag{5.42}$$

The difference between the pseudoranges of each vehicle results in relative pseudoranges. Common satellites shared by both vehicles are determined using the pseudo random numbers assigned to the GPS satellites. Once the common satellites are determined, the relative measurements are computed by differencing the corresponding pseudoranges of each vehicle. Equation 5.43 is used to calculate the measurement data.

$$\delta\rho_i = \rho_{t_i} - \rho_{c_i} \tag{5.43}$$

The gradient of the relative pseudorange measurement with respect to the state vector is given by Equations 5.44-5.47.

$$\frac{d\delta\rho_i}{d\mathbf{r}_c} = \frac{(\mathbf{r}_{gps_i} - \mathbf{r}_c)^T}{\rho_c} \tag{5.44}$$

$$\frac{d\delta\rho_i}{d\mathbf{r}_t} = -\frac{(\mathbf{r}_{gps_i} - \mathbf{r}_t)^T}{\rho_t} \tag{5.45}$$

$$\frac{d\delta\rho_i}{d\mathbf{v}_c} = [0 \;\; 0 \;\; 0] \tag{5.46}$$

$$\frac{d\delta\rho_i}{d\mathbf{v}_t} = [0 \;\; 0 \;\; 0] \tag{5.47}$$

Line of sight vectors can be defined via Equations 5.48-5.49.

$$\mathbf{l}_{c_i} = \frac{(\mathbf{r}_{gps_i} - \mathbf{r}_c)}{\rho_c} \tag{5.48}$$

$$\mathbf{l}_{t_i} = \frac{(\mathbf{r}_{gps_i} - \mathbf{r}_t)}{\rho_t} \tag{5.49}$$

The derivatives of the relative pseudorange measurements with respect to the attitude angles of the chaser vehicle involves a knowledge of the location of the GPS receiver antenna. Given the location of the GPS receiver antennas as $\mathbf{r}_{a_c}$ and $\mathbf{r}_{a_t}$, the velocities are given by:

$$\begin{aligned} \mathbf{v}_{a_c} &= \boldsymbol{\omega}_c \times \mathbf{r}_{a_c} \\ \mathbf{v}_{a_t} &= \boldsymbol{\omega}_t \times \mathbf{r}_{a_t} \end{aligned}$$

Let the skew matrix, $[\mathbf{u}^{\times}]$, be defined by Equation 5.50.

$$[\mathbf{u}^{\times}] = \begin{bmatrix} 0 & -u_3 & u_2 \\ u_3 & 0 & -u_1 \\ -u_2 & u_1 & 0 \end{bmatrix} \tag{5.50}$$

where $\mathbf{u}$ is an arbitrary 3x1 column vector. The matrix that transforms one frame to another frame, derived from Euler parameters (quaternions) relating the two frames, is given by Equation 5.51 [41].

$$\mathbf{T}(\bar{\mathbf{q}}) = I_{3\times 3} - 2q_0[\mathbf{q}_v^{\times}] + 2[\mathbf{q}_v^{\times}]^2 \tag{5.51}$$

where the Euler parameter set is defined scalar part first.

$$\bar{\mathbf{q}} = \begin{bmatrix} q_0 \\ \mathbf{q}_v \end{bmatrix}$$

Making use of Equations 5.50 and 5.51, the partial derivatives of the position and velocity of the chaser and target vehicles with respect to the chaser attitude parameters are defined by Equations 5.52-5.55.

$$\frac{d\mathbf{r}_c}{d\boldsymbol{\theta}} = [(\mathbf{T}^T(\bar{\mathbf{q}_\mathbf{c}})\mathbf{r}_{a_c})^{\times}] \tag{5.52}$$

$$\frac{d\mathbf{v}_c}{d\boldsymbol{\theta}} = [(\mathbf{T}^T(\bar{\mathbf{q}}_\mathbf{c})\mathbf{v}_{a_c})^\times] \tag{5.53}$$

$$\frac{d\mathbf{r}_t}{d\boldsymbol{\theta}} = [(\mathbf{T}^T(\bar{\mathbf{q}}_\mathbf{t})\mathbf{r}_{a_t})^\times] \tag{5.54}$$

$$\frac{d\mathbf{v}_t}{d\boldsymbol{\theta}} = [(\mathbf{T}^T(\bar{\mathbf{q}}_\mathbf{t})\mathbf{v}_{a_t})^\times] \tag{5.55}$$

The gradient of the relative pseudorange with respect to chaser attitude parameter set is computed via Equation 5.56.

$$\frac{d\delta\rho_i}{d\boldsymbol{\theta}} = \mathbf{l}_{c_i}\frac{d\mathbf{r}_c}{d\boldsymbol{\theta}} - \mathbf{l}_{t_i}\frac{d\mathbf{r}_t}{d\boldsymbol{\theta}} \tag{5.56}$$

With the gradients of the measurements with respect to the original states defined, the remaining partial derivatives needed to fully populate the sensitivity matrix are those with respect to the clock bias and drift. The partial derivatives of the relative pseudorange with respect to the relative clock bias and drift, Δb and Δf, are given by Equations 5.57-5.58.

$$\frac{d\delta\rho_i}{d\Delta b} = 1 \tag{5.57}$$

$$\frac{d\delta\rho_i}{d\Delta f} = 0 \tag{5.58}$$

With the knowledge of the required gradients, the sensitivity matrix is constructed using Equation 5.59.

$$\mathbf{H}_{k_i} = \begin{bmatrix} \frac{d\delta\rho_i}{d\mathbf{r}_c} & \frac{d\delta\rho_i}{d\mathbf{v}_c} & \frac{d\delta\rho_i}{d\boldsymbol{\theta}} & \frac{d\delta\rho_i}{d\mathbf{r}_t} & \frac{d\delta\rho_i}{d\mathbf{v}_t} & \frac{d\delta\rho_i}{d\Delta b} & \frac{d\delta\rho_i}{d\Delta f} & \mathbf{0}_{1\times 3} \end{bmatrix} \tag{5.59}$$

The sensitivity matrix is rebuilt every time a new measurement is processed,

which is shown in Equation 5.59 by the subscript i. The subscript, k, denotes the current time step when the measurements are acquired. After the sensitivity matrix is computed, the Kalman gain is computed followed by the updating of the state vector and covariance matrix. After all measurements have been processed and the updates completed, the final updated estimates for the states and error covariance from the current time step are propagated and the process is repeated until the final time is reached.

$$\mathbf{e}_{p_{rel}} = (\mathbf{r}_t - \mathbf{r}_c) - (\hat{\mathbf{r}}_t - \hat{\mathbf{r}}_\mathbf{c}) \tag{5.60}$$

The estimation errors are determined in a similar manner as is given for the PV EKF given by Equations 5.36-5.37. The relative estimation error is determined by differencing the inertial position and velocity of both vehicles as shown in Equation 5.60. Monte Carlo runs are performed and estimation errors plotted against the corresponding error covariances. Since relative measurements are being processed, the RGPS EKF is expected to perform well with respect to relative state estimation and poorly with respect to absolute state estimation.

E. Pseudorange Kalman Filter

A pseudorange (GPS) EKF is derived in this section. The GPS EKF estimates the position and velocity vectors and clock bias and drift of both vehicles as well as common pseudorange errors based upon pseudorange measurements. Additional states are augmented onto the existing state vector to estimate the common pseudorange errors unique to each GPS satellite. The GPS EKF can process up to six pseudorange measurements. Measured pseudoranges from common GPS satellites are processed first. If there are less than six common satellites, pseudorange measurements from

non-common satellites are processed. In cases when one or both vehicles see four or less satellites, less than six pseudorange measurements are processed.

The state and measurement vectors used for the GPS EKF are given as follows.

$$\begin{aligned} \mathbf{x} &= \begin{bmatrix} \mathbf{r}_c^T & \mathbf{v}_c^T & \boldsymbol{\theta}^T & b_c & f_c & \mathbf{r}_t^T & \mathbf{v}_t^T & b_t & f_t & \mathbf{a}_b^T & \boldsymbol{\xi}_\rho^T \end{bmatrix}^T \\ \widetilde{\mathbf{y}} &= \begin{bmatrix} \rho_{c_1} & \rho_{c_2} \cdots & \rho_{c_n} & \rho_{t_1} & \rho_{t_2} & \cdots & \rho_{t_n} \end{bmatrix}^T \end{aligned}$$

The accelerometer states are modeled using a first order Gauss-Markov process with a steady state standard deviation of 40 μg and a time constant of one hour [38]. The common pseudorange errors are modeled using a first order Gauss-Markov process with a steady state standard deviation, σ_{ξ_ρ}, of 6 meters and a time constant, τ_{ξ_ρ}, of 100 seconds. Equation 5.61 is used during the propagation of the common pseudorange errors. Since the estimation error covariance is propagated using Equation 5.16, the covariance matrix $\mathbf{Q}_{\xi\rho_k}$ is given corresponding to the common pseudorange errors.

$$\dot{\boldsymbol{\xi}}(t) = -\frac{1}{\tau_{\xi_\rho}}\boldsymbol{\xi}(t) + \boldsymbol{\eta}(t) \tag{5.61}$$

$$\mathbf{Q}_{\xi\rho_k} = \sigma_{\xi_\rho}^2 \left(1 - e^{\frac{-2\Delta t}{\tau_{\xi_\rho}}}\right) \cdot \mathbf{I}_{6\times 6} \tag{5.62}$$

The covariance matrix, $\mathbf{Q}_k$, is given as follows:

$$\mathbf{Q}_k = \begin{bmatrix} \mathbf{Q}_{c_{pv_k}} & \mathbf{0}_{6\times3} & \mathbf{0}_{6\times2} & \mathbf{Q}_{c/t} & \mathbf{0}_{6\times2} & \mathbf{0}_{6\times3} & \mathbf{0}_{6\times6} \\ \mathbf{0}_{3\times6} & \mathbf{Q}_{c_{\theta_k}} & \mathbf{0}_{3\times2} & \mathbf{0}_{3\times6} & \mathbf{0}_{3\times2} & \mathbf{0}_{3\times3} & \mathbf{0}_{3\times6} \\ \mathbf{0}_{2\times6} & \mathbf{0}_{2\times3} & \mathbf{Q}_{c_{bf_k}} & \mathbf{0}_{2\times6} & \mathbf{0}_{2\times2} & \mathbf{0}_{2\times3} & \mathbf{0}_{2\times6} \\ \mathbf{Q}_{t/c} & \mathbf{0}_{6\times3} & \mathbf{0}_{6\times2} & \mathbf{Q}_{t_{pv_k}} & \mathbf{0}_{6\times2} & \mathbf{0}_{6\times3} & \mathbf{0}_{6\times6} \\ \mathbf{0}_{2\times6} & \mathbf{0}_{2\times3} & \mathbf{0}_{2\times2} & \mathbf{0}_{2\times6} & \mathbf{Q}_{t_{bf_k}} & \mathbf{0}_{2\times3} & \mathbf{0}_{2\times6} \\ \mathbf{0}_{3\times6} & \mathbf{0}_{3\times3} & \mathbf{0}_{3\times2} & \mathbf{0}_{3\times6} & \mathbf{0}_{3\times2} & \mathbf{Q}_{a_k} & \mathbf{0}_{3\times6} \\ \mathbf{0}_{6\times6} & \mathbf{0}_{6\times3} & \mathbf{0}_{6\times2} & \mathbf{0}_{6\times6} & \mathbf{0}_{6\times2} & \mathbf{0}_{6\times3} & \mathbf{Q}_{\xi_{\rho_k}} \end{bmatrix}$$

where the covariance matrix corresponding to the accelerometer bias $\mathbf{Q}_{a_k}$ is given by Equation 5.35. The covariance matrix corresponding to the pseudorange error states $\mathbf{Q}_{\xi_{\rho_k}}$ is given by Equation 5.62. The process noise covariance matrices $\mathbf{Q}_{c_{pv}}$, $\mathbf{Q}_{c_\theta}$, $\mathbf{Q}_{t_{pv}}$, $\mathbf{Q}_{t/c}$, and $\mathbf{Q}_{c/t}$ are known. The two covariance matrices corresponding to the clock bias and drift of the GPS receiver onboard each vehicle are modeled assuming a second order random walk and coefficients corresponding to a compensated crystal time standard [22]. The discrete version of a second order random walk given in Chapter II for the receiver clock bias is used to propagate the states of the clock bias and drift during the propagation portion of the Kalman filter process.

$$\mathbf{Q}_{s_{bf_k}} = \begin{bmatrix} \frac{h_0}{2}\Delta t + 2h_{-1}\Delta t^2 + \frac{2}{3}\pi^2 h_{-2}\Delta t^3 & h_{-1}\Delta t + \pi^2 h_{-2}\Delta t^2 \\ h_{-1}\Delta t + \pi^2 h_{-2}\Delta t^2 & \frac{h_0}{2\Delta t} + 4h_{-1} + \frac{8}{3}\pi^2 h_{-2}\Delta t \end{bmatrix}$$

where the subscript s denotes vehicle and the coefficients $h_\#$ are defined as

$$\begin{aligned} h_0 &: 2\times10^{-19}\ (s^2) \\ h_{-1} &: 7\times10^{-21}\ (s) \\ h_{-2} &: 2\times10^{-20} \end{aligned}$$

For instances when less than six satellites are visible, the row and column of the estimation error covariance matrix corresponding to the common pseudorange error of the missing satellite are zeroed out and the steady state variance of the common pseudorange error is placed in the diagonal. For example, if the fifth and sixth satellites are missing, the 27th and 28th row and column on the estimation error covariance matrix are set to zero and the diagonal term of each is set to 36 square meters. The estimation error covariance matrix and estimated pseudorange error state are also restructured every time new satellites are acquired, lost or both. If a new satellite comes into view, the corresponding row and column of the estimation error covariance matrix and estimated pseudorange error state are zeroed out and the diagonal of the estimation error covariance matrix replace with the variance of common pseudorange error. The portions of the state vector and covariance matrix are set to zero since each satellite has a unique pseudorange error.

The pseudorange error not accounted for by the common pseudorange error is modeled as a white sequence with covariance matrix, $\mathbf{R}_k$, given as follows.

$$\begin{aligned} \mathbf{R}_{k_c} &= 15 \cdot \mathbf{I}_{n\times n} \ m^2 \\ \mathbf{R}_{k_t} &= 30 \cdot \mathbf{I}_{n\times n} \ m^2 \end{aligned}$$

The variance of the uncommon pseudorange error is 15 square meters for the chaser and 30 square meters for the target due to the remaining error in the total pseudorange error not accounted for by the 6 meter estimated common pseudorange error. Sequential processing of the pseudorange measurements is used therefore the measurement covariance matrix is scalar. The measurement sensitivity matrices are given by Equation 5.63-5.66.

$$\mathbf{H}_{k_c} = \left[\frac{\hat{\mathbf{r}}_c}{\rho_c(\hat{\mathbf{r}}_c)} \;\; \mathbf{0}_{1\times 6} \;\; 1 \;\; \mathbf{0}_{1\times 18} \right] \tag{5.63}$$

$$\mathbf{H}_{k_c}(i+22) = 1 \tag{5.64}$$

$$\mathbf{H}_{k_t} = \left[\mathbf{0}_{1\times 11} \;\; \frac{\hat{\mathbf{r}}_t}{\rho_c(\hat{\mathbf{r}}_t)} \;\; \mathbf{0}_{1\times 3} \;\; 1 \;\; \mathbf{0}_{1\times 10} \right] \tag{5.65}$$

$$\mathbf{H}_{k_t}(i+22) = 1 \tag{5.66}$$

where i is the current pseudorange measurement being processed. With the covariance matrices and measurement sensitivity matrix defined, the states are estimated over the entire duration of the rendezvous. The estimation errors of the position and velocity of both vehicles are found in the same manner as defined for the PV filter in section C. The relative estimation errors are determined using Equation 5.60. Equations 5.67 and 5.68 are used to determine the errors in the estimated clock bias and clock drift compared to the true state values.

$$\mathbf{e}_{p_s} = \mathbf{b}_s - \hat{\mathbf{b}}_s \tag{5.67}$$

$$\mathbf{e}_{v_s} = \mathbf{f}_s - \hat{\mathbf{f}}_s \tag{5.68}$$

The subscript s refers to which spacecraft.

F. Reduced Pseudorange Kalman Filter

The derivation of a reduced pseudorange (GPS) EKF is addressed in this section. Frequently in addition to position, velocity, clock bias and clock drift states, other states are included in a GPS EKF as is the case in Section E. By choosing to

not estimate states in the GPS EKF, the reduced GPS EKF is formed reducing the complexity of both the state model as well as the Kalman filter at little cost in the means of filter performance. Although the common pseudorange error states are no longer estimated, the states are still considered. The effects of the common pseudorange error states on the other states are considered but not compensated for. As a result, the reduced GPS EKF is slightly more conservative in state estimation compared to the GPS EKF. In addition, bookkeeping is no longer performed. The bookkeeping can be omitted since the common pseudorange error states are no longer being estimated. If the states were still being estimated, bookkeeping must still be performed otherwise the filter would fail. By removing the bookkeeping from the reduced GPS filter, more conservatism is also added to the state estimation errors.

The state vector used for the reduced GPS EKF is comprised of chaser position and velocity, target position and velocity, chaser attitude parameters, accelerometer bias, common pseudorange errors unique to each GPS satellite, and clock bias and drift of both GPS receivers (one onboard the chaser and one onboard the target). Although the pseudorange errors are included in the state vector, the reduced GPS EKF does not estimate the states. Instead, the states are set to zero while the process noise covariance and state transition matrix entries corresponding to the additional states are allowed to evolve with time. By allowing the process noise covariance and state transition matrices to evolve with time, the entries corresponding to the pseudorange error in the estimation error covariance matrix also evolve with time affecting the estimation of the states being estimated. The measurement vector consists of pseudoranges from no more than six satellites per receiver. The number of pseudorange measurements available during every update process will vary depending upon the number of GPS satellites in view of the receiver. The state and measurement vectors are as follows.

$$\begin{aligned}
\mathbf{x} &= \begin{bmatrix}\mathbf{r}_c^T & \mathbf{v}_c^T & \boldsymbol{\theta}^T & b_c & f_c & \mathbf{r}_t^T & \mathbf{v}_t^T & b_t & f_t & \mathbf{a}_b^T & \boldsymbol{\xi}_{gps}^T\end{bmatrix}^T \\
\widetilde{\mathbf{y}} &= \begin{bmatrix}\rho_{c_1} & \rho_{c_2} \cdots & \rho_{c_n} & \rho_{t_1} & \rho_{t_2} & \cdots & \rho_{t_n}\end{bmatrix}^T
\end{aligned}$$

The subscript n denotes the n^{th} and final visible satellite. The maximum values for n is six at any given time. If more than six GPS satellites are in view at any time, the GPS satellites corresponding to the first six signals received are used. The state and measurement models used are the same as given in Section A.

Unlike to the PV filter, the state and measurement models both experience corruption in the states or measurements due to the presence of white noise. Using the definition of the state model in Equation 5.1, the zero mean white process noise has a spectral density $\mathbf{Q}(t)$. However, the discrete propagation of the estimation error matrix is used therefore the covariance matrix corresponding to the zero mean white process noise is needed. The covariance matrix corresponding to the discrete version of the zero mean white process noise, $\mathbf{Q}_k$, is found using Equation 5.14 and is the same as given for the full state GPS EKF.

The measurement covariance matrix, $\mathbf{R}_k$, is given by the following equation.

$$\mathbf{R}_k = \sigma_{\rho_{ss}}^2 \mathbf{I}_{n\times n} \tag{5.69}$$

The scalar value for $\mathbf{R}_k$ conveys the use of sequential processing of the measurements. The steady state standard deviation, $\sigma_{\rho_{ss}}$, is 5 meters. In a similar manner as is performed for the relative pseudorange relative deltarange EKF, a single measurement is processed at a time updating the covariance with each processed measurement and adding error corrections to the state error correction vector.

Since there are pseudorange measurements for both the chaser and target vehi-

cles, the sensitivity matrix $\mathbf{H}_k$ will differ depending upon the pseudorange measurement being processed. The sensitivity matrix corresponding to measured pseudoranges from the chaser vehicle is given by Equations 5.63-5.64 while Equations 5.65-5.66 give the sensitivity matrix for pseudorange measurements from the target. The sensitivity matrices are found by taking the derivative of the pseudorange corresponding to a vehicle with respect to the state vector. With the sensitivity matrices defined, the EKF process defined in Section A is implemented and an estimation of the states over the duration of the rendezvous operation is determined. The position and velocity estimation errors are found using Equations 5.36-5.38 while Equations 5.67-5.68 are used to calculate the estimation errors in the clock bias and drift.

CHAPTER VI

RESULTS AND COMPARISONS

The results for the four Kalman filters are presented in this chapter. For the following results, 100 Monte Carlo runs are performed. Each filter experiences the same error for a given Monte Carlo simulation. The estimation errors of the inertial position and velocity of both vehicles as well as the relative position and velocity are presented. The sample standard deviation is determined and presented alongside the predicted standard deviation of all 100 Monte Carlo runs. The sample standard deviation of the four filters are compared with advantages and disadvantages of each filter determined. The relative trajectory over which the rendezvous operation is performed is given.

A. Results

1. Proximity Operations Trajectory

For the current study, GPS navigation is implemented during the rendezvous of a chaser vehicle with a target vehicle. The range over which GPS navigation is implemented is from 23 kilometers to 500 meters. The true trajectory used for this study is generated off-line and includes information about the position, velocity, attitude and angular velocity of each vehicle. The nonimal trajectory consists of two altitude adjust maneuvers. Over the course of the rendezvous, four primary burns are triggered to initiate and end each of the altitude adjustments. The first burn initiates the altitude adjust with the second burn ending the adjustment. The vehicle coasts and gains ground on the target vehicle from behind before approach initiation occurs with the third burn. The fourth burn occurs when the chaser vehicle is radially underneath at a distance of approximately 500 meters at which point GPS navigation

is deactivated.

The estimation errors resulting from the 100 Monte Carlo runs are plotted against their respective 3σ predicted standard deviations of all 100 runs. In order to determine the overall performance of the four filter, the sample standard deviations derived from the 100 estimation errors are computed using Equation 6.1 and compared to the 1σ predicted standard deviations from the Monte Carlo simulation.

$$\mathbf{S}_{sam_j} = \sqrt{\frac{1}{n}\sum_{i=1}^{100}(\mathbf{e}_i)^2} \quad \text{for } j = 1, ..., N \tag{6.1}$$

The total number of estimation errors for one Monte Carlo run is denoted by N. For a properly tuned filter, the estimation error should closely follow the 1σ predicted standard deviation over the entire simulation.

2. Position-Velocity Extended Kalman Filter

The following results pertain to 100 Monte Carlo simulation of a single trajectory of both the target vehicle and chaser vehicle. Measurement rejection is based upon satellite visibility and geometry, determined by the position delusion of precision (PDOP). PDOP is calculated using Equation 6.3. For the current case of study, any measurement of PDOP > 8 is rejected.

$$\mathbf{G_{dop}} = (\mathbf{H_{dop}}^T\mathbf{H_{dop}})^{-1} \tag{6.2}$$

$$PDOP = \sqrt{trace(\mathbf{G_{dop}}(\mathbf{1:3}, \mathbf{1:3}))} \tag{6.3}$$

where $\mathbf{G_{dop}}$ is the design matrix and is defined as follows. Note the subscript n refers to the n^{th} pseudorange measurement and the last column is the derivative of the pseudorange with respect to the clock bias.

$$\mathbf{G_{dop}} = \begin{bmatrix} \frac{d\rho_1}{dx} & \frac{d\rho_1}{dy} & \frac{d\rho_1}{dz} & 1 \\ \vdots & \vdots & \vdots & \vdots \\ \frac{d\rho_n}{dx} & \frac{d\rho_n}{dy} & \frac{d\rho_n}{dz} & 1 \end{bmatrix}$$

Figure 20 gives the position estimation errors of 100 Monte Carlo runs with the corresponding 3σ predicted standard deviation for the chaser vehicle. Figure 21 gives the position estimation errors of the target vehicle for 100 Monte Carlo runs with the 3σ predicted standard deviation of all 100 Monte Carlo runs. The growth of the predicted standard deviation relates to one of two things, inadequate satellite visibility or poor geometry. As previously mentioned, in order for the GPS sensor to compute an approximate position and velocity at least four GPS satellites must be visible at any given time. When the number of visible satellites decreases to less than four or a PDOP value of greater than eight is calculated, the current measurement is rejected and only the estimated state is propagated. There is a single case that does not lie within the 3σ predicted standard deviations in Figure 21. The occurrence of a single violation is expected over 100 runs with the measurements corrupted by colored noise and is therefore of no major concern. In addition, the error violates the predicted standard deviations by a few meters, a relatively small violation based on the size of the predicted standard deviations.

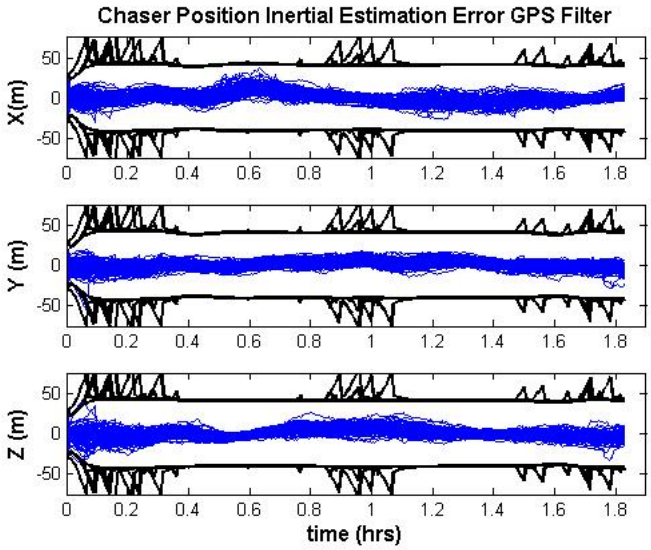

Fig. 20. Chaser Inertial Position Estimation Error - PV EKF

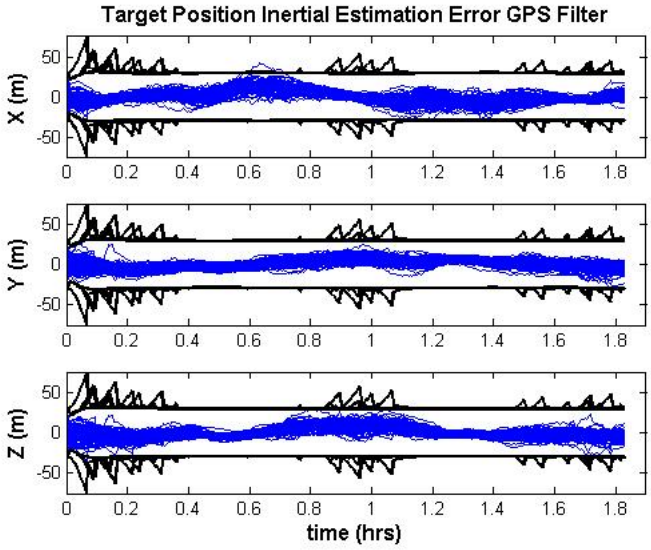

Fig. 21. Target Inertial Position Estimation Error - PV EKF

Figures 22-23 correspond to the velocity estimation errors of the chaser and target vehicles respectively for 100 Monte Carlo runs with the 3σ predicted standard

deviation of each run. As for the velocity of the target vehicle, Figure 23 shows the estimation error remaining within the predicted standard deviations of all 100 runs. Once again, any growth in the predicted standard deviations is due to propagation only of the estimated state resulting from measurement rejection. Since only a single trajectory is being used, the errors are similar for all 100 runs due to the process noise being the essentially the same for every run performed. Using a single trajectory does not allow for the dispersion in the errors which occurs when multiple trajectories are used. As a result of using a single trajectory, the dynamics are visible in Figure 20-23.

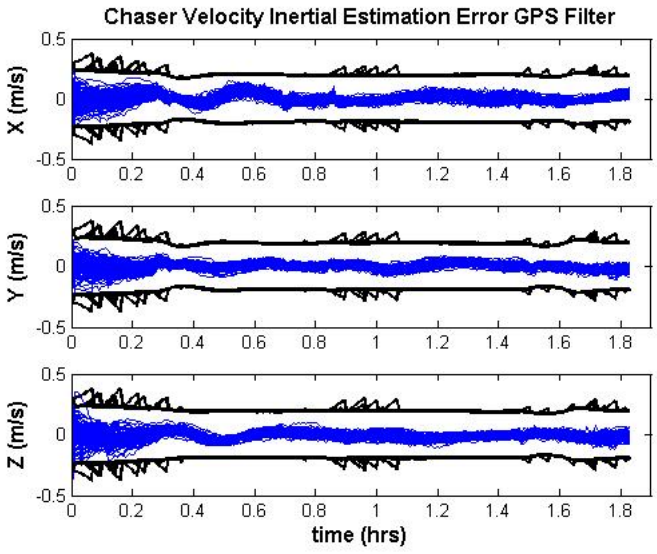

Fig. 22. Chaser Inertial Velocity Estimation Error - PV EKF

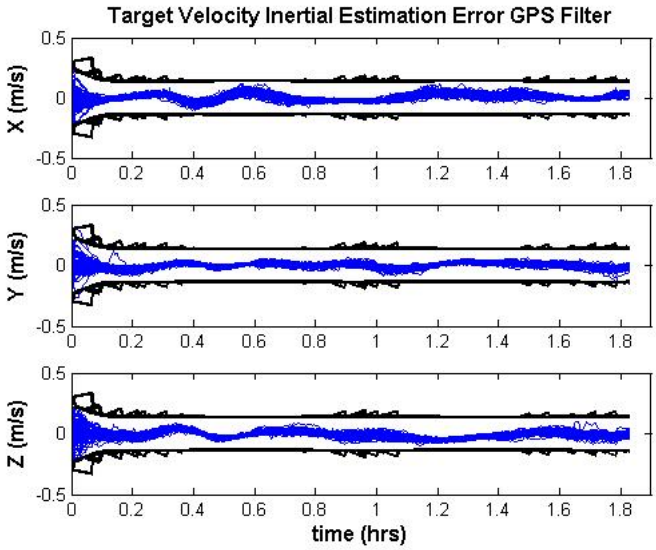

Fig. 23. Target Inertial Velocity Estimation Error - PV EKF

Figure 24 is the estimation error in the relative position between the chaser and target vehicles while Figure 25 is the estimation error in the relative velocity between both vehicles, each representing 100 Monte Carlo runs. The relative position estimation error is computed by calculating the difference between the position estimation error of chaser vehicle and that of the target vehicle. The relative velocity estimation error is computed in the same fashion. The covariance of the relative position and velocity estimation error is calculated based on the covariance of the position and velocity of the two vehicles throughout the simulation as shown in Equation 6.4.

$$\mathbf{P}_{rel} = \mathbf{P}_c + \mathbf{P}_t - \mathbf{P}_{t/c} - \mathbf{P}_{c/t} \tag{6.4}$$

where $\mathbf{P}$ is the estimation error covariance. The estimation error covariance matrix can be divided as follows assuming 12 states, the first 6 corresponding to the position and velocity of the chaser and the final 6 corresponding to the target's position and

velocity.

$$\mathbf{P} = \begin{bmatrix} \mathbf{P}_c & \mathbf{P}_{c/t} \\ \mathbf{P}_{t/c} & \mathbf{P}_t \end{bmatrix}$$

The subscript t/c refers to the correlation of the estimation errors between the target and chaser vehicles and vice versa for the subscript c/t.

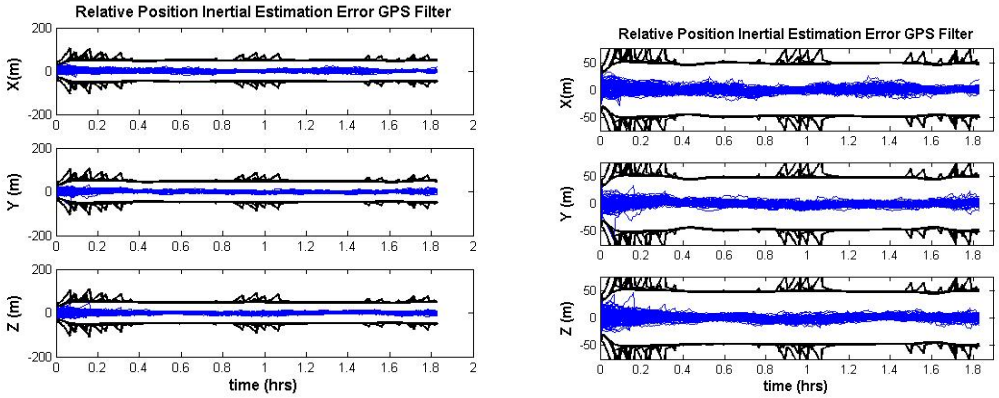

(a) Nominal (b) Zoomed

Fig. 24. Relative Position Estimation Error - PV EKF

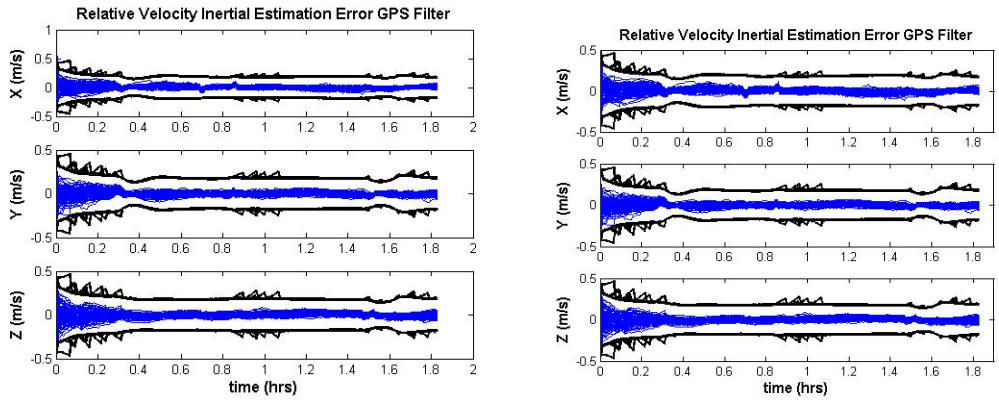

(a) Nominal (b) Zoomed

Fig. 25. Relative Velocity Estimation Error - PV EKF

In order to determine the performance of the PV EKF, the sample standard deviation for each state is compared to the 1σ predicted standard deviations of the respective state. Figure 26 gives the sample standard deviations pertaining to the chaser position and velocity for all 100 Monte Carlo simulations plotted against the 100 predicted standard deviations. The sample standard deviation of the position is frequently smaller than the 100 predicted standard deviations. The sample standard deviation of the velocity matches the predicted standard deviations for the first 0.3 hours before shrinking less than 100 predicted standard deviations. The sample standard deviation is higher over the first portion due to the lag in the accelerometer bias estimate. As a result, there is an increase in the uncertainty of the estimation errors resulting in an increased sample standard deviation.

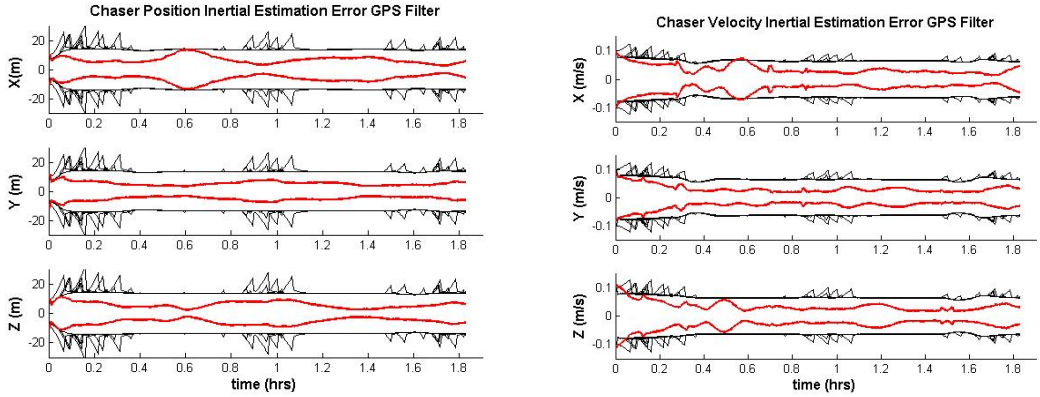

(a) Position (b) Velocity

Fig. 26. Chaser Position and Velocity Sample Standard Deviation - PV EKF

Figure 27(a) shows the sample standard deviation of all 100 Monte Carlo estimation errors for the inertial position of the target vehicle. Figure 27(b) conveys the sample standard deviation of the estimation errors for the inertial velocity of the

target vehicle for all 100 Monte Carlo simulations. The predicted standard deviations are slightly smaller compared to the predicted standard deviations of the chaser vehicle. The dynamics are visible in both the position and velocity. The lag in the accelerometer bias estimate does not affect the velocity estimate of the target vehicle as it does the chaser vehicle.

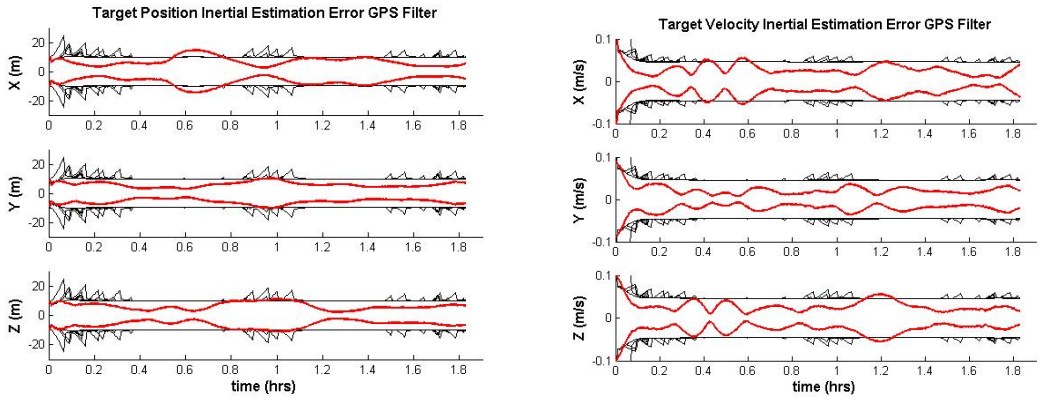

(a) Position (b) Velocity

Fig. 27. Target Position and Velocity Sample Standard Deviation - PV EKF

In Figures 26-27, there are multiple instances where the sample standard deviation is much small than the predicted 1σ standard deviations in one direction but in another direction the sample standard deviation matches the predicted standard deviation. This is due to inability of the PV filter to determine error directionality and is also attributed to the use of a single trajectory.

Figures 28-29 correspond to the sample standard deviation of all 100 estimation errors for relative position and velocity plotted against all 100 1σ predicted standard deviations. The sample standard deviation for both the relative position and velocity lie along the predicted standard deviations for all 100 Monte Carlo runs.

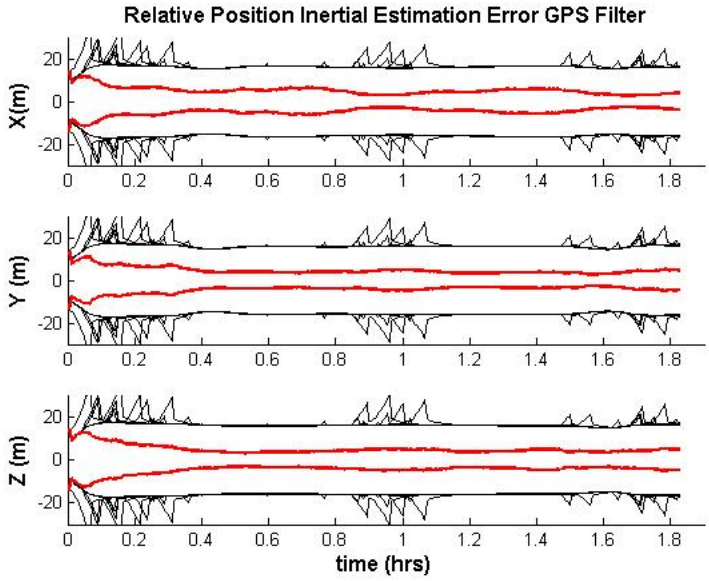

Fig. 28. Relative Position Sample Standard Deviation - PV EKF

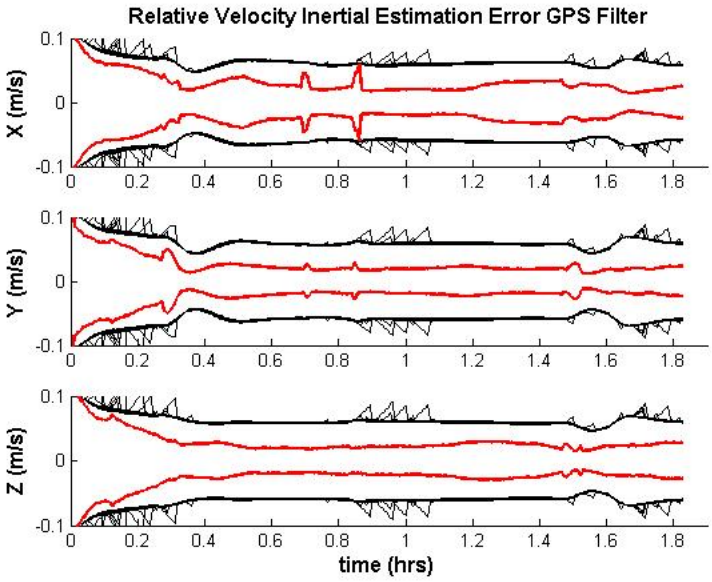

Fig. 29. Relative Velocity Sample Standard Deviation - PV EKF

The growths in the sample standard deviation correspond to thruster firings that

influence all of the errors in the same manner. Although there are instances in Figures 26-27 when the sample standard deviation does not match the predicted standard deviations, the lack of error directionality explains a number of these instances.

3. Relative Pseudorange Extended Kalman Filter

The RGPS EKF is simulated for 100 Monte Carlo runs and the results analyzed in the following section. A dual inertial state filter is used with the relative pseudorange measurement processed. Although there are multiple approaches to the design and implementation of relative GPS filters, the dual inertial state filter is used for consistency between the four filters being compared. Both the inertial position and velocity of each vehicle along with the relative position and velocity between the two vehicles is presented. The predicted standard deviations are 3σ standard deviations for the time history of all 100 estimation errors and 1σ standard deviations for the time history comparison of the sample standard deviation.

Figure 30(a) gives the estimation errors of the position of the chaser vehicle for all Monte Carlo runs. The figure also gives the predicted standard deviation for all Monte Carlo runs. Figure 30(b) shows the estimation error for the position of the target for all the Monte Carlo runs in addition to the predicted standard deviations. Since the RGPS filter processes relative measurements, the performance in estimating the position of each vehicle diminishes as can be seen by the substantial growth of the errors and corresponding predicted standard deviations as time progresses.

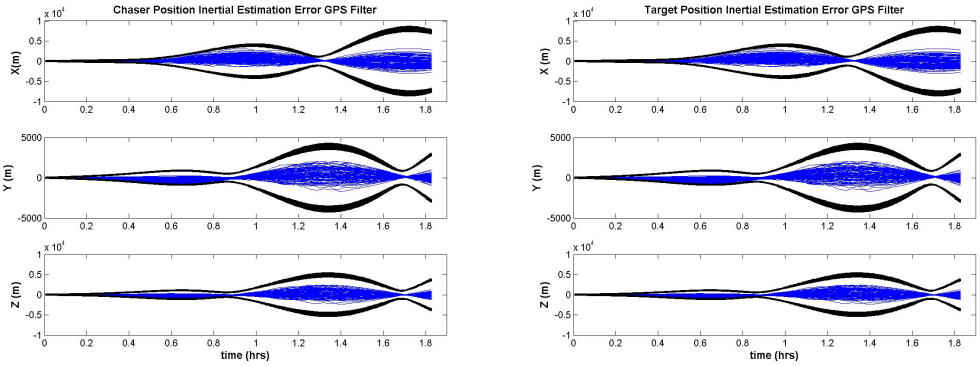

(a) Chaser (b) Target

Fig. 30. Inertial Position Estimation Error - RGPS EKF

Figure 31 shows the estimation errors and corresponding predicted standard deviations of the chaser and target velocities. Similar to the position estimation errors, the velocity estimation errors and covariances for each vehicle progressively grow throughout time. As aforementioned, since relative measurements are being processed, the RGPS filter ensures the relative position and velocity between the two vehicles remain low while the inertial position and velocity errors grow with time.

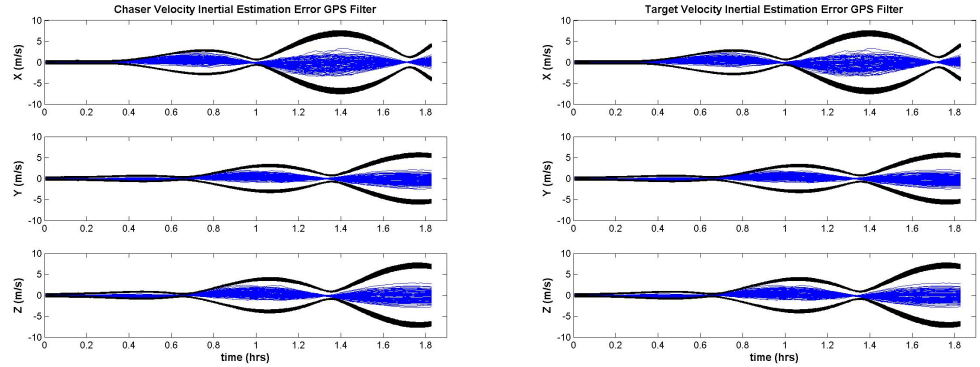

(a) Chaser (b) Target

Fig. 31. Inertial Velocity Estimation Error - RGPS EKF

The relative position estimation errors and error covariances are given by Figure 32. Although there appears to be many instances when the error estimates do not match the predicted predicted standard deviations, the majority of the errors remain within the corresponding predicted predicted standard deviation for each respective run. There are two instances where the estimation error ventures past the corresponding 3σ predicted standard deviation. This is a result of poor geometry in addition to a low number of visible satellites. While the estimation errors do grow past the covariance, the estimation errors are on the order of less than a meter outside of the covariance and is expected over the course of 100 Monte Carlo runs.

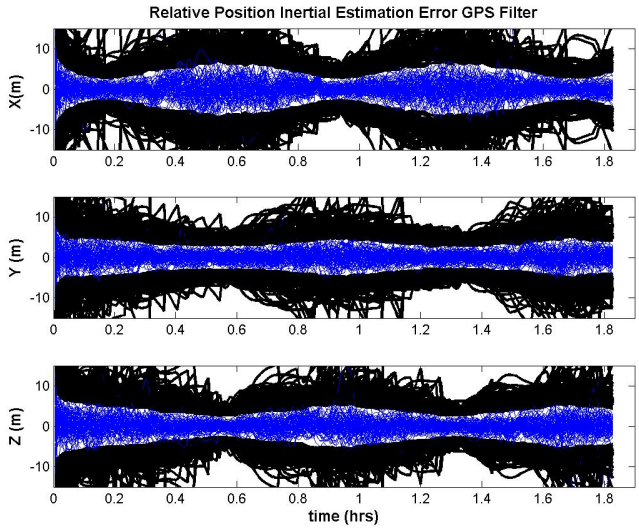

Fig. 32. Relative Position Estimation Error - RGPS EKF

The relative velocity estimation errors and covariances are shown in Figure 33. Contrary to the relative position errors, the relative velocity estimation errors remain within the predicted standard deviations. The jumps in the estimation errors correspond to thruster firings performed by the chaser vehicle.

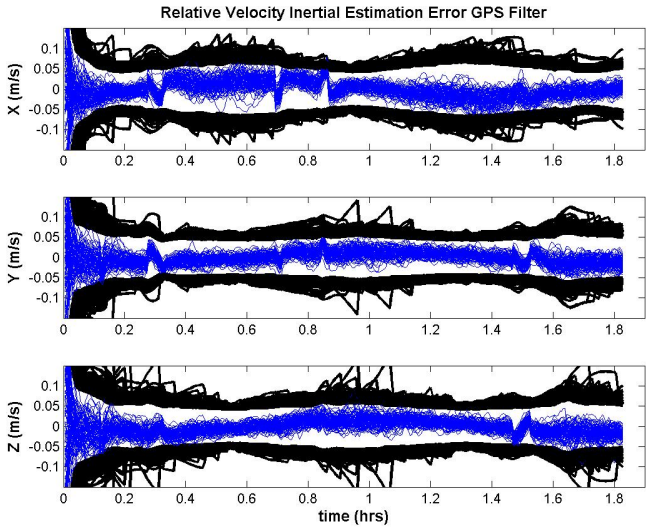

Fig. 33. Relative Velocity Estimation Error - RGPS EKF

The increase and decrease of the predicted standard deviations with the estimation error in Figures 32-33 relay the ability of the RGPS filter to determine the direction in which the error is present. As a result, the predicted standard deviations more accurately predict the actual estimation errors for the relative states.

Sample covariance plots corresponding to the inertial position and velocity estimation errors are omitted. It is evident how the sample standard deviations will evolve with time by inspection of Figures 30-31. Figure 34 and Figure 35 gives the sample standard deviation of the relative position and velocity plotted against all 100 Monte Carlo predicted standard deviations. The sample standard deviation lies among the 100 predicted standard deviations. Figure 35 shows the sample standard deviation pertaining to the relative velocity estimation errors remaining within nearly all 100 Monte Carlo simulation. The sample standard deviation again lies along the 100 predicted standard deviations with the exception of the growths in the sample standard deviations. The spikes in the velocity sample standard deviation are due to

the thruster firings which affect the velocity state estimation of all 100 Monte Carlo runs the same.

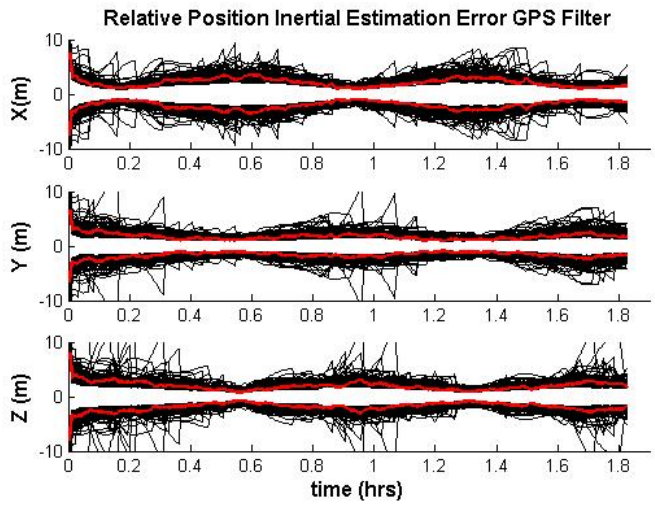

Fig. 34. Relative Position Sample Standard Deviation - RGPS EKF

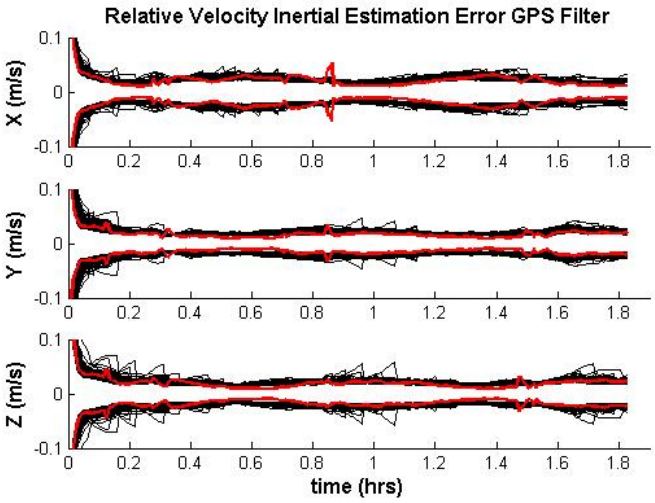

Fig. 35. Relative Velocity Sample Standard Deviation - RGPS EKF

While the RGPS EKF has the disadvantage of not being capable of estimating the

inertial position and velocity, it does have the advantage of performing exceptionally well with respect to relative state estimation. The filter also allows for more accurate prediction of the estimation errors since it is capable to determine the magnitude of the error in each direction. The RGPS EKF processes non-linear measurements resulting in a slightly more complex architecture than the PV EKF.

4. Psuedorange Extended Kalman Filter

The time history of 100 estimation errors as well as the sample standard deviation determined from the 100 estimation errors is presented in the following section for the GPS EKF. The GPS EKF has the advantage of performing well in both inertial state and relative state estimation. The 3σ predicted standard deviations are plotted against the 100 estimation errors while the sample standard deviations are plotted against the 1σ predicted standard deviation. Common satellites are processed first followed by satellites uniquely visible to each vehicle until 6 total satellites have been processed. Since the pseudorange error is unique to each GPS satellite, the predicted standard deviation changes when the visible satellites change.

Figure 36 gives the inertial position estimation error of the chaser for all 100 Monte Carlo runs and Figure 37 gives the inertial estimation errors corresponding to the position of the target vehicle. As is the case for the PV filter, the dynamics of the system are visible over the course of the rendezvous in the position of both vehicles. This is attributed to only a single reference trajectory being used during the Monte Carlo runs. Comparing the X direction with the Y and Z directions, it is evident that the GPS EKF allows for more accurate predictions of the estimation error since the predicted standard deviations of all three grow and decrease differently. The growth in the predicted standard deviation is contributed to poor geometry, lack of satellite visibility or a combination of both.

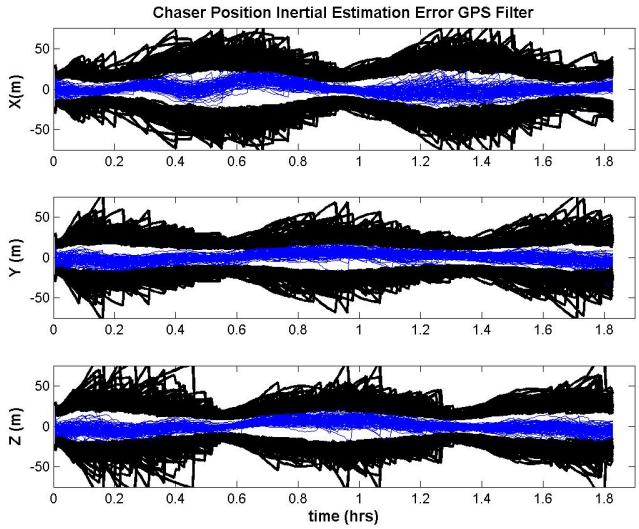

Fig. 36. Chaser Inertial Position Estimation Error - GPS EKF

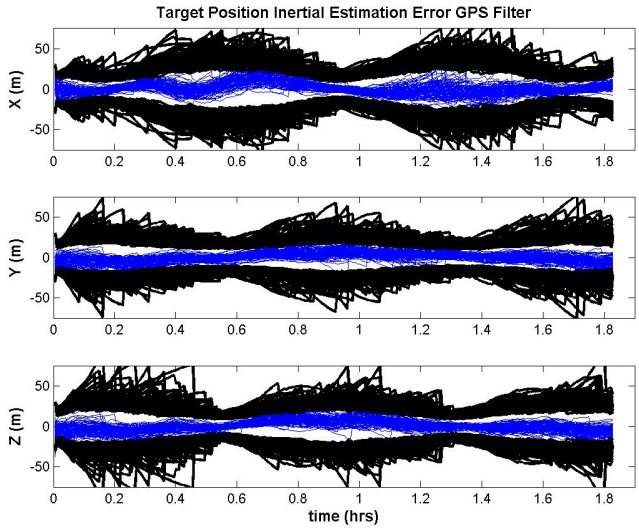

Fig. 37. Target Inertial Position Estimation Error - GPS EKF

The time history of all 100 velocity estimation errors is given by Figures 38-39. The covariance grows and shrinks with the increase and decrease in the estimation

errors. The estimation errors remain within the predicted standard deviations for all 100 Monte Carlo runs.

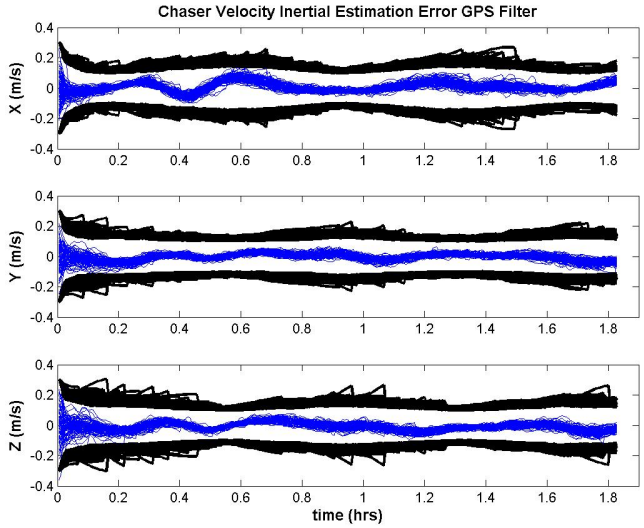

Fig. 38. Chaser Inertial Velocity Estimation Error - GPS EKF

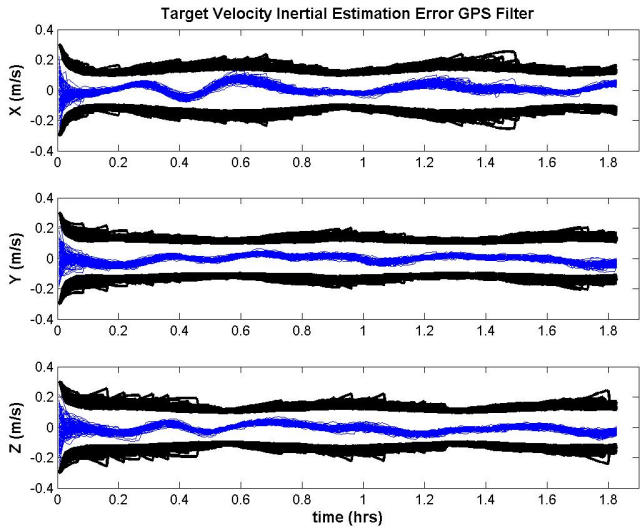

Fig. 39. Target Inertial Velocity Estimation Error - GPS EKF

The relative position estimation error is given by Figure 40. Although it appears there are numerous cases that venture outside of the covariance, the estimation error for all but two cases remain within their predicted covariance. The two instances that go outside the covariance venture less than a meter outside and return within the covariance rather quickly.

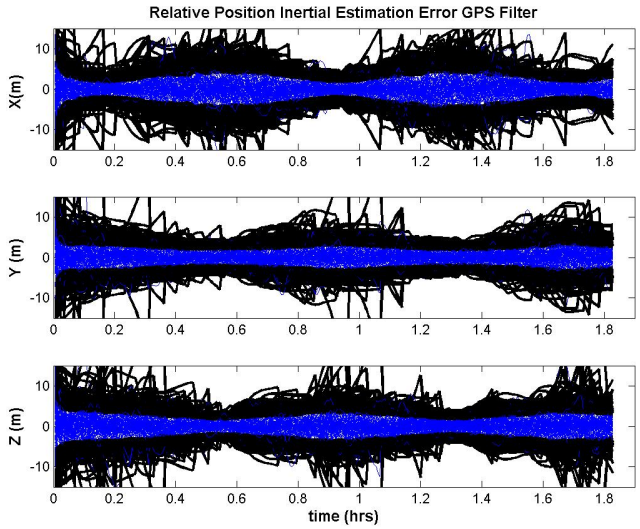

Fig. 40. Relative Position Estimation Error - GPS EKF

Figure 41 shows the estimation errors corresponding to 100 Monte Carlo runs. The relative velocity errors remain within the 3σ covariances for all 100 runs.

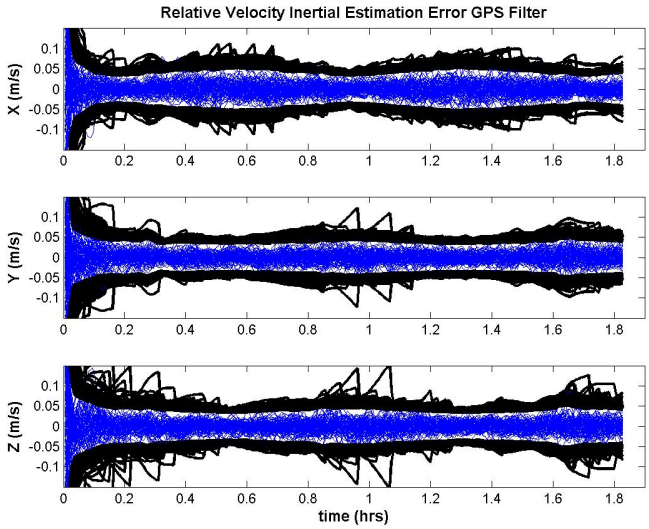

Fig. 41. Relative Velocity Estimation Error - GPS EKF

In order to examine the performance of the GPS EKF, the sample standard deviation of each estimation error is determine and plotted against the 100 1σ predicted standard deviations. Figures 42-43 give the position and velocity sample standard deviations for the chaser vehicle and target vehicle respectively. As is the case in the PV filter, the sample standard deviation corresponding to the chaser velocity closely matches the predicted standard deviation for the first 0.3 hours. This is attributed to the lag in the estimation of the accelerometer bias. The sample standard deviation for each inertial state consistently lies along the 100 covariances. The velocity sample standard deviations are occasionally less than the 100 predicted standard deviations which is attributed to the repeatability of the estimation error due to the presence of a single trajectory.

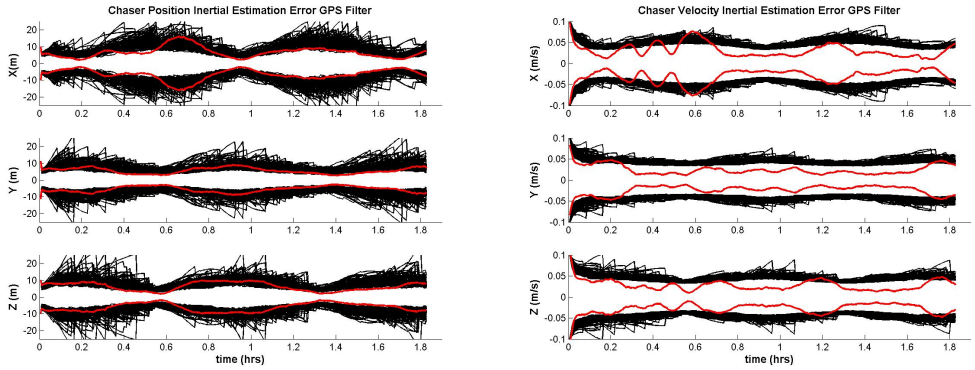

(a) Position (b) Velocity

Fig. 42. Chaser Position and Velocity Sample Standard Deviation - GPS EKF

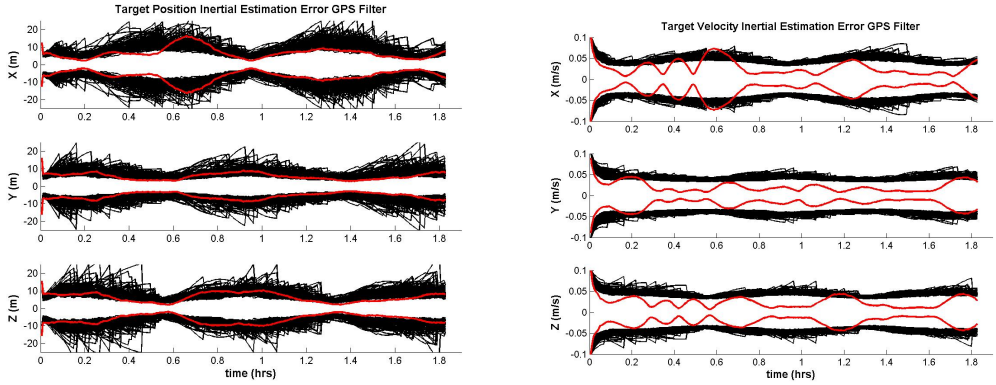

(a) Position (b) Velocity

Fig. 43. Target Position and Velocity Sample Standard Deviation - GPS EKF

The sample standard deviation of both the relative position and velocity estimation errors are given in Figure 44 and Figure 45. The sample standard deviation of each lies along the 100 predicted standard deviations. Since only 100 Monte Carlo runs are considered, it is easy to see a correlation between substantially larger predicted standard deviations and growths in the sample standard deviation.

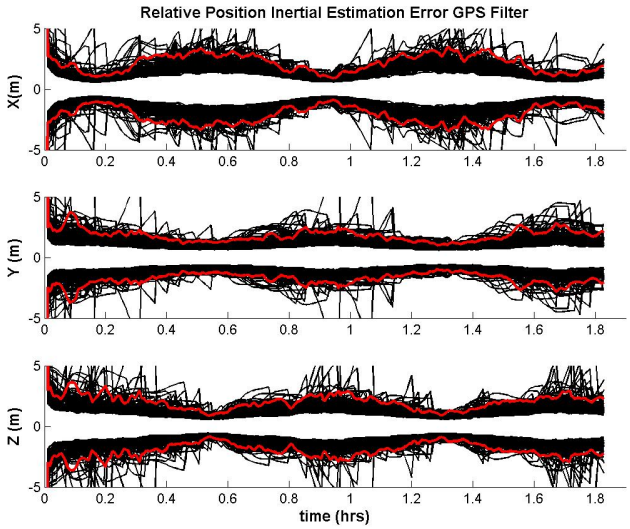

Fig. 44. Relative Position Sample Standard Deviation - GPS EKF

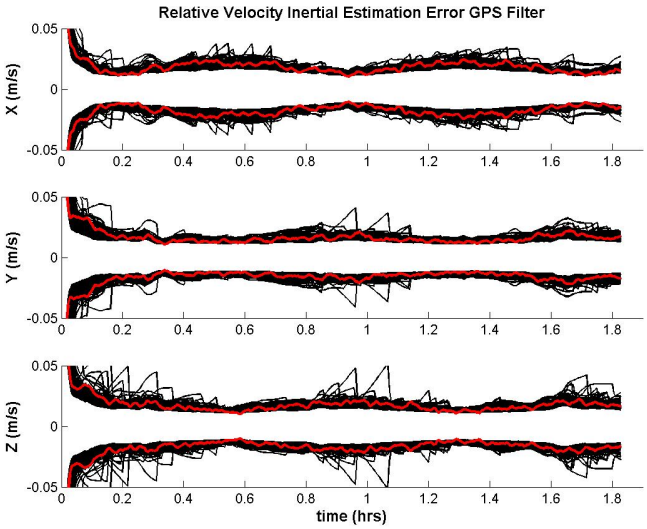

Fig. 45. Relative Velocity Sample Standard Deviation - GPS EKF

The GPS EKF performs well in inertial state estimation and maintains a low error in the relative distance and velocity between the two vehicles.

5. Reduced Pseudorange Extended Kalman Filter

The results from 100 Monte Carlo runs for the reduced GPS filter is presented in the following section. Inertial position and velocity estimation errors of each vehicle in addition to relative position and velocity estimation errors are analyzed. All 100 Monte Carlo estimation errors as well as the sample standard deviations of the relative states are presented. The estimation errors are presented with 3σ predicted standard deviations while the sample standard deviations are presented with 1σ predicted standard deviations. The reduced GPS EKF no longer estimates additional states corresponding to common pseudorange errors but does keep the states in the state vector. As a result, there are correlation terms in the predicted standard deviation between the common pseudorange error states and the remaining states that are allowed to evolve with time. Therefore, the covariances in the following section include affects resulting from the common pseudorange error states not estimated.

Figure 46 shows the inertial estimation errors for the position of the chaser vehicle for all 100 Monte Carlo runs with the corresponding 3σ covariances. Figure 47 gives the inertial estimation errors for the position of the target vehicle with the predicted standard deviation of all 100 Monte Carlo runs.

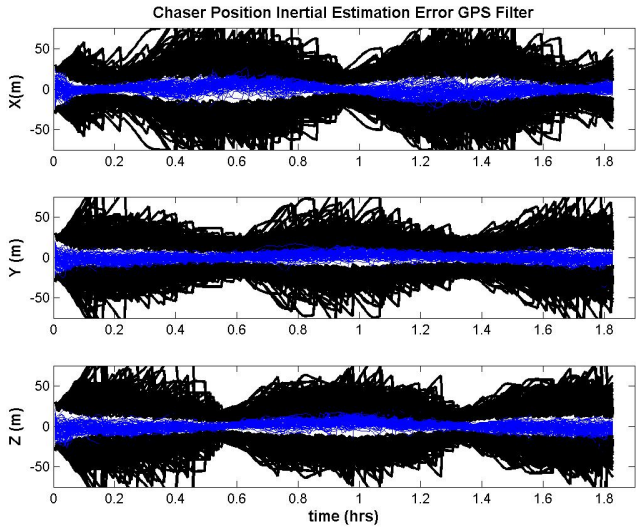

Fig. 46. Chaser Inertial Position Estimation Error - Reduced GPS EKF

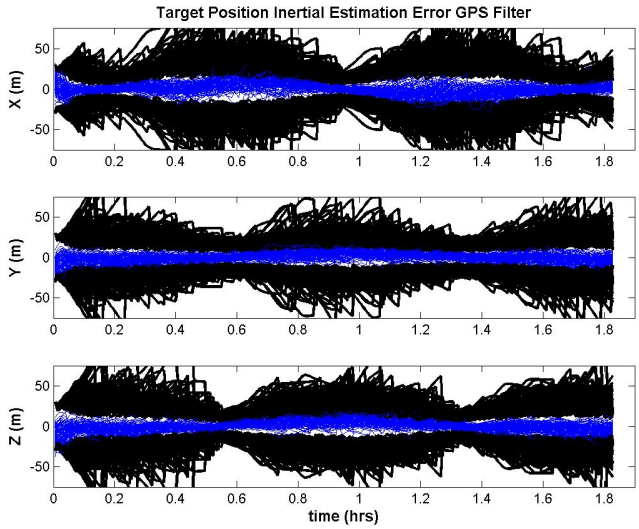

Fig. 47. Target Inertial Position Estimation Error - Reduced GPS EKF

The estimation errors for each vehicle remain within the covariance for all Monte Carlo runs. Increases in the covariance correspond to poor geometry or inadequate

satellite coverage. The GPS filter is equipped with the ability to reject a measurement if the measurement residual is five times greater than the corresponding measurement covariance. The measurement residual is found using Equation 6.5.

$$\Delta y = \widetilde{\mathbf{y}} - \mathbf{h}(\hat{\mathbf{x}}) \tag{6.5}$$

The measurement covariance is given by Equation 6.6.

$$\mathbf{W}_{meas} = \mathbf{H}_k \mathbf{P}_k \mathbf{H}_k + \mathbf{R}_k \tag{6.6}$$

Figures 48-49 give the inertial velocity estimation errors of each vehicle for the 100 Monte Carlo runs. The estimation errors remain within the 3σ predicted standard deviations for both vehicles. Once again, the estimation errors remain withing all 100 Monte Carlo predicted standard deviations.

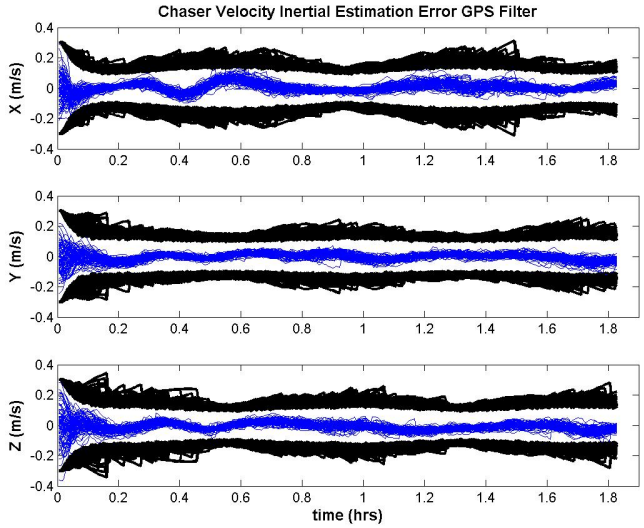

Fig. 48. Chaser Inertial Velocity Estimation Error - Reduced GPS EKF

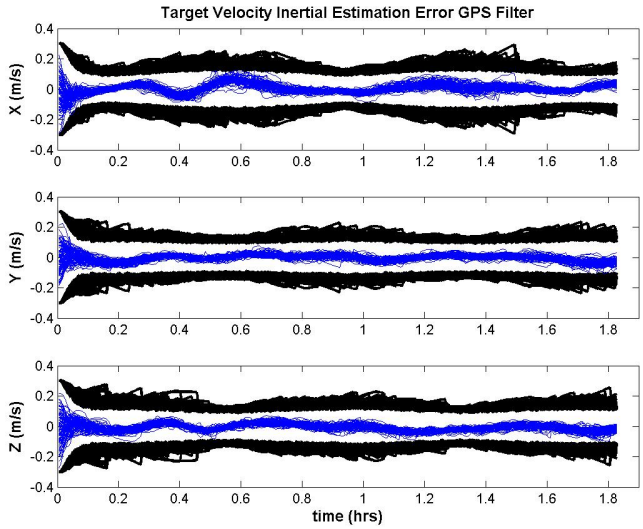

Fig. 49. Target Inertial Velocity Estimation Error - Reduced GPS EKF

Figure 50 shows the estimation errors in the relative position between the two vehicles while Figure 51 gives the estimation error in the relative velocity between the two vehicles, both with respect to the covariance of all 100 Monte Carlo runs. Although it may appear that some of the estimation errors venture outside of the predicted standard deviations in Figure 50, the estimation errors do remain within their respective 3σ covariances except for two instances. During these instances, the estimation errors go beyond the predicted standard deviation by approximately 1 meter which is explained by a sudden loss of satellites resulting in a less accurate state estimation due to less measurements processed. Although the estimation errors do not match the predicted standard deviations at these instances, the presence of the two small outlying estimation errors is acceptable and hence of no major concern.

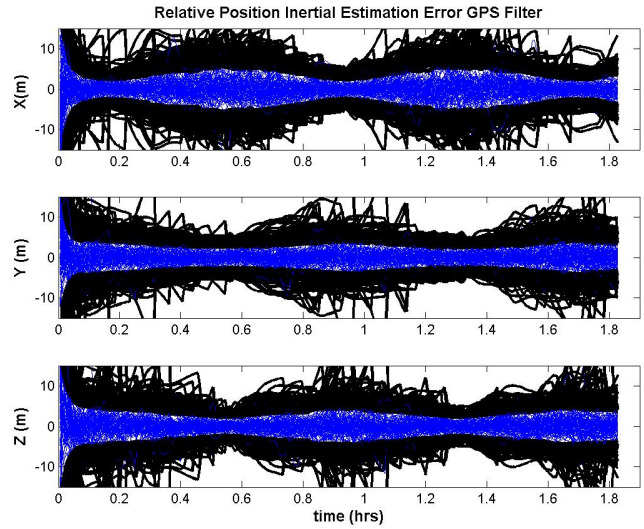

Fig. 50. Relative Position Estimation Error - Reduced GPS EKF

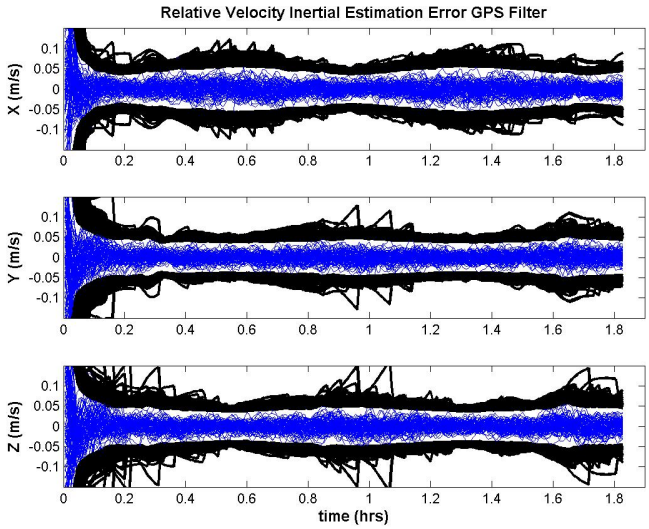

Fig. 51. Relative Velocity Estimation Error - Reduced GPS EKF

Figures 52-53 give the sample standard deviations derived from the 100 estimation errors for the position and velocity of the chaser vehicle and target vehicle respec-

tively. The position sample standard deviation of both vehicles matches the predicted standard deviations for the entire duration when GPS navigation is implemented. The velocity sample standard deviation follows the predicted standard deviations but are slightly smaller than the predicted standard deviations at instances. The chaser velocity sample standard deviation once again follows the predicted standard deviations over the first 0.3 hours due to the lag in the accelerometer bias estimation.

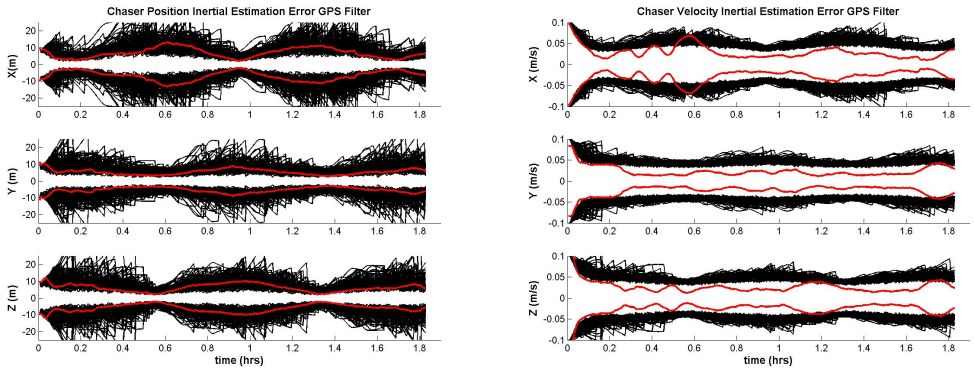

(a) Position (b) Velocity

Fig. 52. Chaser Position and Velocity Sample Standard Deviation - Reduced GPS EKF

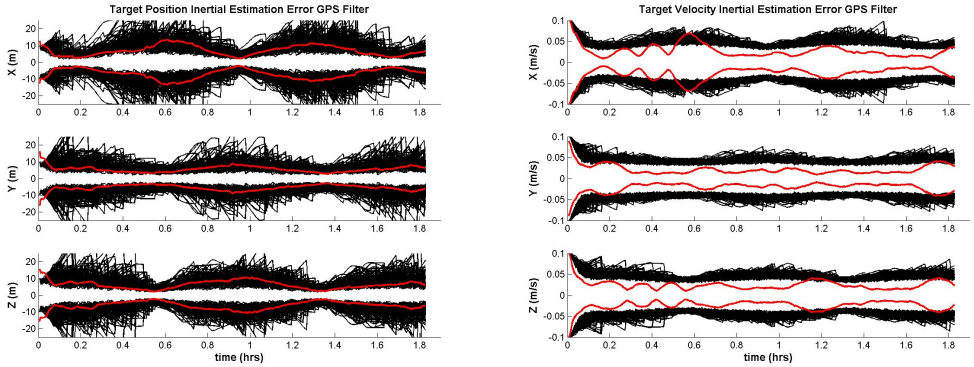

(a) Position (b) Velocity

Fig. 53. Target Position and Velocity Sample Standard Deviation - Reduced GPS EKF

Figures 54-55 give the sample standard deviation corresponding to all 100 estimation errors along with the 1σ predicted predicted standard deviations for all 100 Monte Carlo runs. Upon inspection of Figure 54, the sample standard deviation appears to be larger than a number of predicted predicted standard deviations. The larger sample standard deviations occur around larger predicted predicted standard deviations conveying the accuracy of the estimates corresponding to the elevated predicted standard deviations has diminished. As a result, estimation errors over the interval of increased predicted standard deviations are more likely to be higher hence the sample standard deviation is larger since the sample standard deviation is determined from the estimation errors. On the other hand, the velocity sample standard deviation shown in Figure 55 follow along the inside of all 100 predicted standard deviations after the first 0.2 hours. The sample standard deviation is elevated during 0.2 hour due to randomness in the initial starting velocity of both the chaser and target vehicles therefore resulting in more dispersed estimation errors.

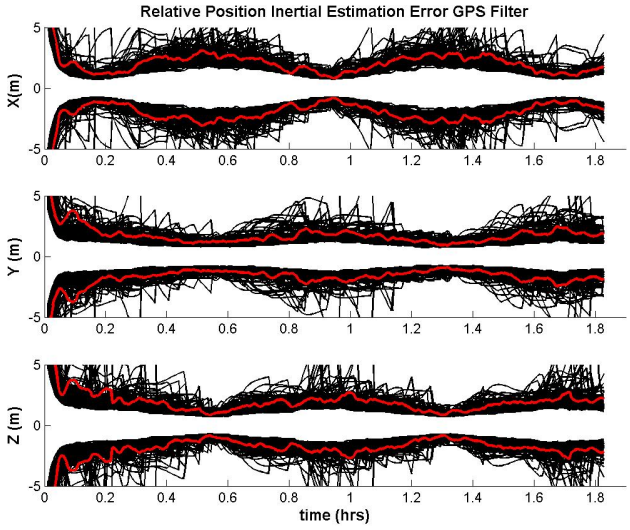

Fig. 54. Relative Position Sample Standard Deviation - Reduced GPS EKF

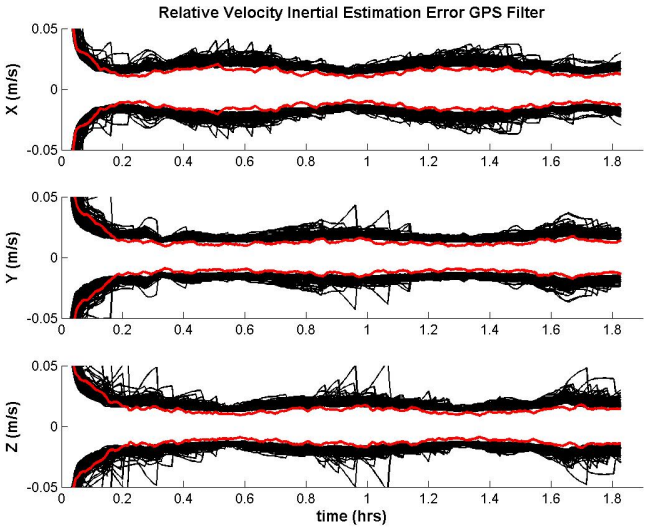

Fig. 55. Relative Velocity Sample Standard Deviation - Reduced GPS EKF

B. Comparisons of Architectures

A comparison of the four Kalman filters examined for relative GPS navigation is performed in the following section. The root sum square (RSS) of the inertial position and velocity estimation errors of both vehicles are given. The estimation errors corresponding to the relative position and velocity are given for all three directions as well as a compilation of all errors in terms of the RSS error.

Figure 56 gives the RSS values of the sample standard deviations corresponding to the chaser vehicle for the PV, GPS, and reduced GPS EKFs. The RSS of the sample standard deviations pertaining to the target vehicle is given by Figure 57 for the same three EKFs. The RGPS EKF sample standard deviation is omitted from all inertial absolute plots due to the magnitude of the sample standard deviation compared to the other three filters. It is obvious from the discussion in Section 3 that

the RGPS filter performs significantly worse in absolute state estimation compared to the other three filters due to the measurements processed by the RGPS EKF.

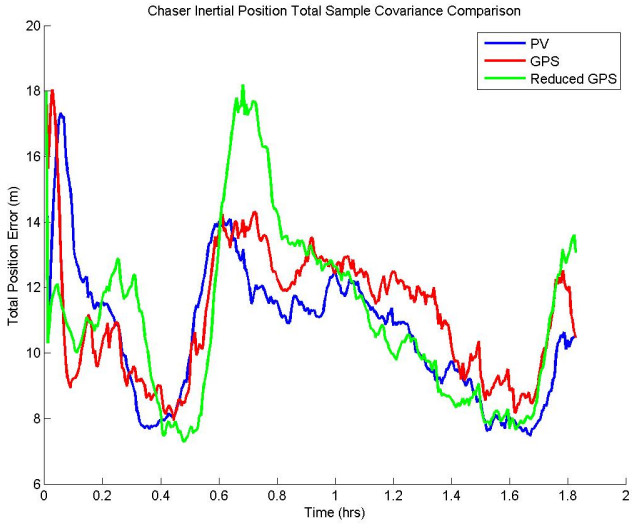

Fig. 56. Chaser Position RSS Sample Standard Deviation Comparison

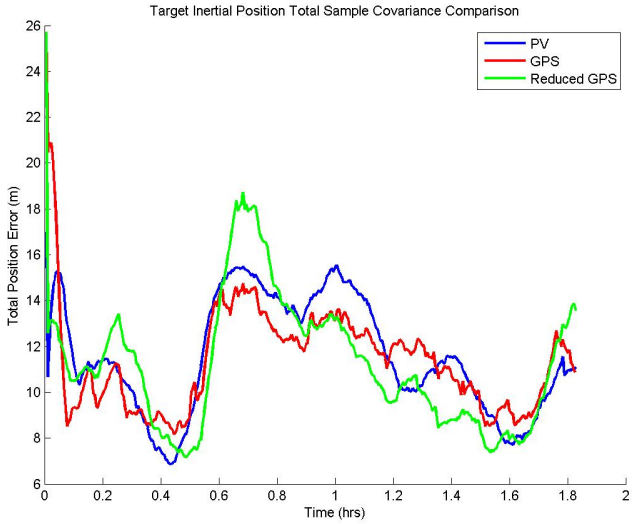

Fig. 57. Target Position RSS Sample Standard Deviation Comparison

The PV and GPS EKFs perform better than the reduced GPS EKF in position estimation for the majority of the proximity operations. It is evident from Figure 56 that the lag in the accelerometer bias estimation influences the state estimation of the PV filter more than the two GPS EKFs. The GPS filters allow for slightly more accurate state estimates but at a higher computational cost. Although the PV filter performs slightly worse for the first 0.3 hours in the chaser position compared to the GPS EKFs, the PV EKF performs as well as the GPS EKF and better than the reduced GPS EKF over the remainder of the proximity operations.

Figure 58 gives a comparison of the sample standard deviations of the PV, GPS and reduced GPS EKFs for the chaser velocity while Figure 59 gives a similar comparison for the target velocity. The PV filter is more sensitive to the thruster firings of the chaser vehicle than the two GPS filters. In addition, the lag in estimation of the accelerometer bias affects the PV filter more than the GPS EKFs. Comparing the sample standard deviations in Figure 59, it is concluded that all three filters perform essentially the same in absolute velocity estimation. The three filters perform similarly in the estimation of the chaser velocity with the exception of the first 0.3 hours where the PV filter performs worse than the two GPS filters. The presence of the thruster firings and accelerometer bias affects the absolute state estimation of the PV filter more so than the two GPS EKFs due to the simplicity of the PV filter. The non-linearity of the GPS filters allows for a better estimation of the absolutes states than does the PV filter.

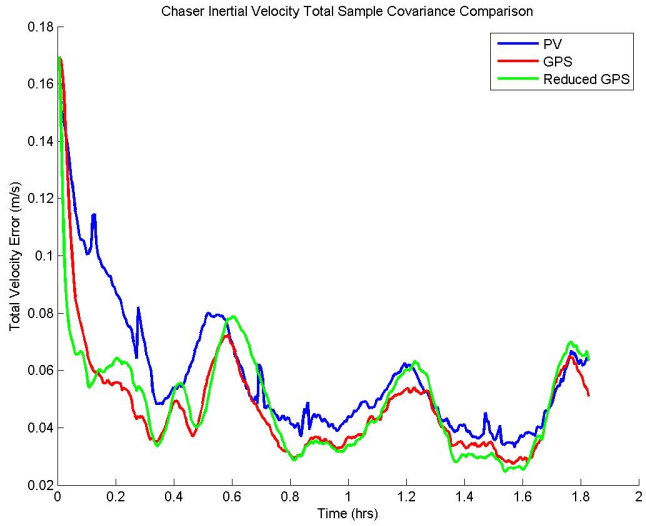

Fig. 58. Chaser Velocity RSS Sample Standard Deviation Comparison

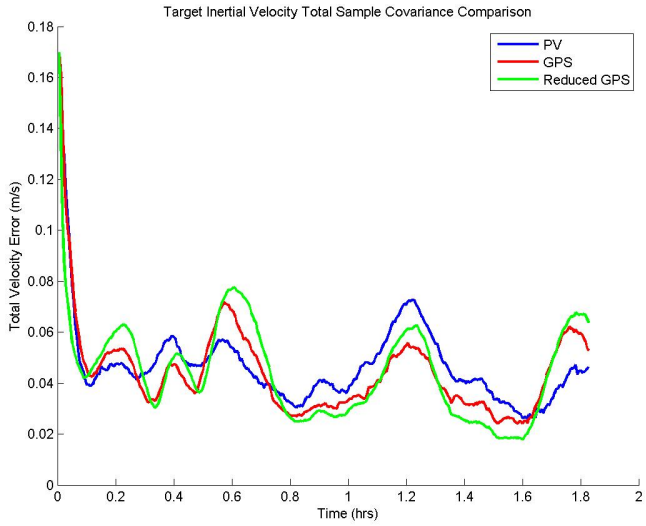

Fig. 59. Target Velocity RSS Sample Standard Deviation Comparison

Figure 60 is a comparison of the sample standard deviation for all four filters corresponding to the relative position between the two vehicles. The two GPS EKFs

and relative GPS EKF maintain an estimation error of approximately 2 meters in all directions over the entire duration of the proximity operations with the exception of the elevated sample standard deviations at the beginning due to the range of initial position errors. On the other hand, the PV filter consistently maintains an error of 5 meters in all direction except at the beginning when the error is on the order of 10 meters. By comparison, it is evident that the PV filter does not provide relative position information as well as the relative and two GPS EKFs.

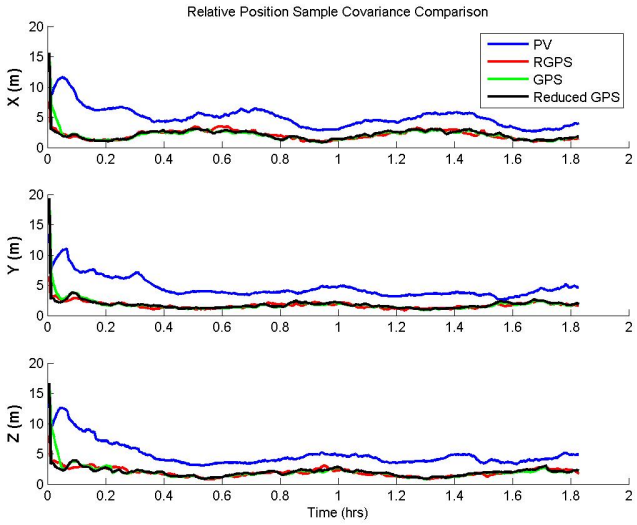

Fig. 60. Relative Position Sample Standard Deviation Comparison

Figure 61 provides a comparison of the total sample standard deviation of all four EKFs for the relative position between the two vehicles. Similar findings are concluded from Figure 61 as was from Figure 60. The difference in the sample standard deviations between the three filters that process some form of a pseudorange measurement is a matter of a few centimeters. On the other hand, the difference between the sample standard deviations of the three forms of GPS filters and the PV

filter is on the matter of at least 4 meters with some differences during the course of the proximity operations as high as 10 meters. This is expected since the PV filter is designed to perform well in absolute state estimation opposed to relative state approximation.

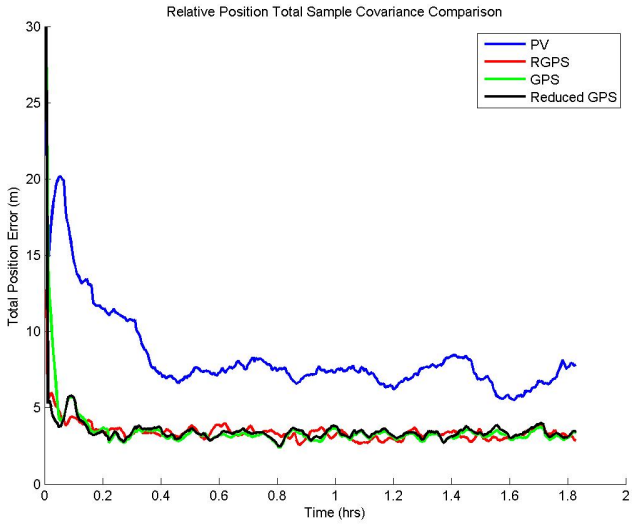

Fig. 61. Relative Position RSS Sample Standard Deviation Comparison

A comparison of the sample standard deviations for all four filters corresponding to the relative velocity between the two vehicles is given by Figure 62. The two GPS filters perform better than the PV and RGPS EKFs in terms of approximating the relative velocity. The PV and RGPS EKFs are more sensitive to the thruster firings of the chaser vehicle than are the GPS and reduced GPS EKFs.

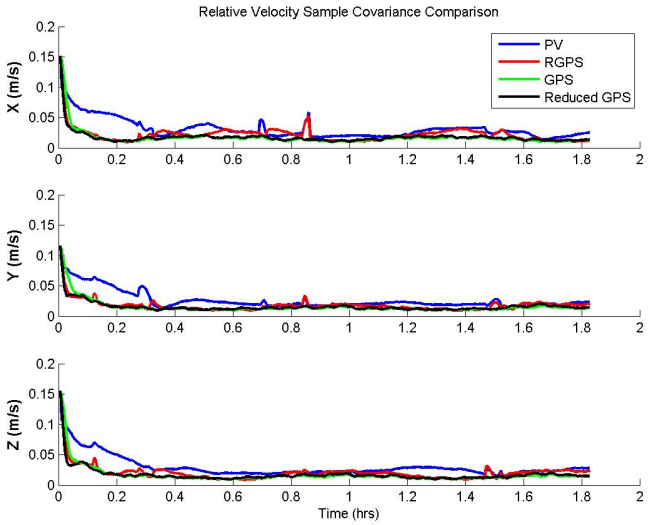

Fig. 62. Relative Velocity Sample Standard Deviation Comparison

Figure 63 gives the RSS of the sample standard deviations for all four filters for the relative velocity between the chaser and target vehicles. While the performance between the two GPS filters does not differ much, the performance of the PV and RGPS filters are worse. The spikes in the sample standard deviations refer to thruster firings performed by the chaser vehicle. The PV and RGPS filters are more sensitive in the accelerometer bias estimation hence the slightly elevated sample standard deviation of the two filters. The sensitivity of the PV filter with respect to the accelerometer bias is particularly evident over the first 0.3 hours of the proximity operations.

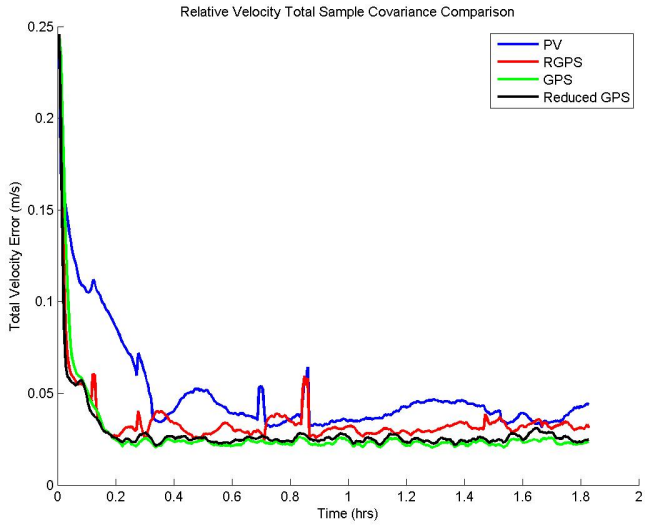

Fig. 63. Relative Velocity RSS Sample Standard Deviation Comparison

Although the RGPS EKF is designed to perform well in relative state approximation, it actually performs worse than both GPS filters that are able to accurately estimate the absolute position and velocity states. The RGPS EKF performs worse due to the presence of high multipath error corresponding to the ISS. Currently the uncommon pseudorange errors are modeled as white noise. However, the pseudorange errors are a result of colored noise. Although the standard deviation of colored noise is approximately 2.5 meters, the standard deviation of the white noise is required to be approximately two times higher for the filter to properly estimate the relative states. Modeling the colored noise as white noise results in a performance decrease. One advantage of the RGPS EKF is it removes all common pseudorange errors by processing relative measurements and provides good relative information without the addition of extra states. However, due to the size of the multipath error, additional states are needed. Since the uncommon colored noise is modeled as white noise and no additional states are included, the performance of the RGPS EKF is worse in rel-

ative state estimation as compared to the two other GPS filters. In order to achieve a similar performance, additional states are needed which voids one of the advantages of the RGPS EKF. If additional states are omitted, it is then more beneficial to implement a GPS EKF opposed to a RGPS EKF.

Table XIV summarizes the advantages and disadvantages of each Kalman filter architecture analyzed. The values corresponding to the absolute and relative performance are the average of the sample covariances.

Table XIV. Kalman Architecture Comparison

	PV	**RGPS**	**GPS**	**Reduced GPS**
Error Directionality	No	Yes	Yes	Yes
Computational Cost	Medium	Low	High	Medium
Relative Performance	7.7 m 0.044 m/s	3.3 m 0.032 m/s	3.2 m 0.023 m/s	3.3 m 0.025 m/s
Absolute Performance	11 m 0.049 m/s	1000 m 2 m/s	11 m 0.045 m/s	11 m 0.047 m/s
Comments	4+ visible GPS satellites required	Similar antenna orientation of both vehicles and measurement synchronization	Bookkeeping of internal states estimated	None

CHAPTER VII

CONCLUSIONS

A GPS sensor model for an orbiting spacecraft has been developed and error sources calibrated based on specifications of a GPS sensor typically used in space applications. An algorithm has been developed that estimates the GPS receiver's velocity and clock drift based upon pseudorange and range rate measurements as well as an estimated position of the GPS receiver. A visibility analysis has been performed to determine the half cone angle of a GPS receiver on an orbiting spacecraft that allows for the visibility of four GPS satellites during the proximity operations. The theory behind the extend Kalman filter architecture has been outlined and implemented in the four Kalman filter architectures analyzed. The advantages and disadvantages of each architecture are discussed in this section in addition to a more in-depth comparison of the architectures.

The PV EKF processes position and velocity estimates supplied by the GPS sensors. The algorithms used for position and velocity estimation calculate absolute position and velocity estimates from pseudoranges determined from the C/A code. As a result, the errors in the estimated position can be 1-100 meters which then appear in the velocity estimate [9]. Pseudoranges can also be calculated by measuring the received phase of the transmitted GPS frequencies. By processing carrier phase pseudoranges, the accuracy of the position estimate increases by as much as two orders of magnitude which in turn increases the accuracy of the velocity estimation. This increase in accuracy is due to the short period of the carrier waveform. However, since the phase is measured in terms of 2π, additional measurements, frequently code pseudoranges, are needed to effect ambiguity resolution [42]. With relative navigation the main focus of this thesis, relative position is of more importance than

absolute position. A direct relative position estimation algorithm has been developed allowing for an increased accuracy in relative position estimation by an order of magnitude compared to relative position calculated by differencing absolute position estimates [43]. This algorithm is similar to the approach taken in the RGPS EKF. The increase in accuracy is due to less multipath on the measurements (<1 m) in addition to the higher orbiting altitude of the satellites. For the current analysis, the GPS signals pass through an additional 250 kilometers of the atmosphere compared to the satellites in reference [43] which results in more disperse ionosphere errors on the measurements. When differenced, less atmosphere errors cancel than compared to satellites at higher altitudes contributing to higher errors in the relative position estimation. Although relative states are key to relative navigation, absolute state information is also desired for the analysis performed in this thesis. As a result, a dual inertial filter is the basis for the four Kalman filter architectures. While carrier phase pseudoranges have been combined with code pseudoranges in Kalman filter architectures [44], code pseudoranges are solely used in this thesis for position estimation by the GPS sensors to reduce complexity. The higher errors are accounted for during state estimation performed by the Kalman filters.

One advantage of the PV EKF is in the measurements being processed. The PV EKF processes approximate position and velocity measurements computed by the GPS sensor. The measurements correspond to the inertial states of the vehicle. By processing inertial position and velocity measurements, the complexity of the filter is significantly reduced. Additional computations are avoided and the relation between the measurements and estimated states are linear. The addition of extra states to model errors present in the position and velocity measurements add little complexity to the PV EKF.

One disadvantage of the PV EKF is it does not assign directionality to the po-

sition and velocity errors. Therefore, if there is a 10 meter error in the X direction but only a 1 meter error in the Y and Z direction in position, the predicted standard deviation for all three directions corresponds with the 10 meter error. The predicted standard deviation for the directions with the smaller errors is too conservative for the size of the errors. In order to account for the directionality of the error, similar calculations performed by the GPS sensor to get the approximate position and velocity need to be performed. The advantage of acquiring the approximate position and velocity is nullified by performing the same calculations as performed by the GPS receiver. Due to the inability of the PV filter to assign error directionality, the estimation errors are slightly larger in terms of relative position and velocity as compared with an RGPS or GPS filter. The inability of the filter to remove common state errors from the pseudorange measurements also contributes to the larger relative estimation errors. When the estimated position and velocity measurements are calculated inside the GPS sensor, the errors present on each pseudorange measurement become embedded in the position and velocity estimation. As a result, the errors can no longer be canceled out and therefore contribute to the larger estimation errors.

An advantage of the RGPS EKF is its ability to perform well in terms of approximating relative states from inertial state estimation. By processing relative pseudoranges, the RGPS filter is capable of maintaining significantly lower errors in the approximation of relative states from the estimated inertial states compared to the PV filter. In addition, less states are estimated therefore the RGPS EKF has a lower computational cost.

While the RGPS EKF performs well with respect to relative state approximation, it cannot accurately estimate the current absolute position and velocity of either vehicle. The RGPS filter experiences this disadvantages due to the processing of relative measurements. Since only relative measurements are being processed, there is

no knowledge of the current inertial position and velocity states. Without any knowledge, the uncertainty in the estimation grows triggering the growth in the predicted standard deviations. The inertial states of each vehicle is essentially propagated over the duration of the proximity operations when the RGPS filter is used. As previously mentioned, there are multiple designs for a RGPS EKF. One design involves estimating the relative position, velocity, clock bias and drift between the two vehicles [11]. By estimating eight states, the computational cost of the filter is low. However, no absolute information is received from the relative filter therefore an external absolute filter is needed. By using two filters, the correlation between the measurements processed and states estimated is neglected resulting in less accurate state estimation. In this thesis, a dual inertial state filter is used for the four filters to allow for a direct comparison. Therefore, inertial information is received but the filter essentially only propagates the inertial position and velocity of each vehicle. More accurate inertial information can be obtained by processing different measurements (pseudorange or estimated position and velocity of both vehicles) but the complexity of the filter increases as a result. In addition, the RGPS EKF cannot properly model the multipath error as white noise therefore resulting in worse performance when compared to both GPS filters. Additional states are needed to properly model the multipath errors due to the elevated multipath error of the ISS but the addition of states results in a more complex filter. The increase in the complexity due to the processing of different measurement or addition of error states results in an increase in the computational cost nullifying one advantage of the RGPS EKF.

The GPS EKF is an advantageous filter in terms of its ability to perform well in both absolute state estimation and relative state approximation from the estimated absolute states. This advantage arises from the ability of the filter to determine error directionality. Since pseudorange measurements are being processed, performance in

absolute state estimation is similar to the PV filter as opposed to the performance of the RGPS filter. By processing an absolute distance from GPS satellites opposed to a relative distance between the two vehicles, the accuracy of the absolute state estimation increases. Error directionality is another advantage to the GPS EKF. The pseudorange measurements processed allow for error directionality since the GPS satellites are oriented at varying elevation angles. As a result, larger error appear in one direction for one satellite and appear in another direction for another satellite. Combining the variation of these errors, the GPS EKF is capable of better determining the magnitude of the errors in each direction.

The GPS EKF does have a disadvantage that arises from the non-linearity in the pseudorange measurements processed. Due to the measurements, the complexity of the filter is higher compared to the PV filter since non-linear equations are included to calculate an estimated pseudorange from the estimated states. As a result of the higher complexity, the GPS EKF also comes with a higher computational cost. In addition to the complexity due to the non-linearity of the measurements, the GPS EKF also accounts for additional states to model common pseudorange errors present in each satellite being processed. Since the common pseudorange error is unique to each satellite, the six additional states added to model these errors need to be closely monitored during the implementation of the GPS EKF. Bookkeeping of previous satellites corresponding to processed pseudorange measurements is performed in order to accurately model the common pseudorange errors. When satellites are lost, acquired, or rearranged in order, the appropriate pseudorange error from the previous update and propagation is shifted to the new position of the corresponding pseudorange error. This bookkeeping adds even more complexity to the filter in turn raising the computational costs of the GPS filter.

The reduced GPS EKF attempts to take advantage of the GPS EKF while min-

imizing the disadvantages. While the reduced GPS EKF cannot escape the nonlinearity in the pseudorange measurements, the reduced GPS EKF significantly minimizes the complexity of the GPS EKF by not estimating the additional states corresponding to the common pseudorange errors. While the states are not estimated, the states are considered and therefore remain part of the state vector. By doing so, the remaining states being estimated are influenced by the states not estimated by the presence of correlation terms in the estimation error covariances corresponding to the pseudorange errors not estimated. The rows and columns of the estimation error covariance corresponding to the common pseudorange error states are allowed to evolve with time therefore influencing the states being estimated. The advantage of good performance in both absolute state estimation and relative state approximation is retained as is the ability to determine error directionality. However, the resulting estimation errors are more conservative compared to the GPS EKF since the common pseudorange error states are only considered and the bookkeeping of the common pseudorange error states is removed.

The complexity and computation costs of the reduced GPS EKF is still higher than the PV filter but less than the GPS EKF since the bookkeeping of GPS satellites is avoided. Since it is avoided, the evolution of the estimation error covariances does not involve rearranging rows and columns based upon the acquisition, loss, or rearrangement of satellites from which pseudorange measurements are being processed. The estimation error covariance is allowed evolve assuming the correlation between the estimated states and common pseudorange error states vary little from satellite to satellite. In addition, the covariances and correlations of the six common pseudorange errors are assumed to vary little from satellite to satellite as well.

In conclusion, there are advantages and disadvantages to each filter. While the PV filter performs well in absolute state estimation, its lacks in the ability to supply

small errors in relative position and velocity. The RGPS EKF is capable of providing small errors in the relative position and velocity between the two vehicle but cannot provide the user with any usable inertial state information. In addition, complications arise in the presence of multipath rich environments. The GPS EKF provides the best of both worlds by being able to perform similar to the PV filter in terms of absolute state navigation and similar to the RGPS EKF in terms of relative state approximation. While the all around performance is better, the higher complexity of the filter results in the highest computational cost of the four Kalman filters studied. The reduced GPS EKF combines the advantages of the GPS EKF while minimizing the disadvantages of the GPS EKF. While the complexity and computational cost of the filter are still higher compared to the RGPS EKF, the complexity and computational cost are less than the GPS EKF since satellite bookkeeping is avoided. The overall performance in both absolute and relative navigation provided by the reduced GPS EKF is nearly equivalent to that of the GPS EKF.

REFERENCES

[1] K. Tom, *Echoes of Old China*. Honolulu, HI: University of Hawai'i Press, 1989.

[2] R. H. Battin, *An Introduction to the Mathematics and Methods of Astrodynamics,* Revised ed. Reston, VA: American Institute of Aeronautics and Astronautics, Inc., 1999.

[3] D. Sobel, "A brief history of early navigation," *Johns Hopkins APL Technical Digest*, vol. 19, pp. 11–13, 1998.

[4] M. Skolnik, *Introduction to Radar Systems,* 3rd ed. New York: McGraw-Hill, 2001.

[5] J. J. Spilker, B. W. Parkinson, P. Axelrad, and P. Enge, *Global Positioning System: Theory and Application*. Reston, VA: American Institute of Aeronautics and Astronautics, Inc., 1996, vol. I.

[6] A. El-Rabbany, *Introduction to GPS: The Global Positioning System*. Norwood, MA: Artech House, Inc, 2002.

[7] M. Selinger and D. Ball, "Global positioning system (GPS) IIF," http://www.boeing.com/defense-space/space/gps/docs/GPSIIF_overview.pdf, The Boeing Company, accessed on August 24, 2009.

[8] G. Xu, *GPS: Theory, Algorithms, and Application,* 2nd ed. New York: Springer, 2003.

[9] M. S. Grewal, L. R. Weill, and A. P. Andrews, *Global Positioning Systems, Inertial Navigation, and Integration,* 2nd ed. Hoboken, NJ: John Wiley & Sons, Inc., 2007.

[10] P. Kachmar, "Apollo and space shuttle on-board navigation systems: Application of Kalman filtering techniques," in *Proceedings of the Institute of Navigation 58th Annual Meeting/CIGTF 21st Guidance Test Symposium.* Albuquerque, NM: American Institute of Aeronautics and Astronautics, AIAA Paper # 08-7295, June 2002, pp. 24–26.

[11] J. Gonnaud and V. Pascal, "ATV guidance navigation and control for rendezvous with ISS," in *Proceedings of the 4th ESA International Conference on Spacecraft Guidance, Navigation and Control Systems.* Noordwijk, The Netherlands: European Space Agency, October 1999, pp. 501–510.

[12] J. Gonnaud, L. Lagarde, S. Strandmoc, and A. Ballereau, "Relative GPS navigation implementation for the ATV rendezvous," in *Proceedings of the 5th ESA International Conference on Spacecraft Guidance, Navigation and Control Systems.* Frascati, Italy: European Space Agency, October 2002, pp. 225–232.

[13] K. Yamanaka, K. Yokota, K. Yamada, S. Yoshikawa, H. Koyama, K. Tsukahara, and T. Nakamura, "Guidance and navigation system design of r-bar approach for rendezvous and docking," in *Proceedings of the International Communications Satellite Systems Conference and Exhibit, 17th.* Yokohama, Japan: American Institute of Aeronautics and Astronautics, February 1998, pp. 23–27.

[14] C. D'Souza, A. Bogner, T. Brand, J. Tsukui, H. Koyama, and T. Nakamura, "An evaluation of the GPS relative navigation system for ETS-VII and HTV," in *Proceedings of the 22nd Annual AAS Guidance and Control Conference.* Breckenridge, CO: American Astronautical Society, February 1999, pp. 239–257.

[15] H.Mamich and C. D'Souza, "Orion preliminary navigation system design," in *Proceedings of the AIAA Guidance, Navigation and Control Conference and Ex-*

hibit. Honolulu, HI: American Institute of Aeronautics and Astronautics, August 2008, pp. 18–21.

[16] H. Hu and T. Straube, "Orion GN&C overview and architecture," in *Proceedings of the AIAA Guidance, Navigation and Control Conference and Exhibit.* Hilton Head, SC: American Institute of Aeronautics and Astronautics, AAS Paper #07-6678, August 2007, pp. 1–12.

[17] F. Busse and J. How, "Demonstration of adaptive extended Kalman filter for low Earth orbit formation estimation using CDGPS," *NAVIGATION, Journal of The Institute of Navigation*, vol. 50, pp. 79–94, 2003.

[18] M. L. Mitchell, "CDGPS-based relative navigation for multiple spacecraft," M.S. thesis, Massachusetts Institute of Technology, Cambridge, MA, June 2004.

[19] S. C. Jenkins and D. K. Geller, "State estimation and targeting for autonomous rendezvous and proximity operations," in *Proceedings of the AAS/AIAA Astrodynamics Specialists Conference.* Mackinac Island, MI: American Astronautical Society, AAS Paper #07-316, August 2007, pp. 1071–1102.

[20] D. A. Vallado, *Fundamentals of Astrodynamics and Applications,* 3rd ed. Hawthorne, CA: Microcosm, Inc., 2007.

[21] R. Alonso, J. L. Crassidis, and J. L. Junkins, "Vision-based relative navigation for formation flying of spacecraft," in *Proceedings of the AIAA Guidance, Navigation, and Control Conference.* Denver, CO: American Institute of Aeronautics and Astronautics, AIAA Paper #00-4439, August 2002, pp. 1–11.

[22] R. G. Brown and P. Y. Hwang, *Introduction to Random Signals and Applied Kalman Filtering,* 3rd ed. New York: John Wiley & Sons, Inc., 1967.

[23] J. A. Klobuchar, "Ionospheric time-delay algorithm for single-frequency GPS users," *IEEE Transactions on Aerospace and Electronic Systems*, vol. 3, pp. 325–331, May 1987.

[24] P. Gustavsson, "Development of a matlab-based GPS constellation simulation for navigation algorithm developments," M.S. thesis, Luleå University of Technology, Luleå, Sweden, April 2005.

[25] B. Hofmann-Wellenhof, H. Lichtenegger, and J. Collins, *GPS Theory and Practice:* 5th, revised ed. New York: Springer-Verlag/Wien, 2001.

[26] J. J. Spilker, B. W. Parkinson, P. Axelrad, and P. Enge, *Global Positioning System: Theory and Application.* Reston, VA: American Institute of Aeronautics and Astronautics, Inc., 1996, vol. II.

[27] E. D. Kaplan and C. J. Hegarty, *Understanding GPS: Principles and Applications,* 2nd ed. Norwood, MA: Artech House, Inc., 2006.

[28] B. W. Remondi, "Computing satellite velocity using the broadcast ephemeris," *GPS Solutions*, vol. 8, pp. 181–183, August 2004.

[29] S. Bancroft, "An algebraic solution of the GPS equations," *IEEE Transactions on Aerospace and Electronic Systems*, vol. AES-21, no. 7, pp. 56–59, January 1985.

[30] P. R. Escobal, *Methods of Orbit Determination.* New York: John Wiley & Sons, Inc., 1965.

[31] J. L. Crassidis and J. L. Junkins, *Optimal Estimation of Dynamic Systems.* New York: CRC Press LLC, 2004.

[32] "Iss trajectory data," http://spaceflight.nasa.gov/realdata/sightings/SSapplications/Post/JavaSSOP/orbit/ISS/SVPOST.html, National Aeronautics and Space Administration, accessed on March 5, 2009.

[33] M. Osenar, "Performance of automated feature tracking cameras for lunar navigation," M.S. thesis, Rice University, Houston, TX, April 2007.

[34] J. B. Kuipers, *Quaternions and Rotation Sequences: A Primer with Applications to Orbits, Aerospace, and Virtual Reality*. Princeton, NJ: Princeton University Press, 1999.

[35] W. S. Flenniken, J. H. Wall, and D. M. Bevly, "Characterization of various IMU error sources and the effect on navigation performance," in *Proceedings of the 2005 ION GNSS*, Long Beach, CA, September 13-16 2005, pp. 1–12.

[36] M. Osenar, F. Clark, and C. D'Souza, "Performance of an automated feature tracking lunar navigation system," in *Proceedings of the 31st Annual AAS Guidance and Control Conference*. Breckenridge, CO: American Astronautical Society, Paper # AAS 08-101, February 2008, pp. 23–40.

[37] "GG5300 Three Axis MEMS Rate Gyro Package," http://www.honeywell.com/sites/servlet/com.merx.npoint.servlets.DocumentServlet?docid=D35976465-FA39-F5B2-79C1-F0FD8E49DF03, Honeywell International Inc., accessed on April 23, 2009.

[38] "Q-Flex QA-3000 Accelerometer," https://www.honeywell.com/sites/servlet/com.merx.npoint.servlets.DocumentServlet?docid=D35C68575-7711-02ED-121B-93D839D7099D, Honeywell International Inc., accessed on April 23, 2009.

[39] R. Stengel, *Optimal Control and Estimation*. Mineola, NY: Dover Publications, Inc., 1994.

[40] M. H. Kaplan, *Modern Spacecraft Dynamics & Control*. Hoboken, NJ: John Wiley & Sons, Inc., 1976.

[41] H. Schaub and J. L. Junkins, *Analytical Mechanics of Space Systems*. Reston, VA: American Institute of Aeronautics and Astronautics, Inc., 2003.

[42] G. Blewitt, "Carrier phase ambiguity resolution for the global positioning system applied to geodetic baselines up to 2000 km," *Journal of Geophysical Research*, vol. 94, pp. 10 187–10 203, August 1989.

[43] M.-P. Rudel and P. Gurfil, "Precise spacecraft relative positioning using single-frequency pseudorange measurements," *The Journal of Navigation*, vol. 62, pp. 119–134, 2009.

[44] P. Y. Hwang and R. G. Brown, "GPS navigation: Combining pseudorange with continuous carrier phase using a Kalman filter," *NAVIGATION: Journal of The Institute of Navigation*, vol. 37, no. 2, pp. 181–196, 1990.

APPENDIX A

IONOSPHERE MODEL DERIVATION

The ionospheric modeled used during the development of the GPS measurement model is the Klobuchar model. The Klobuchar model assumes a cosine representation of the diurnal curve which varies in amplitude and period based on the latitude location of the GPS receiver. The model for a spaceborne GPS receiver [24] is derived from the Klobuchar model as given for a ground based GPS receiver [23]. The primary difference between a spaceborne receiver and ground based receiver is the immediate point (IP) of the ionosphere. Figure 64 shows the difference in how the location of the IP is determined based upon the location of the GPS receiver. The two red triangles denotes the IP corresponding to each receiver.

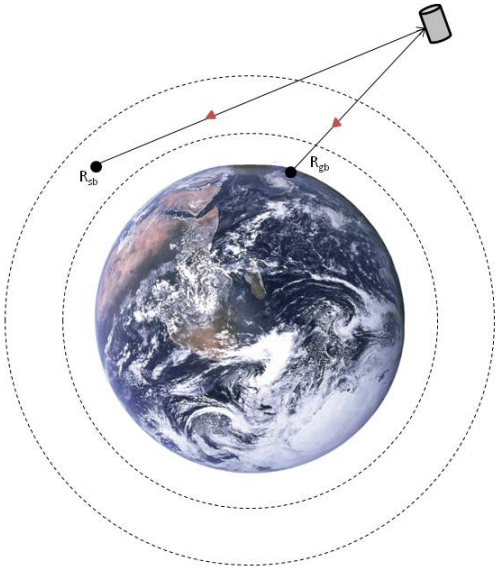

Fig. 64. Intermediate Point for Ionospheric Error Calculation

Three cases must be considered for a spaceborne receiver dependent on the location of the receiver; below, inside or above the ionosphere. Recall the ionosphere has a basement of 50 kilometers and ceiling of 1000 kilometers, both measured as altitude above sea level. The derivation of the ionospheric model for a spaceborne GPS receiver is as follows. Many angles will be defined in the following derivation that deal with the geometry between vectors from the center of the Earth to crossing of the ionosphere basement or ceiling with that of the line of sight (LOS) vector defined from the receiver to the GPS satellite. A visual representation of the angles determined below can be found in Reference [24].

Determine the azimuth, A, the elevation, E, and the geodetic coordinates (lat,log,alt), (ϕ, λ, h) given the position of the GPS receiver $\mathbf{r}$ and current GPS satellite $\mathbf{r_{gps_i}}$ from the center of the Earth. The LOS vector is computed by taking the cross product of the position of the receiver and satellite. Compute the zenith and Euler axis of rotation using Equations A.1-A.3.

$$Z = \frac{pi}{2} - E \tag{A.1}$$

$$\mathbf{r}_{los} = \mathbf{r}_{gps_i} \times \mathbf{r} \tag{A.2}$$

$$\hat{\mathbf{e}} = \frac{\mathbf{r_{los}}}{\|\mathbf{r_{los}}\|} \tag{A.3}$$

The radius of the earth at the given latitude is computed using Equation A.4 and the basement and ceiling of the ionosphere defined. Define ζ_1 to be the angle between the LOS and the vector from the center of the Earth to the point of intersection of the LOS vector with the ceiling of the atmosphere.

$$R_n = \frac{a_E}{\sqrt{1 - e_E^2 \sin^2(\phi_g)}} \tag{A.4}$$

$$r_{I_{max}} = R_n + h_{I_{max}} \tag{A.5}$$

$$r_{I_{min}} = R_n + h_{I_{min}} \tag{A.6}$$

$$\xi = \pi - Z \tag{A.7}$$

$$\zeta_1 = \arcsin\left(\frac{\|\mathbf{r}\| \sin(\xi)}{r_{I_{max}}}\right) \tag{A.8}$$

CASE 1: GPS receiver located <u>below</u> the ionosphere.

Compute the following angles in order to determine the radius to the IP as given in Equation A.13.

$$\zeta_3 = \arcsin\left(\frac{\|\mathbf{r}\| \sin(\xi)}{r_{I_{min}}}\right) \tag{A.9}$$

$$\nu = \pi - \zeta_3 \tag{A.10}$$

$$\gamma = \pi - \zeta_1 - \nu \tag{A.11}$$

$$p_I = \frac{\sin(\gamma)}{\sin(\nu)} r_{I_{min}} \tag{A.12}$$

$$d_{ip} = \frac{1}{2}\sqrt{2(r_{I_max}^2 + r_{I_min}^2) - p_I^2} \tag{A.13}$$

CASE 2: GPS receiver located inside the ionosphere.

The following angle and distance between the GPS receiver and intersection of the ceiling of the ionosphere are used to determine the distance from the center of the Earth to the IP ad defined by Equation A.16. It is assumed in the implementation of the ionosphere model that the floor of the ionosphere will not be intersected by a LOS vector for a spacecraft inside or above the ionosphere.

$$\gamma = \pi - \zeta_1 - \xi \tag{A.14}$$

$$p_I = \frac{\sin(\gamma)}{\sin(\xi)} r_{I_{max}} \tag{A.15}$$

$$d_{ip} = \frac{1}{2}\sqrt{2(\|\mathbf{r}\|^2 + r_{I_{max}}^2) - p_I^2} \tag{A.16}$$

The following equations are common for a GPS receiver location either below or inside the ionosphere. The solution to Equation A.21 is used to determine the geodetic coordinates of the IP (ϕ_{ip}, λ_{ip}, h_{ip}) which are used in the calculation of the ionospheric time delay.

$$\zeta_2 = \arcsin\left(\|\mathbf{r}\| \frac{\sin(\xi)}{d_{ip}}\right) \tag{A.17}$$

$$\upsilon = \pi - \zeta_2 - \xi \tag{A.18}$$

$$\hat{\mathbf{r}} = \frac{\mathbf{r}}{\|\mathbf{r}\|} \tag{A.19}$$

$$\hat{\mathbf{d}}_{ip} = \mathbf{T}(\hat{\mathbf{e}}, -\upsilon)\hat{\mathbf{r}} \tag{A.20}$$

$$\mathbf{d}_{ip} = \hat{\mathbf{d}}_{ip} \cdot d_{ip} \tag{A.21}$$

where $\mathbf{T}$ is the transformation matrix defined by Equation A.22 where $[\hat{\mathbf{u}}^{\times}]$ denotes the skew symmetric matrix of the principle axis of rotation.

$$T(\hat{\mathbf{u}}, \theta) = \cos\theta I_{3\times 3} + (1 - \cos(\theta))\hat{\mathbf{u}}\hat{\mathbf{u}}^T - \sin(\theta)\left[\hat{\mathbf{u}}^{\times}\right] \tag{A.22}$$

CASE 3: GPS receiver located above the ionosphere

For a receiver located above the ionosphere, the only ionospheric delay will result from LOS vectors that intersect the ceiling of the ionosphere meaning GPS signals passing into and back out of the ionosphere. In order for the signal from the GPS satellite to intersect the ionosphere, the elevation corresponding to the LOS vector must be less than the elevation of the top of the ionosphere, found using Equation A.23.

$$E_I = -\arccos\frac{R_n + h_{I_{max}}}{R_n + h} \tag{A.23}$$

For the current case, an effective calculation point (ECP) and corresponding elevation angle must be calculated at the point where the LOS vector first intersects the ceiling of the ionosphere. Using this point, the effective ionosphere delay can be found. The following equations are used to determine the ECP where the transformation matrix T is found using Equation A.22.

$$\zeta = \pi - \arcsin\left(\|\mathbf{r}\|\frac{\sin\xi}{R_n + h_I}\right) \tag{A.24}$$

$$\psi = \pi - \zeta - \xi \tag{A.25}$$

$$E_{ecp} = \frac{pi}{2} - \zeta \tag{A.26}$$

$$\hat{\mathbf{d}}_{ecp} = T(\hat{\mathbf{e}}, -\psi)\hat{\mathbf{r}} \tag{A.27}$$

$$\mathbf{d}_{ecp} = \hat{\mathbf{d}}_{ecp} \cdot d_{ecp} \tag{A.28}$$

Contrary to the case of a GPS receiver located below or inside the ionosphere, the the geodetic coordinates are found using $\mathbf{d}_{ecp}$ instead of $\mathbf{d}_{ip}$. With the determination of the geodetic coordinates of either the IP or ECP, the following set of equations are used to determine the ionospheric time delay.

Define the geomagnetic pole coordinates to be $\phi_p = 78.3°$ for latitude and $291.0°$ for longitude. Combining the geodetic coordinates of the intermediate point (or ECP) with those of the geomagnetic pole, the quantity $\phi_i p^m$ is defined by Equation A.29.

$$\phi_{ip}^m = \arccos\left(\sin(\phi_{ip})\sin(\phi_p) + \cos(\phi_{ip})\cos(\phi_p)\cos(\lambda_{ip} - \lambda_p)\right) \tag{A.29}$$

The broadcast ephemeris transmit correction terms to be used during the calculation of the ionosphere error. These correction terms are common to all satellites and included in the common portion of the ephemeris data. The correction term coefficients as given by the broadcast ephemeris are combined with ϕ_{ip}^m to produce the following coefficients used in the calculation of the ionospheric time delay.

$$C_1 = \sum_{n=0}^{3} \alpha_n \, {\phi_{ip}^m}^n \tag{A.30}$$

$$C_2 = \sum_{n=0}^{3} \beta_n \, \phi_{ip}^{m\,n} \tag{A.31}$$

The coefficient C_1 refers to the amplitude of the cosine function while C_2 defines the period. The ionosphere time delay should always be a positive scalar value therefore if the amplitude as calculated by Equation A.30 is calculated to be less than zero, the amplitude is then defined to be zero. With the definition of the amplitude and period of the cosine function, the ionospheric time delay is defined by the following equation.

$$\Delta T_{iono} = SF \cdot \left(C_3 + C_1 \cos\left(\frac{2\pi(t - C_4)}{C_2} \right) \right) \tag{A.32}$$

Equation A.32 can also be rewritten as a fourth order Taylor series expansion of the cosine function. C_3 is a constant time delay of 5×10^{-9} (ns) and C_4 is defined to be a constant of 14 hours given in seconds. The current local time, t, is found using Equation A.33.

$$t = \frac{\lambda_{ip}}{15} + t_{ut} \tag{A.33}$$

The time value, t_{ut} refers to the universal time and is broadcast in the ephemeris data. Since the GPS satellite seen by the receiver is not often directly above, the time delay due to the presence of the ionosphere is multiplied by a scale factor, SF. The scale factor is found using Equation A.34. The angle z' is defined as the satellite zenith angle at the IP.

$$SF = \frac{1}{\cos(z')} \tag{A.34}$$

$$z' = \arcsin\left(\frac{R_n}{R_n + h_{ip}}\sin(Z)\right) \tag{A.35}$$

The total error as contributed by the ionosphere in meters is determined by multiplying the computed time delay by the speed of light.

APPENDIX B

TROPOSPHERE MODEL DERIVATION

There are two regions of the troposphere which are addressed in the derivation of the tropospheric time delay [25]. It is assumed that knowledge of the elevation, azimuth, geodetic coordinates and radius of the Earth at the current position of the vehicle, the tropospheric is known in the following derivation. Let T_0 be 288.16 K and the ceiling of the wet portion of the troposphere be 11 km. The ceiling of the troposphere is found using Equation B.1.

$$h_{dry} = 40136 + 148.72 \cdot (T_0 - 273.16) \tag{B.1}$$

Define an elevation mapping function, M.

$$M_{dry} = \begin{cases} M_{dry} = \frac{1}{\sqrt{E^2+6.25}} & E > 0 \\ M_{dry} = 0.4 & E \leq 0 \end{cases}$$

$$M_{wet} = \begin{cases} \frac{1}{\sqrt{E^2+2.25}} & E > 0 \\ \frac{2}{3} & E \leq 0 \end{cases}$$

where E is the elevation in radians. The Hopfield troposphere model is used to calculate the time delays resulting from the presence of the troposphere. Let P_0 and e_0 be defined as 1013.25 mb and 0.085 mb. The refractive indices of the wet and dry portions of the atmosphere are given by Equations B.2 and B.3 respectively.

$$N_{wet} = (-12.96T_0 + 3.718 \times 10^5)\frac{e_0}{T_0^2} \tag{B.2}$$

$$N_{dry} = 77.64\frac{P_0}{T_0} \tag{B.3}$$

The time delay resulting from the wet and dry portions of the troposphere is given by the following equations.

$$\Delta T_{wet} = \frac{10^{-6}}{5\,c} N_{wet} \frac{(h_{wet} - h)^5}{h_{wet}^4} M_w et \quad h > h_{wet} \tag{B.4}$$

$$\Delta T_{dry} = \frac{10^{-6}}{5\,c} N_{dry} \frac{(h_{dry} - h)^5}{h_{dry}^4} M_d ry \tag{B.5}$$

Note that for an altitude of a receiver greater than the ceiling of the wet portion of the troposphere, the time delay resulting from the wet portion of the troposphere is zero. The total error due to the troposphere in meters is computed by Equation B.6 with SF defined as a scale factor.

$$E = SF \cdot (\Delta T_{wet} + \Delta T_{dry}) \tag{B.6}$$

There are three cases that are considered for the time delay resulting from the presence of the troposphere. The three cases are as follows.

1. Receiver inside troposphere with positive elevation
2. Receiver inside troposphere with negative elevation
3. Receiver outside of troposphere

For the case of a user inside with a positive elevation, all above derived equations hold true and the scale factor is 1. For a user inside with a negative elevation, an intermediate point (IP) is determined such that the elevation angle with respect to this point is zero. The altitude of the IP is calculated using Equation B.7.

$$h_{ip} = \cos(\beta)(R_n + h) - R_n \tag{B.7}$$

The quantity β is equal to the original negative value of the elevation angle. The solution to Equation B.7 is used in place of h during the calculation performed in the Hopfield troposphere model. The scale factor is defined by Equation B.8.

$$\begin{aligned} X &= \sqrt{(R_n + h_a)^2 - (R_n + h_{ip})^2} \\ Y &= \sqrt{(R_n + h)^2 - (R_n + h_{ip})^2} \end{aligned}$$

where h_a is replaced by the ceiling of the portion of the atmosphere the receiver is located in.

$$SF = 1 + \frac{Y}{X} \tag{B.8}$$

For a receiver located outside of the troposphere, there is a slim chance for which a signal may pass through the troposphere. For this case, an effect calculation point (ECP) is calculated in a similar manner as for the ionosphere time delay. An elevation of the ceiling of the troposphere with respect to receiver is calculated by Equation B.9 and compared with the elevation of the GPS satellite. If the calculated elevation is greater than the elevation of the GPS satellite, the ECP point is calculated and the process described for a negative elevation angle is followed with the ECP replacing the IP. The resulting scale factor for this case is 2.

$$E_{ecp} = \arccos\left(\frac{R_n + h_a}{R_n + h}\right) \tag{B.9}$$

APPENDIX C

NOMENCLATURE

DOF	Degree of Freedom
ECEF	Earth Centered Earth Fixed
ECI	Earth Centered Inertial
ECP	Effect Calculation Point
EKF	Extended Kalman Filter
GDOP	Geometric Delusion of Precision
GPS	Global Positioning System
IP	Intermediate Point
ISS	International Space Station
J2000	Julian 2000 Epoch
LOS	Line of Sight
LVLH	Local Vertical Local Horizontal
PDOP	Position Delusion of Precision
PV	Position-Velocity
RGPS	Relative Global Positioning System
RMS	Root Mean Square
RSS	Root Sum Square
STK	Satellite Tool Kit
TEC	Total Electron Count

VITA

Name: Matthew Peyton Fritz

Address: Texas A&M University
Department of Aerospace Engineering
H.R. Bright Building, Rm. 701, Ross Street - TAMU 3141
College Station TX 77843-3141

Email Address: aeroag85@gmail.com

Education: B.S. Aerospace Engineering
Texas A&M University, 2007
M.S. Aerospace Engineering
Texas A&M University, 2009